BLANK PAGES
XI-4-161
XI-4-162
XI-4-163
XI-4-164
XI-4-165
XI-4-166
XI-4-167
XI-4-168

BLANK PAGE

4.9.5 Radial Expansion Inner Shell - Uranium

The expansion of the inner shell adjacent to the uranium ring in the end of the cask was determined in the ANSYS analysis of Section 3.8 to be .084 inches outward. The radial growth of the uranium ring may be determined by considering the growth due to temperature effects. The temperature of the uranium ring is calculated in Appendix D, Section VIII.

$$\text{Average uranium temp.} = \frac{401 + 377}{2} \quad \text{(average of nodes 22 and 23)}$$

$$= 389^{\circ}F$$

$$\alpha = 9.35 \times 10^{-6} \text{ in/in./}^{\circ}F \text{ (Sect. 1.2)}$$

$R_i = 23.375$ in. (initial clearance of .125 in.)

$$\Delta R = 23.375(9.35 \times 10^{-6})(389 - 68)$$

$$= .07$$

No interference will occur since

$$.084 < .07 + .125$$

4.9.6 SHELL STRESSES FOR THE POST-FIRE CONDITION

INTRODUCTION

Utilizing the finite element model described in Section 3.8, the shell stresses were computed for the post-fire, steady-state temperature distributions. Additionally, the evaluation methods used for the normal cycle, with the appropriate changes in allowable stress values, were used to assess the adequacy of the cask. Structural stability of the shells was also investigated as was the possible degrading influence of creep on shell stability.

SUMMARY AND CONCLUSIONS

The post-fire analysis indicated:

a. Large shell stresses are developed due, in part, to high calculated lead pressure. However, these shell stresses are largely secondary in nature and thus do not present limitations on the cask design as evidenced by the adequacy of the margins computed in the evaluation to the design criteria of Section 1.2.

b. The post-fire buckling analysis of the cask shell system indicates that there are no shell instabilities for the most demanding case of internal heat load and ambient temperature.

c. In the presence of representative initial imperfections and under the most severe temperature and lead pressure conditions, circumferential lead creep is seen to stabilize quickly and diminish. The creep does not relax the restraining influence of the lead.

ANALYSIS FOR STRESS EVALUATION

Model Description and Loading

The ANSYS finite element model described in Section 3.8 served to simulate the cask in the post-fire conditions. For the stress evaluation phase of the analysis, the post-fire, steady-state temperatures for the 70 kw heat load, 130° F ambient were obtained from the thermal solution presented in Section VIII, Appendix D. A more severe temperature distribution for this same case is presented in Section VIII, Appendix E. Because the margins by which the stresses in the evaluation meet the allowables are large, it was not considered necessary to use the latest temperature distribution for the 70 kw, 130° F ambient case. However, in the buckling considerations, the more severe Section VIII, Appendix E temperatures were used.

In addition to the 70 kw, 130° F ambient post-fire solution, the 70 kw, -40° F ambient post-fire condition was included in the evaluation. The temperatures for this case were taken from Section VIII, Appendix E. For convenience, the cask temperatures for the two post-fire cases used in the evaluation are sketched in Figs. 4.9.6-1 and 2.

The general ANSYS solution techniques described in Section 3.8 were used for the post-fire evaluation solutions. In these solutions, the stainless steel was considered elastic.

RESULTS FROM ELASTIC STAINLESS STEEL CASK SOLUTIONS

Figures 4.9.6-3 through 11 present the lead pressure and shell stresses resulting from the 70 kw, 130° F ambient post-fire temperature distribution. These figures indicate lead pressure of approximately 1100 psi and a general stress level in the inner shell of approximately 30.0 ksi. Detailed stress

component values for the post-fire solutions for each of the thirty-four evaluation locations of the cask shown in Figs. 3.8.4-15 and 16 are presented in the tabulation of base case stresses, Table 3.8.4-2. The 70 kw, 130°F and -40°F ambient post-fire results are listed in Table 3.8.4-2 as base case numbers 6 and 14, respectively.

EVALUATION

The only loading case examined for primary stresses in the post-fire evaluation was for the full pin-burst cavity pressure of 85.8 psi. Table 4.9.6-1 presents the results of this evaluation. To develop this table, the primary stresses of Table 3.8.4-1 for the 100 psi cavity pressure solution were multiplied by 0.858 to obtain primary component stresses for an 85.8 psi cavity pressure load. The effective stresses were then computed at each section evaluated. The 0.7 S_u allowable is appropriate for this comparison.

Using the base case stresses reported in Table 3.8.4-2, the primary plus secondary stresses were computed. Examining the primary plus secondary stresses at each cask location for the post-fire temperature distribution, Table 4.9.6-2, three points in the cask are found to exceed the 0.9 S_u allowable stress: the outside of the inner shell at the top of the cask and both sides of the outer shell at the bottom of the cask. Since these stresses exceed the allowable, it was necessary, in accordance with the design criteria, to examine the peak stress range of these locations for the normal stress cycle augmented by the drop loadings and the post-fire conditions. Table 4.9.6-3 presents the thirty-four base case combinations making up the loading conditions considered in this phase of the evaluation.

The primary-plus-secondary stress range for each cask location was com-

THIS PAGE INTENTIONALLY LEFT BLANK

puted using the method described in Section 3.8.5. In these calculations all 34 loading cases were used as reference cases to insure that the maximum stress range was determined including fabrication , normal and accident conditions. The maximum stress range occurred with load case 22 as reference. The stress range was computed for all 34 cask locations indicated in Figures 3.8.4 - 15 & 16. Table 4.9.6-4 presents the listing showing the maximum computed range of 123.6 ksi, which occurred at the outside of the outer shell at the bottom of the cask. Based on a conservative stress concentration factor of 4.0, a peak stress range of 494 ksi was computed. This range is below the allowable stress (S_{a10} = 650 ksi) for alternate 2 of the accident stress criteria (Sect. 1.1 p. XI-1-7d).

SHELL STABILITY IN POST-FIRE CONDITIONS

To accurately assess the states of stress in the cask shells and the lead pressures developed in the post-fire cases, additional ANSYS solutions were performed that considered the stainless steel shells to be elastic-plastic. The stress-strain curves used for these solutions were the same as those presented in Section 3.8. The curves and the bilinearization required for the ANSYS solutions are shown in Fig. 4.9.6-12. In the bilinearization for the post-fire solutions, a total strain of 0.2% was selected as the strain point to determine the elastic-plastic tangent slope. This strain level is approximately the maximum expected strain in the post-fire solutions. As with the stress-strain curves used in the normal case, the 600° F curve was bilinearized and the same elastic-plastic slope was used for curves of lower temperatures. In the buckling calculation, the 600° F empirical relationship (adjusted for minimum yield stress) from Ref. 71 is used.

The stress-strain curves employed to represent the lead in these solutions are given in Fig. 4.9.6-13. These curves are a combination of the experimen-

tal data from Ref. 20 and the high temperature lead data from the NL Research Laboratory, Ref. 81. The ANSYS bilinearization of the lead is also shown in Fig. 4.9.6-13. In the buckling solutions, the lead secant and tangent moduli for the particular conditions were specified as parameters to the solution and were further assumed to be constant as the shell loading parameters were varied.

The thermal solutions used in the buckling stress calculations were all taken from Section VIII, Appendix E. The temperatures of these solutions at the critical cask mid-plane are in general slightly higher, and the gradients slightly larger, than the solutions of Section VIII, Appendix D. With the higher temperatures and gradients, the stress-strain properties are degraded their maximum amount and with the higher gradients, the lead pressure levels are higher. Therefore, the Section VIII, Appendix E temperatures represent the more severe loadings.

Buckling of the Lower Unsupported Portion of the Inner Shell

The lower part of the inner shell backed by the cylindrical uranium sleeve does not have the support of the lead cushion to aid in shell stability. Therefore, the buckling stability of this part of the inner shell was examined separately from the remainder of the shell. A sketch of the geometry of this part of the cask is given in Fig. 4.9.6-14.

The maximum compressive stresses on the lower section of the shell are computed for the 70 kw, 130° F ambient post-fire solution. In the solution, this region was shown to have membrane hoop stresses of -8481 psi and membrane axial stresses of -5909 psi. The shell temperature for this condition was 420° F.

To determine the stability of the shell under these loadings, the buckling

development of Appendix C was used in its single shell mode. In this solution, the unsupported inner shell was examined for axial and circumferential buckling. The axial half wave lengths were varied consistent with the possible integer number of half waves between the uranium support ring and the bottom head. The number of circumferential waves starting with the axisymmetric solution was increased until the minimum buckling load was determined.

The axial and hoop loads were applied simultaneously in approximately the same ratios as the maximum computed stresses noted above.

The minimum buckling hoop and axial stresses were found to be -28600psi and -20300psi, respectively. This buckling load is well in excess of the maximum computed load for this part of the inner shell, thus assuring its stability.

Determination of the Most Critical Loading for Buckling of the Inner Shell

To assess which of the post-fire conditions was the most severe, the lead pressures for several heat loads and ambient temperatures were determined by using a small finite element model. This model was the same ANSYS model which was used to determine the lead pressures in the normal conditions in Section 3.8.3 and is described further in that section. The loading consisted of the cask mid-plane temperatures and a cavity pressure of 16.5 psi.

The results of this lead pressure evaluation are shown in Fig. 4.9.6-15. The maximum lead pressure of 701 psi was developed for the 70 kw, 130° F ambient case. Since the highest shell and lead temperatures are experienced in this same loading condition, the 70 kw, 130° F ambient case is clearly the most critical for the buckling stability evaluation.

To determine more accurately the lead pressure for the 70 kw, 130° F ambient case, the full-cask ANSYS model described in Section 3.8.3 with

elastic-plastic stainless steel shells was used. This model does not have the axial constraint of the small model used in the lead pressure study. Thus, the computed lead pressure of 640 psi is lower than that computed with the small model.

Shell Stability for the Post-Fire Condition

The buckling solution developed in Appendix C for the 10/24 cask shell-lead-shell system was used to assess the inner shell's stability under the most severe post-fire conditions. In the buckling solution, the half wave length was taken to be the full inner shell length of 160 in. The number of circumferential waves was varied until the minimum buckling load was determined. The lead moduli in the buckling solution were computed by the deformation theory development of Appendix C. The parameters of the solution for the 70 kw, 130° F ambient post-fire buckling case are listed below.

	Inner Shell	Lead	Outer Shell
Hoop Stress	-P*22.9/0.75	-P-36(1)	P*30.25/2.0
Axial Stress	-16000(2)	-P-36	-8000(2)
Radial Stress	-P/2.0	-P	-P/2.0
Temperature	591° F	586° F	530° F
Tangent Slope	empirical curve(3)	350(4)	empirical curve
Secant Slope	empirical curve	4380(4)	empirical curve

NOTES:

1. The lead pressure was considered the loading parameter. The 36.0 psi difference between the component stresses is as computed in the ANSYS solution for the 70 kw, 130° F ambient post-fire case.
2. ANSYS results for the 70 kw, 130° F ambient post-fire case.

3. An equivalent stress was computed from the component stresses. This equivalent stress was then used in conjunction with the empirical stress-strain curve for the appropriate temperature to determine the secant and tangent moduli.
4. Estimates based on the lead data of Fig. 4.9.6-13 for a computed total lead strain of 0.0075 in./in.

This buckling solution predicted a minimum buckling pressure of 860 psi. This minimum pressure occurred with nine circumferential waves.

The minimum buckling pressure is significantly larger than the maximum computed lead pressure. Further, as evidenced by Fig. 4.9.6-15, it does not appear that the lead pressure could reach the predicted buckling pressure. The buckling solution itself is conservative for at least the following two reasons: 1) the axial temperature gradient is not considered; this would effectively shorten the shell axially; 2) the minimum lead properties are assumed for the whole lead layer; including the radial gradient would provide additional lead support for the inner shell.

Circumferential Creep Buckling Solution

To help determine if the margin between the minimum buckling pressure and the computed lead pressure for the post-fire condition and the normal condition is adequate, additional buckling solutions were completed. These solutions included initial waves in the inner shell and allowed for the possibility of circumferential creep.

The geometry of the ANSYS model used for the circumferential creep calculation is shown in Fig. 4.9.6-16. The model represents a cross-sectional

cut at cask mid-plane and is made up of isoparametric ring elements, ANSYS STIF 42, for the stainless steel and constant strain elements, ANSYS STIF 2, for the lead. The model is assembled to form a large diameter torus. This type of idealization simulates the generalized plane-strain nature of the stress-strain distribution at the cask mid-section and allows for the circumferential redistribution of the lead.

Two different cases were completed with this model. The first had four circumferential waves imposed on the inner shell, and the second had eight waves so imposed. (To obtain the eight-wave solution, the model shown in Fig. 4.9.6-16 was condensed from an 180° segment to a 90° segment. The same number of elements was used in both models.) The amplitude of the circumferential wave on the inner shell for both solutions was 0.02 in. This amplitude is on the same order as the fabrication tolerances for the inside diameter of the inner shell.

The creep expression developed for lead in Appendix B was used. In addition, the large displacement option of ANSYS was active for every loading and time step. With this option, the geometry is updated after each solution step.

In the solutions, the 70 kw, 130°F ambient post-fire temperature conditions were initially imposed. After this initial loading was established, the calculations were stepped in time.

In both solutions, there was no amplification of the initial circumferential waves initially, or as the solution progressed. Further, the effective stress in the lead decreased at all points in the model with time but with no accompanying decrease in the indicated lead pressure.

Thus, the solutions indicate that the inner shell is stable in the presence of representative initial imperfections and possible circumferential creep.

This result, together with the indicated margin of the Appendix C buckling calculation, demonstrates the inner shell stability for the post-fire loading.

TABLE 4.9.6-1 REV. 1-2/76

ACCIDENT PRIMARY STATIC AND DYNAMIC STRESS EVALUATION

BASE CASE	MULTIPLIER	BASE CASE DESCRIPTION
10	.85800	100 PSI CAVITY

LOCATION	EFFECTIVE STRESS	TEMP.	STRESS ALLOWABLES 0.9SY	0.7SU	0.9SU
1	749	437	18204	41806	53750
3	240	395	18699	42131	54169
5	68	257	21230	45754	58826
7	768	474	17800	41611	53500
9	450	447	18095	41753	53683
11	867	559	16872	41165	52927
13	484	502	17494	41464	53311
15	75	327	19946	43916	56464
17	1300	460	17953	41685	53595
19	1323	458	17975	41695	53608
21	1070	456	17996	41706	53622
23	410	415	18444	41921	53899
25	153	388	18828	42315	54405
27	108	257	21230	45754	58826
29	948	386	18864	42367	54472
31	841	386	18864	42367	54472
33	864	344	19634	43470	55890

TABLE 4.9.6-2

REV. 1-2/76

ACCIDENT PRIMARY PLUS SECONDARY STATIC AND DYNAMIC STRESS EVAL.

BASE CASE	MULTIPLIER	BASE CASE DESCRIPTION
6	1.00000	POST FIRE 70KW 130F AMBIENT
10	.85800	100 PSI CAVITY

LOCATION	EFFECTIVE STRESS	TEMP.	0.9SY	STRESS ALLOWABLES 0.7SU	0.9SU
1	39387	439	18182	41795	53737
2	73680 ←	435	18225	41815	53764
3	23335	408	18520	41958	53946
4	21744	381	18955	42499	54641
5	20497	257	21230	45754	58825
6	20757	257	21230	45754	58825
7	29907	475	17778	41601	53487
8	28849	471	17833	41627	53521
9	19492	459	17964	41690	53602
10	18707	435	18226	41815	53764
11	37104	561	16851	41155	52913
12	33167	556	16905	41181	52947
13	20064	514	17363	41401	53230
14	22110	490	17625	41527	53392
15	26971	327	19946	43916	56
16	27065	327	19946	43916	56
17	18211	462	17931	41574	53581
18	34644	458	17975	41695	53608
19	29374	458	17975	41695	53608
20	16845	458	17975	41695	53608
21	36233	456	17995	41706	53622
22	32585	455	18007	41711	53629
23	16025	427	18313	41858	53818
24	9997	402	18585	41989	53985
25	75254 ←	402	18585	41989	53985
26	52001 ←	374	19084	42582	54877
27	43848	257	21230	45754	58825
28	6853	257	21230	45754	58825
29	4350	385	18864	42357	54472
30	16993	385	18864	42357	54472
31	36573	386	18864	42367	54472
32	16324	386	18864	42367	54472
33	28681	344	19634	43478	55390
34	49502	344	19634	43479	55390

TABLE 4.9.6-2 (CONT.) REV. 1-2/76

ACCIDENT PRIMARY PLUS SECONDARY STATIC AND DYNAMIC STRESS EVAL

BASE CASE	MULTIPLIER	BASE CASE DESCRIPTION
10	.85800	100 PSI CAVITY
14	1.00000	POST FIRE 70KW -40F AMBIENT

LOCATION	EFFECTIVE STRESS	TEMP.	0.9SY	STRESS ALLOWABLES 0.7SU	0.9SU
1	48575	240	21541	45200	59400
2	58515 ←	239	21553	45226	59434
3	27718	218	21945	45777	60142
4	33407	207	22147	47056	60514
5	30369	55	28214	57830	74352
6	12184	55	28214	57830	74352
7	23101	301	20423	44599	57341
8	17127	299	20460	44651	57409
9	15297	298	20478	44677	57442
10	10988	285	20715	45019	57881
11	30470	445	18116	41764	53595
12	27303	442	18149	41779	53716
13	15465	389	18859	42289	54371
14	16922	376	19048	42530	54610
15	32603	158	23802	49512	63658
16	32759	158	23802	49512	63658
17	7111	283	20753	45071	57949
18	37348	281	20790	45124	58016
19	19565	252	21321	45885	58995
20	16760	252	21321	45885	58995
21	6484	271	20973	45386	58354
22	5164	269	21010	45439	58421
23	24242	251	21340	45911	59029
24	8345	239	21560	45226	59434
25	84654 ←	208	22128	47040	60480
26	84653 ←	197	22384	47412	60958
27	65629	55	28214	57830	74352
28	9025	55	28214	57830	74352
29	6338	193	22311	47304	60819
30	7555	199	22311	47304	60819
31	25035	193	22638	47788	61442
32	21131	190	22638	47788	61442
33	51673	163	23620	49242	63312
34	29655	163	23620	49242	63312

TABLE 4.9.6-3

REV. 1-2/76

ACCIDENT STRESS RANGE EVAL. NORM. CYCLE 30FT DROPS AND POST F

LOAD CASES CONSIDERED IN ACCIDENT STRESS RANGE EVALUATION

LOAD CASE 1 FOR RANGE CALCULATIONS		
BASE CASE	MULTIPLIER	
1	1.000	0.0 STRESS
LOAD CASE 2 FOR RANGE CALCULATIONS		
BASE CASE	MULTIPLIER	
2	1.000	-40.0 F ISOTHERMAL
8	-.100	30 G BOTTOM END DROP
11	3.160	1.0 G SIDE DROP
LOAD CASE 3 FOR RANGE CALCULATIONS		
BASE CASE	MULTIPLIER	
2	1.000	-40.0 F ISOTHERMAL
8	-.100	30 G BOTTOM END DROP
11	-3.160	1.0 G SIDE DROP
LOAD CASE 4 FOR RANGE CALCULATIONS		
BASE CASE	MULTIPLIER	
2	1.000	-40.0 F ISOTHERMAL
8	.100	30 G BOTTOM END DROP
11	3.160	1.0 G SIDE DROP
LOAD CASE 5 FOR RANGE CALCULATIONS		
BASE CASE	MULTIPLIER	
2	1.000	-40.0 F ISOTHERMAL
8	.100	30 G BOTTOM END DROP
11	-3.160	1.0 G SIDE DROP
LOAD CASE 6 FOR RANGE CALCULATIONS		
BASE CASE	MULTIPLIER	
2	1.000	-40.0 F ISOTHERMAL
11	14.550	1.0 G SIDE DROP
LOAD CASE 7 FOR RANGE CALCULATIONS		
BASE CASE	MULTIPLIER	
2	1.000	-40.0 F ISOTHERMAL
11	-14.550	1.0 G SIDE DROP
LOAD CASE 8 FOR RANGE CALCULATIONS		
BASE CASE	MULTIPLIER	
3	1.000	70.0 F ISOTHERMAL
8	-.100	30 G BOTTOM END DROP
11	3.160	1.0 G SIDE DROP

REV. 1 - 2/76

TABLE 4.9.6 - 3 (CONT.)

ACCIDENT STRESS RANGE EVAL. NORM. CYCLE 30FT DROPS AND POST FI

LOAD CASES CONSIDERED IN ACCIDENT STRESS RANGE EVALUATION

LOAD CASE 9	FOR RANGE	CALCULATIONS
BASE CASE	MULTIPLIER	
3	1.000	70.0 F ISOTHERMAL
8	-.100	30 G BOTTOM END DROP
11	-3.160	1.0 G SIDE DROP
LOAD CASE 10	FOR RANGE	CALCULATIONS
BASE CASE	MULTIPLIER	
3	1.000	70.0 F ISOTHERMAL
8	.100	30 G BOTTOM END DROP
11	3.160	1.0 G SIDE DROP
LOAD CASE 11	FOR RANGE	CALCULATIONS
BASE CASE	MULTIPLIER	
3	1.000	70.0 F ISOTHERMAL
8	.100	30 G BOTTOM END DROP
11	-3.160	1.0 G SIDE DROP
LOAD CASE 12	FOR RANGE	CALCULATIONS
BASE CASE	MULTIPLIER	
3	1.000	70.0 F ISOTHERMAL
11	14.550	1.0 G SIDE DROP
LOAD CASE 13	FOR RANGE	CALCULATIONS
BASE CASE	MULTIPLIER	
3	1.000	70.0 F ISOTHERMAL
11	-14.550	1.0 G SIDE DROP
LOAD CASE 14	FOR RANGE	CALCULATIONS
BASE CASE	MULTIPLIER	
4	1.000	NORMAL 70KW 130F AMBIENT
8	-.100	30 G BOTTOM END DROP
11	3.160	1.0 G SIDE DROP
LOAD CASE 15	FOR RANGE	CALCULATIONS
BASE CASE	MULTIPLIER	
4	1.000	NORMAL 70KW 130F AMBIENT
8	-.100	30 G BOTTOM END DROP
11	-3.160	1.0 G SIDE DROP
LOAD CASE 16	FOR RANGE	CALCULATIONS
BASE CASE	MULTIPLIER	
4	1.000	NORMAL 70KW 130F AMBIENT
8	.100	30 G BOTTOM END DROP
11	3.160	1.0 G SIDE DROP

REV. 1-2/76

TABLE 4.9.6-3 (CONT.)

ACCIDENT STRESS RANGE EVAL. NORM. CYCLE 30FT DROPS AND POST

LOAD CASES CONSIDERED IN ACCIDENT STRESS RANGE EVALUATION

LOAD CASE 17	FOR RANGE CALCULATIONS	
BASE CASE	MULTIPLIER	
4	1.000	NORMAL 70KW 130F AMBIENT
8	.100	30 G BOTTOM END DROP
11	-3.160	1.0 G SIDE DROP
LOAD CASE 18	FOR RANGE CALCULATIONS	
BASE CASE	MULTIPLIER	
4	1.000	NORMAL 70KW 130F AMBIENT
11	14.550	1.0 G SIDE DROP
LOAD CASE 19	FOR RANGE CALCULATIONS	
BASE CASE	MULTIPLIER	
4	1.000	NORMAL 70KW 130F AMBIENT
11	-14.550	1.0 G SIDE DROP
LOAD CASE 20	FOR RANGE CALCULATIONS	
BASE CASE	MULTIPLIER	
5	1.000	10 MIN. IN POOL COOL-DOWN
LOAD CASE 21	FOR RANGE CALCULATIONS	
BASE CASE	MULTIPLIER	
6	1.000	POST FIRE 70KW 130F AMBIENT
10	.858	100 PSI CAVITY
LOAD CASE 22	FOR RANGE CALCULATIONS	
BASE CASE	MULTIPLIER	
10	.858	100 PSI CAVITY
14	1.000	POST FIRE 70KW -40F AMBIENT
LOAD CASE 23	FOR RANGE CALCULATIONS	
BASE CASE	MULTIPLIER	
4	1.000	NORMAL 70KW 130F AMBIENT
7	1.000	30 G TOP END DROP
LOAD CASE 24	FOR RANGE CALCULATIONS	
BASE CASE	MULTIPLIER	
4	1.000	NORMAL 70KW 130F AMBIENT
8	1.000	30 G BOTTOM END DROP
LOAD CASE 25	FOR RANGE CALCULATIONS	
BASE CASE	MULTIPLIER	
4	1.000	NORMAL 70KW 130F AMBIENT
11	81.000	1.0 G SIDE DROP
LOAD CASE 26	FOR RANGE CALCULATIONS	
BASE CASE	MULTIPLIER	
4	1.000	NORMAL 70KW 130F AMBIENT
11	-81.000	1.0 G SIDE DROP

REV. 1-2/76

TABLE 4.9.6-3 (CONT.)

ACCIDENT STRESS RANGE EVAL. NORM. CYCLE 30FT DROPS AND POST FI

LOAD CASES CONSIDERED IN ACCIDENT STRESS RANGE EVALUATION

LOAD CASE 27	FOR RANGE CALCULATIONS	
BASE CASE	MULTIPLIER	
7	1.000	30 G TOP END DROP
12	1.000	NORMAL 40KW -40F AMBIENT
LOAD CASE 28	FOR RANGE CALCULATIONS	
BASE CASE	MULTIPLIER	
8	1.000	30 G BOTTOM END DROP
12	1.000	NORMAL 40KW -40F AMBIENT
LOAD CASE 29	FOR RANGE CALCULATIONS	
BASE CASE	MULTIPLIER	
11	81.000	1.0 G SIDE DROP
12	1.000	NORMAL 40KW -40F AMBIENT
LOAD CASE 30	FOR RANGE CALCULATIONS	
BASE CASE	MULTIPLIER	
11	-81.000	1.0 G SIDE DROP
12	1.000	NORMAL 40KW -40F AMBIENT
LOAD CASE 31	FOR RANGE CALCULATIONS	
BASE CASE	MULTIPLIER	
7	1.000	30 G TOP END DROP
13	1.000	NORMAL 70KW -40F AMBIENT
LOAD CASE 32	FOR RANGE CALCULATIONS	
BASE CASE	MULTIPLIER	
8	1.000	30 G BOTTOM END DROP
13	1.000	NORMAL 70KW -40F AMBIENT
LOAD CASE 33	FOR RANGE CALCULATIONS	
BASE CASE	MULTIPLIER	
11	81.000	1.0 G SIDE DROP
13	1.000	NORMAL 70KW -40F AMBIENT
LOAD CASE 34	FOR RANGE CALCULATIONS	
BASE CASE	MULTIPLIER	
11	-81.000	1.0 G SIDE DROP
13	1.000	NORMAL 70KW -40F AMBIENT

REV. 1 - 2/76

TABLE. 4.9.6-4

ACCIDENT STRESS RANGE EVAL. NORM. CYCLE SOFT DOPS AND POST FIR

STRESS RANGE DATA LOAD CASE 22 USED AS REFERENCE

LOC	MAX TEMP	MIN TEMP	STRESS RANGE	MIN TEMP	STRESS RANGE
1	439	-40	55169	70	55169
2	435	-40	75549	70	75549
3	408	-40	54811	70	54811
4	391	-40	65375	70	65376
5	257	-40	46432	70	46432
6	257	-40	56751	70	56761
7	475	-40	49723	70	41792
8	471	-40	44580	70	37491
9	453	-40	55960	70	55960
10	435	-40	49653	70	49653
11	561	-40	65659	70	59578
12	555	-40	59385	70	57314
13	514	-40	56219	70	66219
14	490	-40	64911	70	64911
15	327	-40	76995	70	76995
16	327	-40	77040	70	77040
17	462	-40	31553	70	31553
18	458	-40	58194	70	56604
19	458	-40	31880	70	28106
20	458	-40	21734	70	21734
21	455	-40	32969	70	32969
22	455	-40	32291	70	32291
23	427	-40	42461	70	42461
24	402	-40	28911	70	28911
25	402	-40	101845	70	101845
26	374	-40	123560	70	108679
27	257	-40	77050	70	77050
28	257	-40	36414	70	36414
29	385	-40	14664	70	14664
30	385	-40	21605	70	18299
31	385	-40	38378	70	38378
32	385	-40	26151	70	26151
33	344	-40	52757	70	62757
34	344	-40	51010	70	47665

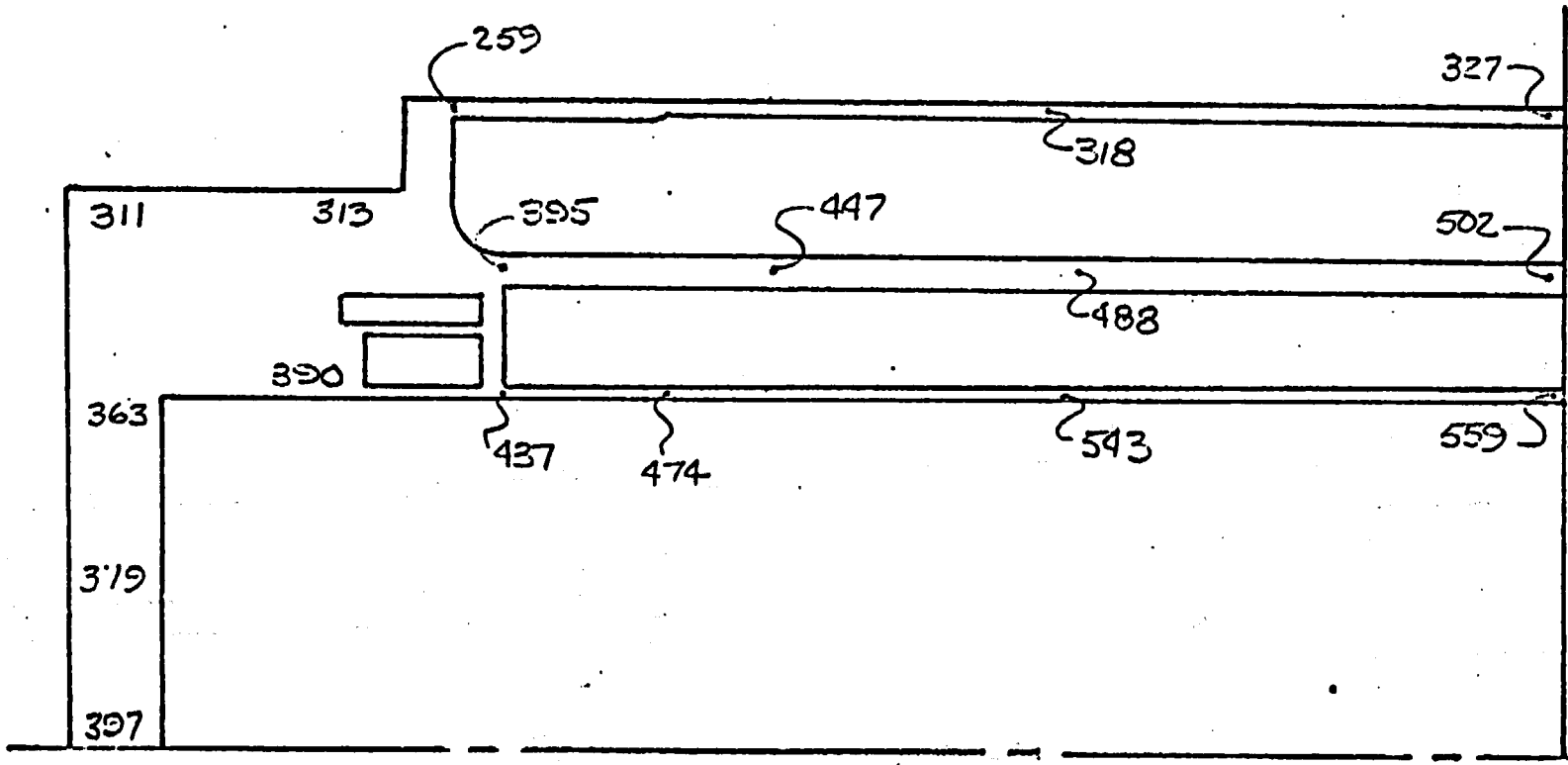

XI-4-177L

CASK, TOP

POST-FIRE CASE
70KN, 130°F (SECTION VIII APPENDIX D)
TEMPERATURE DISTRIBUTION (°F)

TR-2 1 SEPT 75 FIG. 4.9.6-1a REV. 1-2/76 JHA-74-1

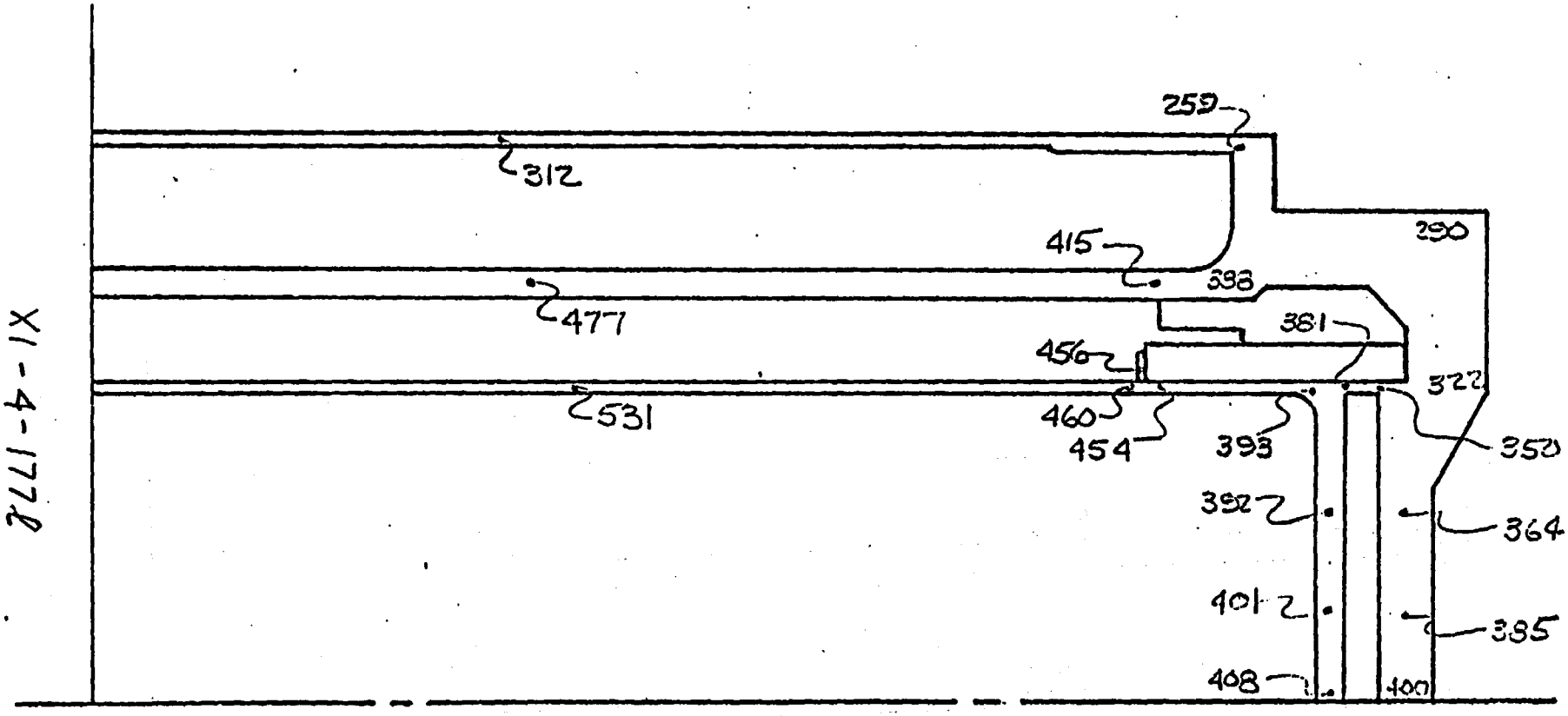

X1-4-1778

CASK, BOTTOM

POST-FIRE CASE
70 KW, 130°F (SECTION VIII APPENDIX D)
TEMPERATURE DISTRIBUTION (°F)

REV. 1-4-76 JHA-74-1

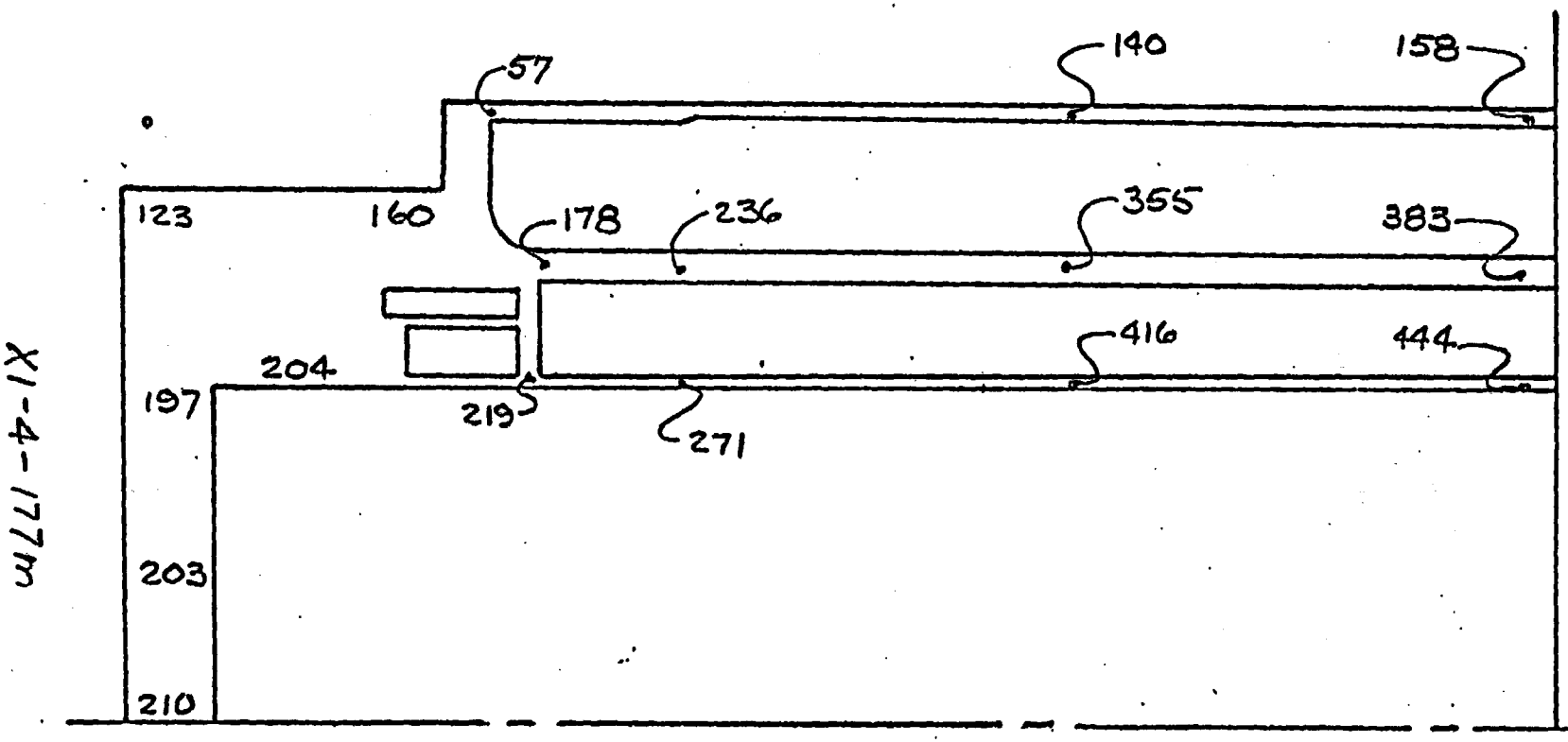

CASK, TOP

70 KW ~-40°F AMBIENT ~POST FIRE

TEMPERATURE DISTRIBUTION (°F)

LLL 25 FEB 76 | FIG. 4.9.6 - 2a

JHA-74-1 1-4-76

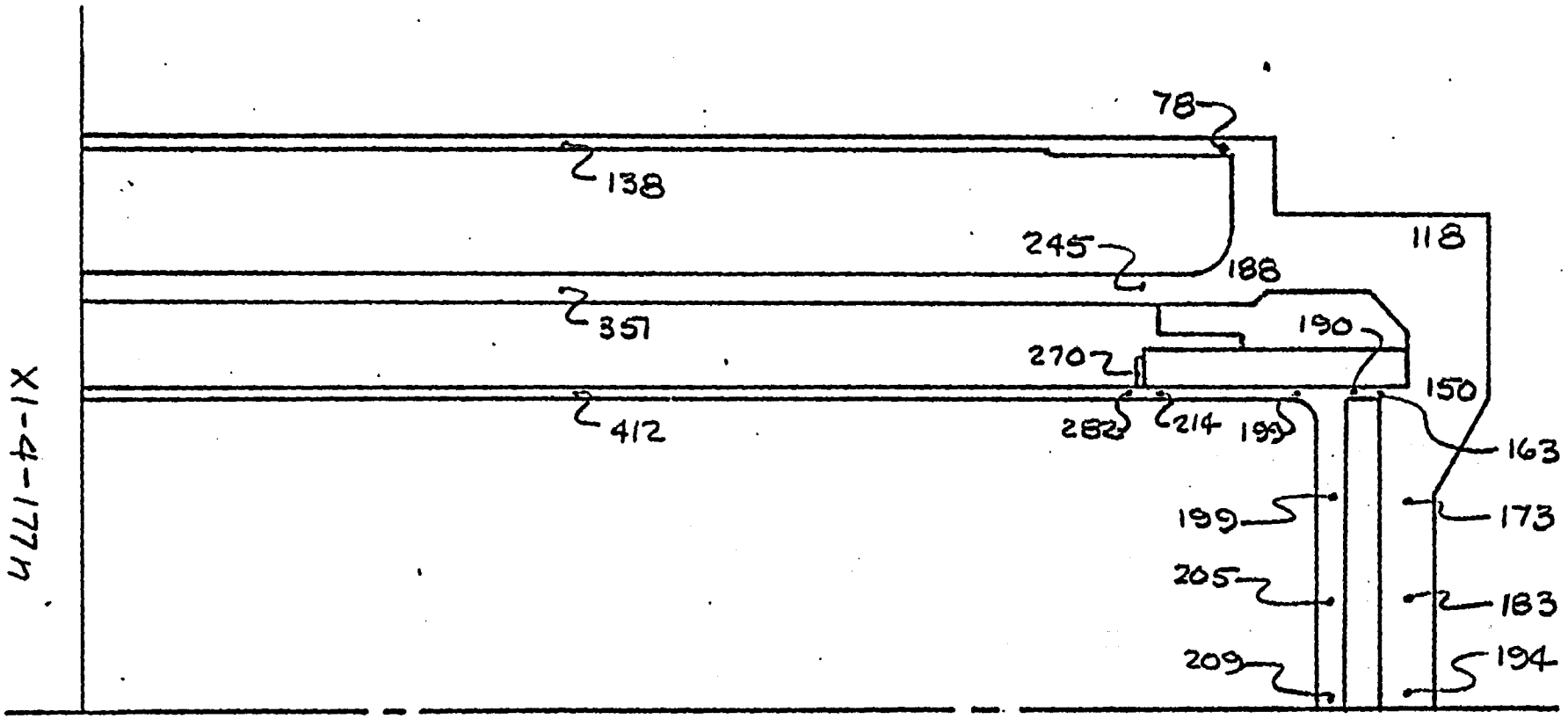

CASK, BOTTOM

70 KW ~ -40°F AMBIENT ~ POST FIRE

TEMPERATURE DISTRIBUTION (°F)

X1-4-177

REV. 1-2/76 JHA-74-1

9/11/75 I-Fig. 4.6-3

JHA-74-1
Fig. 4.7.7-4
Stresses Inside, Inner Shell
Post Fire Case
To 1hr, 1300°F Ambient
End of Lead at
Top of Cask
Axial Distance From Bottom of Cask (in)
150
152
154
156
158
160
162
164
Axial Stress ~ KSI
Hoop Stress ~ KSI
20
15
10
5
0
-5
-10
-15
-20
-25
-30
-35
-40
X1-4-177

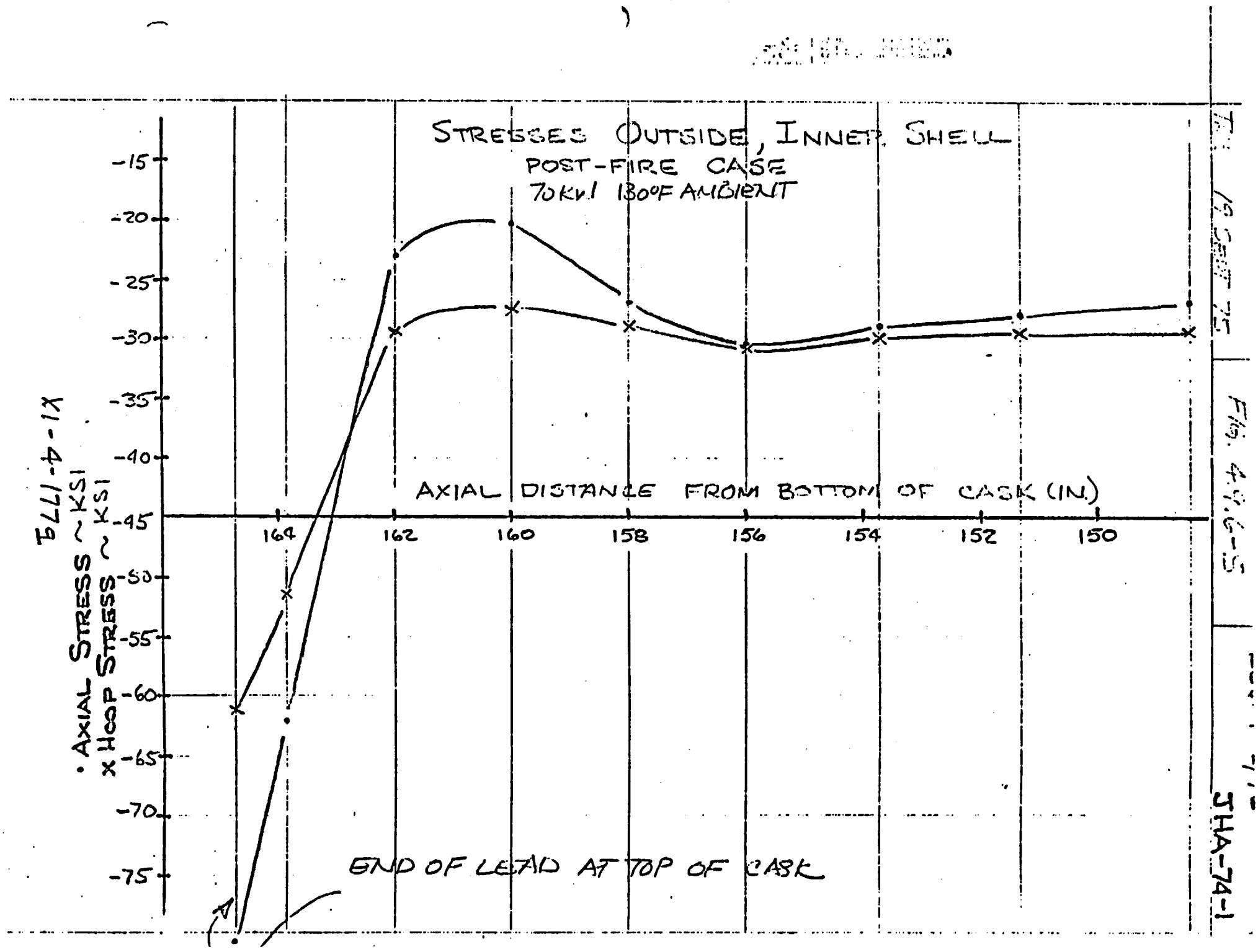
STRESSES OUTSIDE, INNER SHELL
POST-FIRE CASE
70KN 130°F AMBIENT
AXIAL DISTANCE FROM BOTTOM OF CASK (IN.)
• AXIAL STRESS ~ KSI
× HOOP STRESS ~ KSI
-15
-20
-25
-30
-35
-40
-45
-50
-55
-60
-65
-70
-75
164
162
160
158
156
154
152
150
END OF LEAD AT TOP OF CASK
A
TLLI-4-1X
THA-74-1

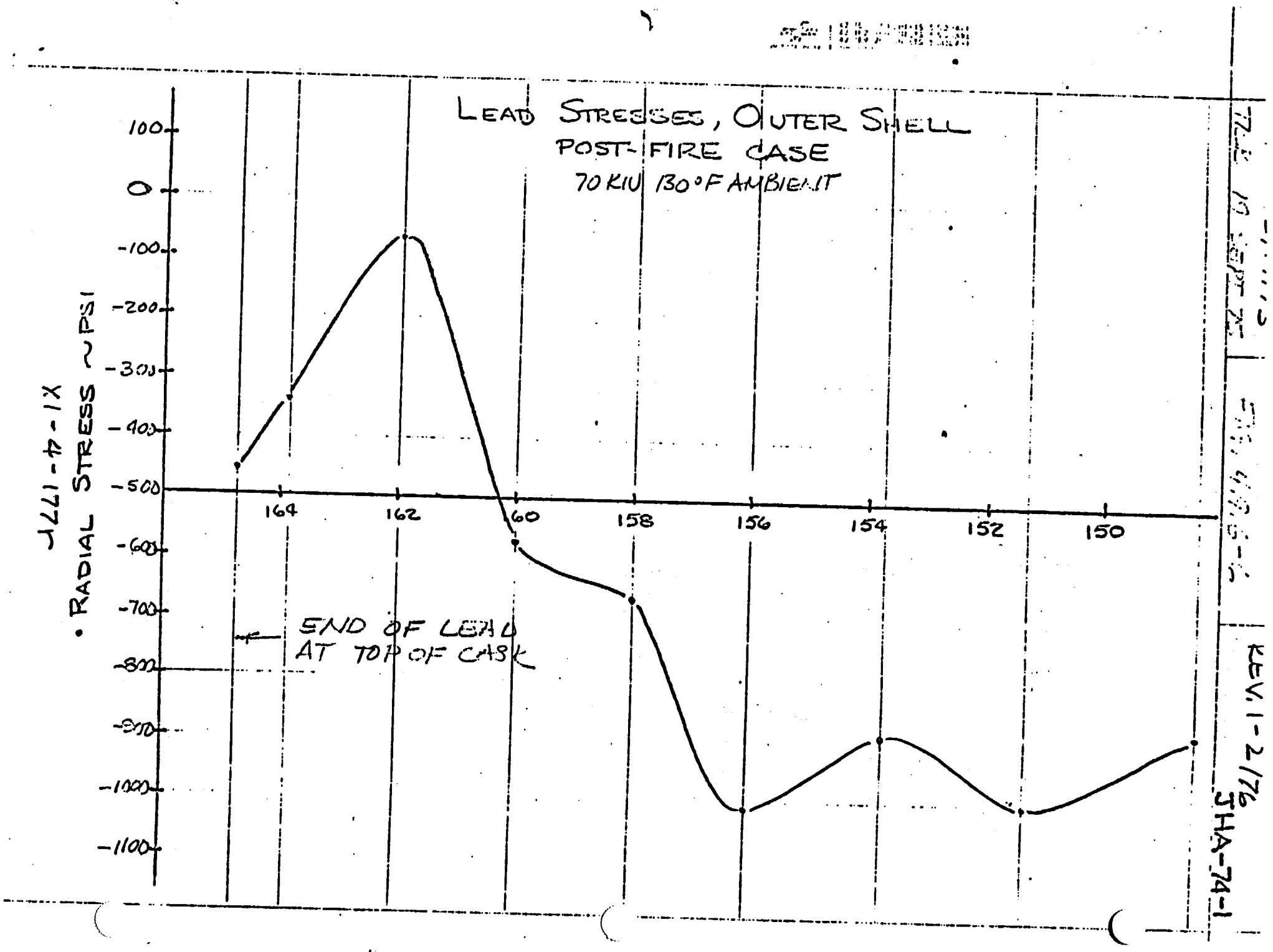
LEAD STRESSES, OUTER SHELL
POST-FIRE CASE
70 KIU 130°F AMBIENT
• RADIAL STRESS ~ PSI
JLLI-4-1X
100
0
-100
-200
-300
-400
-500
-600
-700
-800
-900
-1000
-1100
164
162
160
158
156
154
152
150
END OF LEAD
AT TOP OF CASK
REV. 1-2/76
JHA-74-1

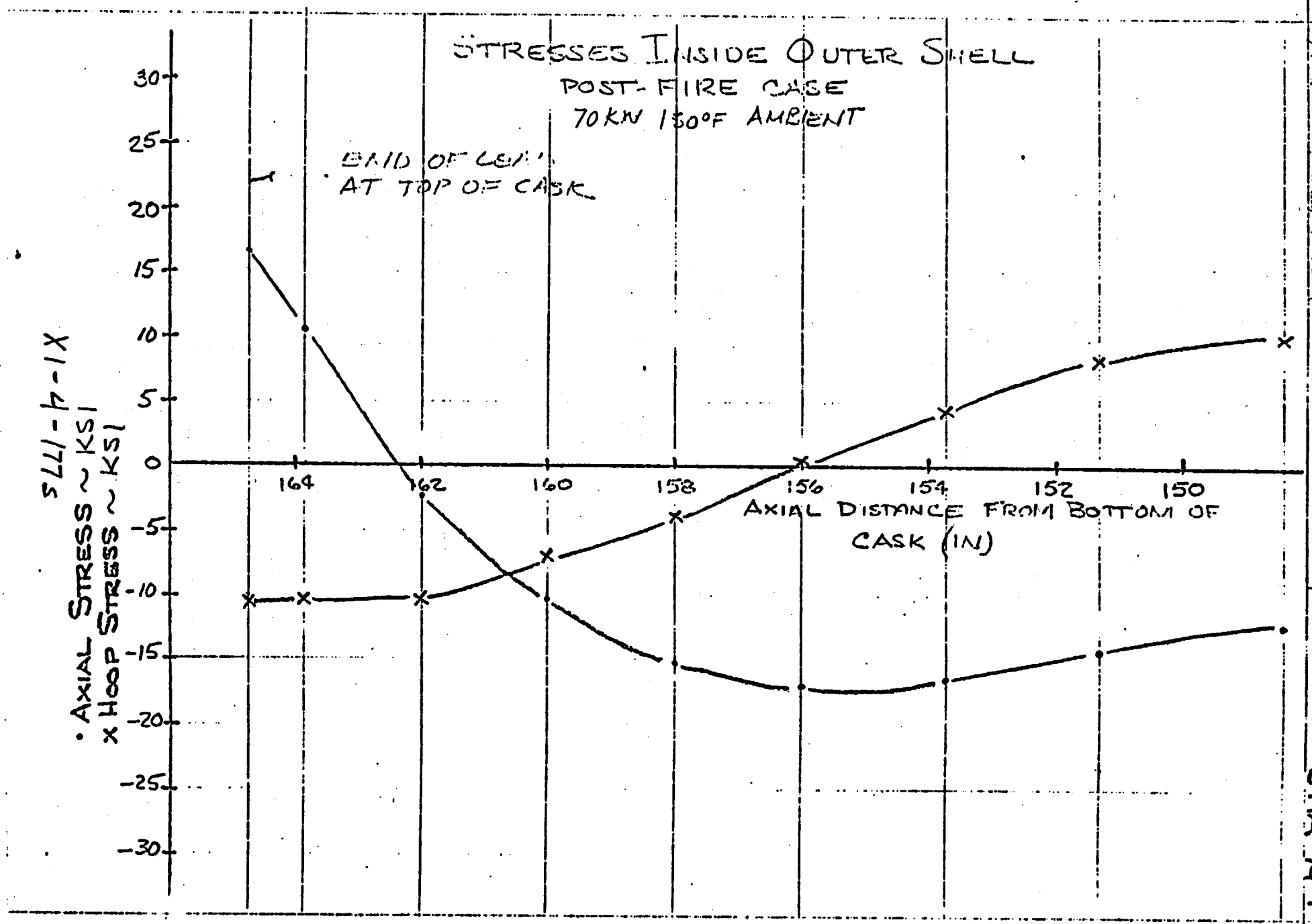

SLI-4-1X

REV. 1-2/76 JHA-74-1

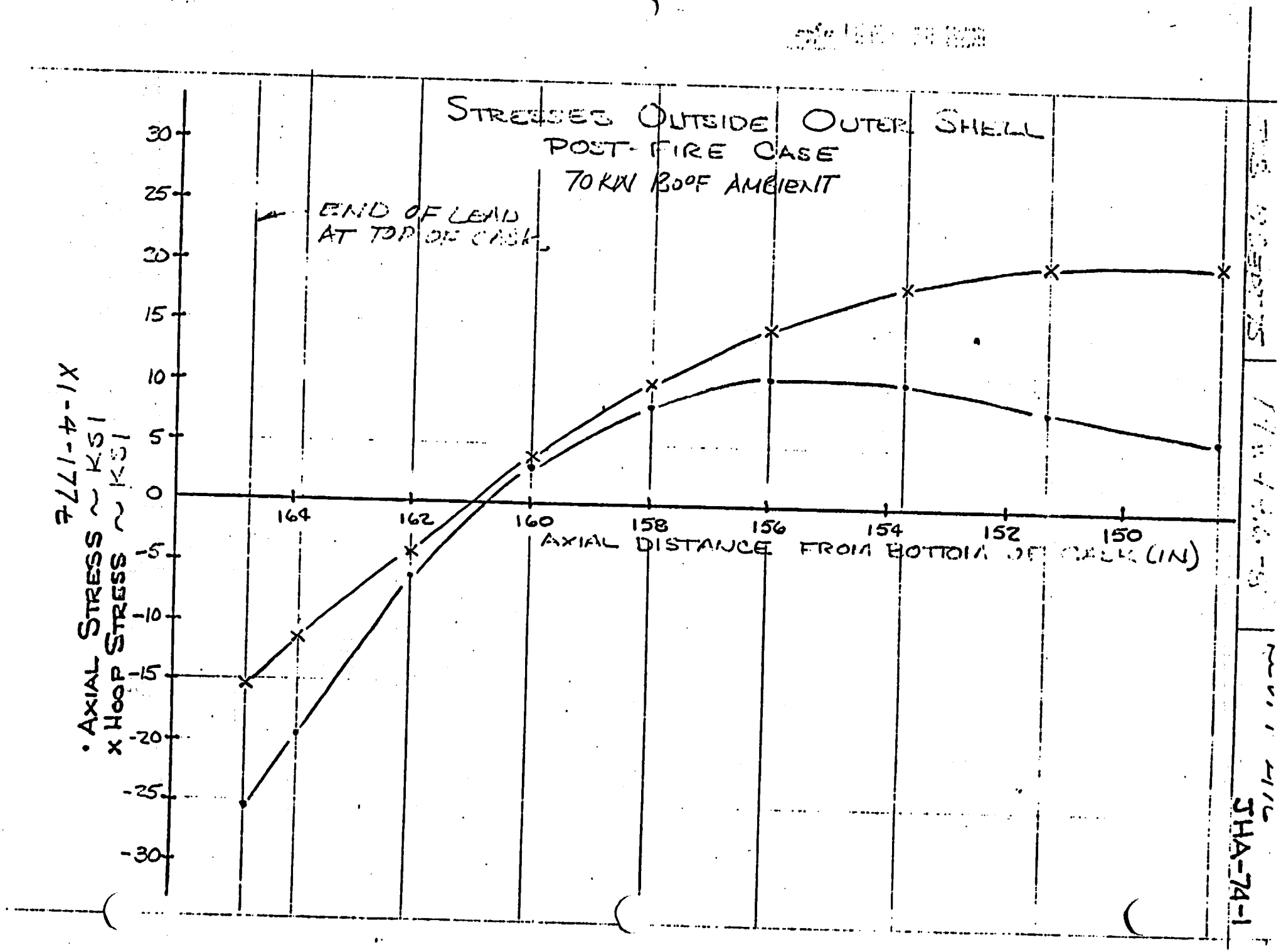
STRESSES OUTSIDE OUTER SHELL
POST-FIRE CASE
70 KN 130°F AMBIENT
END OF LEAD AT TOP OF CASE
• AXIAL STRESS ~ KSI
× HOOP STRESS ~ KSI
7711-4-1X
AXIAL DISTANCE FROM BOTTOM OF CASE (IN)
30
25
20
15
10
5
0
-5
-10
-15
-20
-25
-30
164
162
160
158
156
154
152
150

REV. 1-2/76
JHA-74-1

FIG. 4.9.6-1

LEAD STRESSES OUTER SHELL
POST-FIRE CASE
70 KW 130°F AMBIENT

END OF LEAD AT BOTTOM OF CASK

AXIAL DISTANCE FROM BOTTOM OF CASK (IN.)

0 3 6 9 12 15 18 21 24 27

1250 1000 750 500 250 0 -250 -500 -750 -1000

• RADIAL STRESS ~ PSI

X1-4-177A

REV. 1-2/76
JHA-74-1
Fig. 4.9.4-10
Stresses Inside Outer Shell
Post-Fire Case
70kN/130°F Ambient
• Axial Stress ~ KSI
× Hoop Stress ~ KSI
X1-4-1771
6
9
12
15
18
21
24
27
-50
-40
-30
-20
-10
0
10
20
30
40
50
60
70

JHA-74-1
Fig. 4.4.5.6-11
Stresses Outside Outer Shell
Post-Fire Case
70kW Boone Ambient
• Axial Stress ~ KSI
x Hoop Stress ~ KSI
-70
-60
-50
-40
-30
-20
-10
0
10
20
30
40
50
27
24
21
18
15
12
9
6
Axial Distance From Bottom of Cask (IN.)
End of Outer Shell at Bottom of Cask
X1-4-1774

FIG. 4.9.6-12 | JHA-74-1(c)

REV. 1-2/76

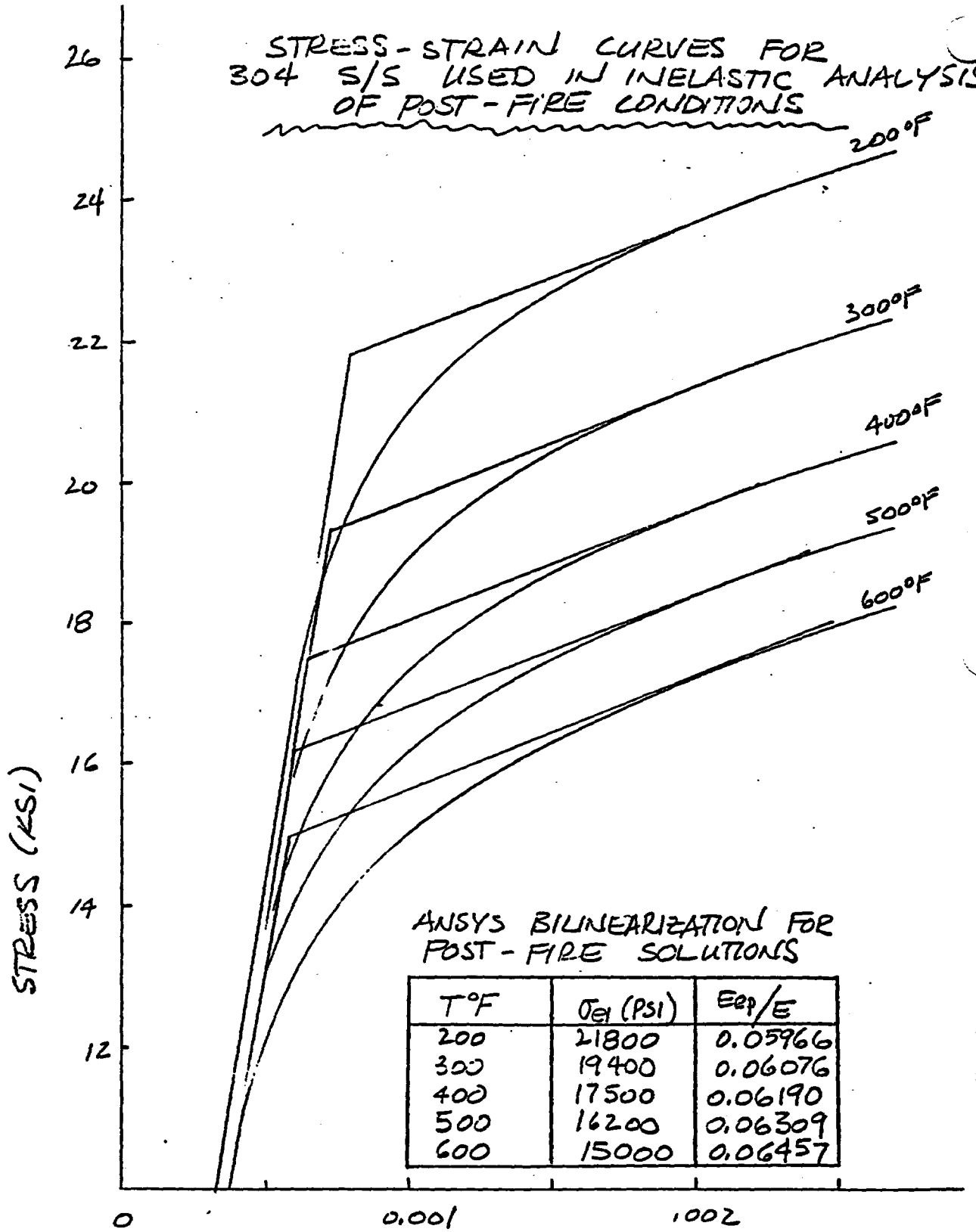

ANSYS BILINEARIZATION FOR POST-FIRE SOLUTIONS

T°F	σ_{el} (PSI)	ε_{ep}/E
200	21800	0.05966
300	19400	0.06076
400	17500	0.06190
500	16200	0.06309
600	15000	0.06457

X.1-4-177x

STRESS STRAIN CURVES USED FOR THE LEAD IN POST-FIRE BUCKLING SOLUTIONS

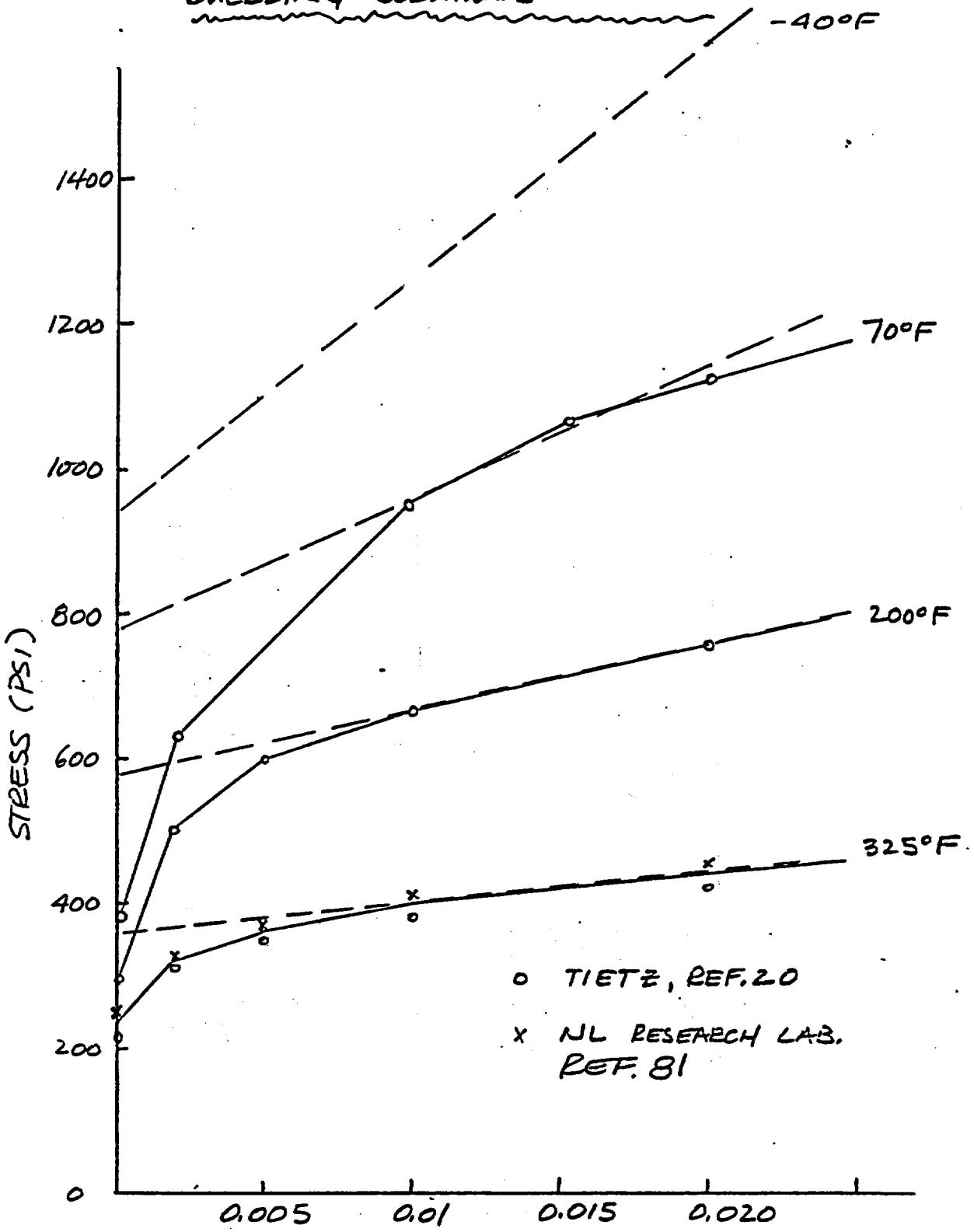

X1-4-177y

REV. 1-2/76

FIG. 4.9.6-13(6) JHA-74-1 (c)

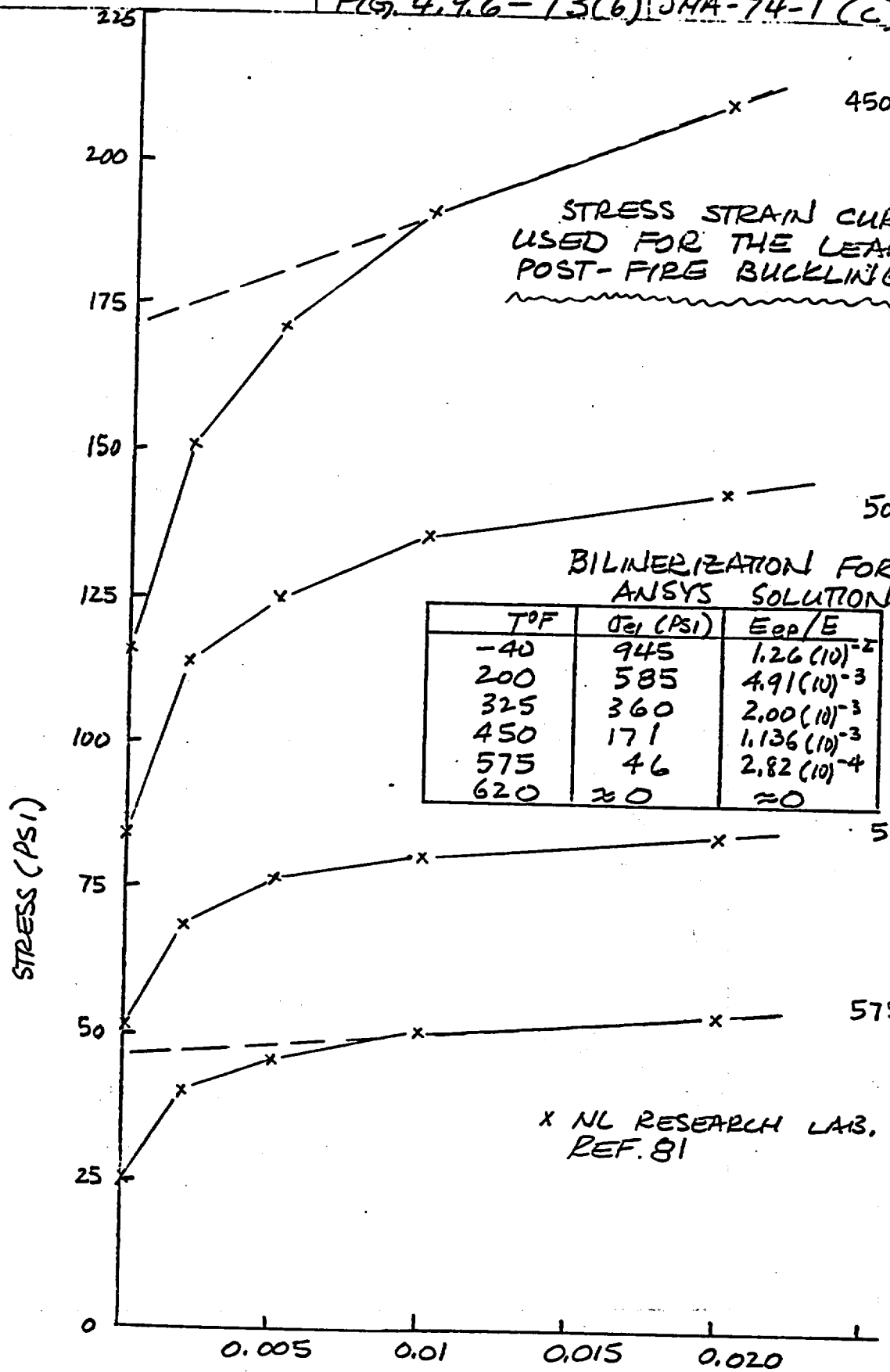

BILINERIZATION FOR ANSYS SOLUTIONS

T°F	σ_{el} (PSI)	E_{ep}/E
-40	945	$1.26(10)^{-2}$
200	585	$4.91(10)^{-3}$
325	360	$2.00(10)^{-3}$
450	171	$1.136(10)^{-3}$
575	46	$2.82(10)^{-4}$
620	≈0	≈0

X1-4-177 ≈

LOWER UNSUPPORTED PORTION OF THE INNER SHELL

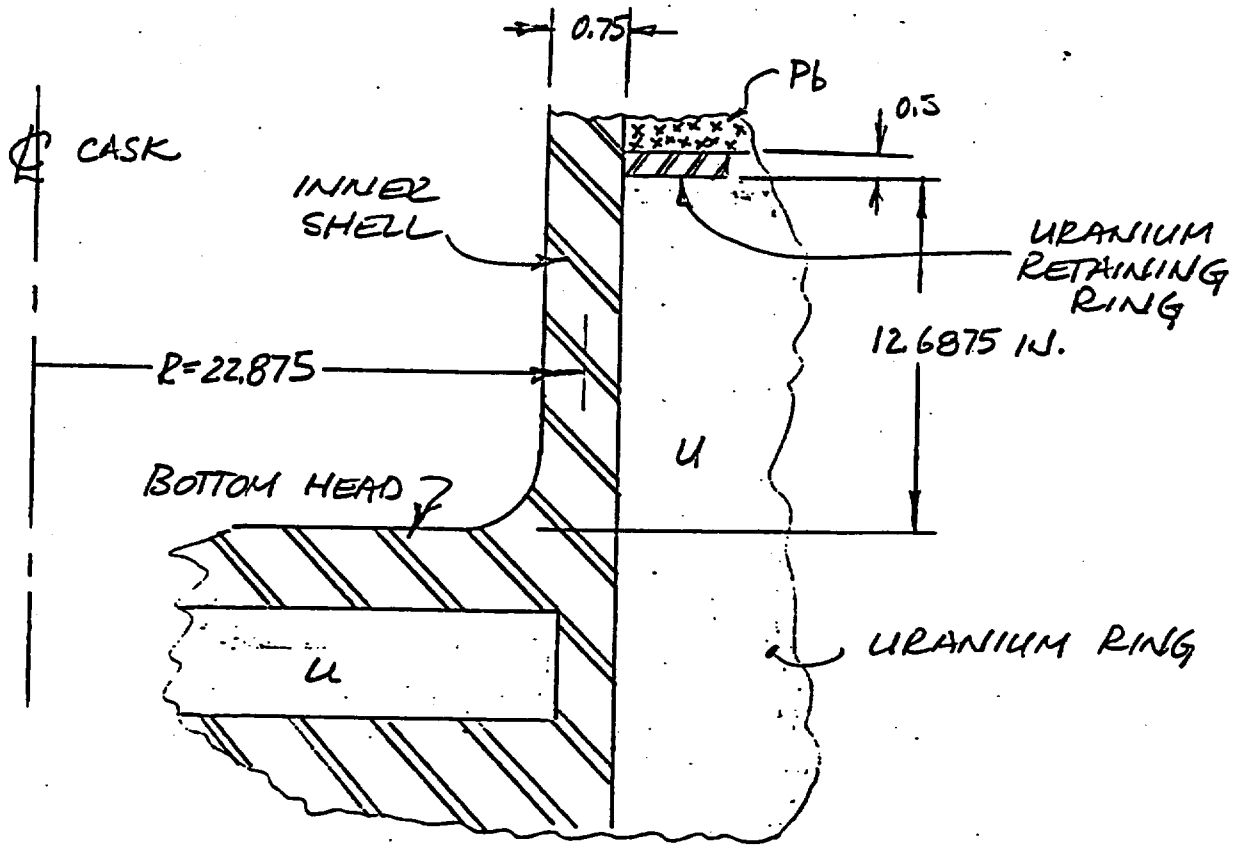

FIGURE 4.9.6-15

LEAD PRESSURE AT CASK CENTER PLANE
(FROM SMALL AXISYMMETRIC ANSYS MODEL)

POST FIRE CONDITIONS

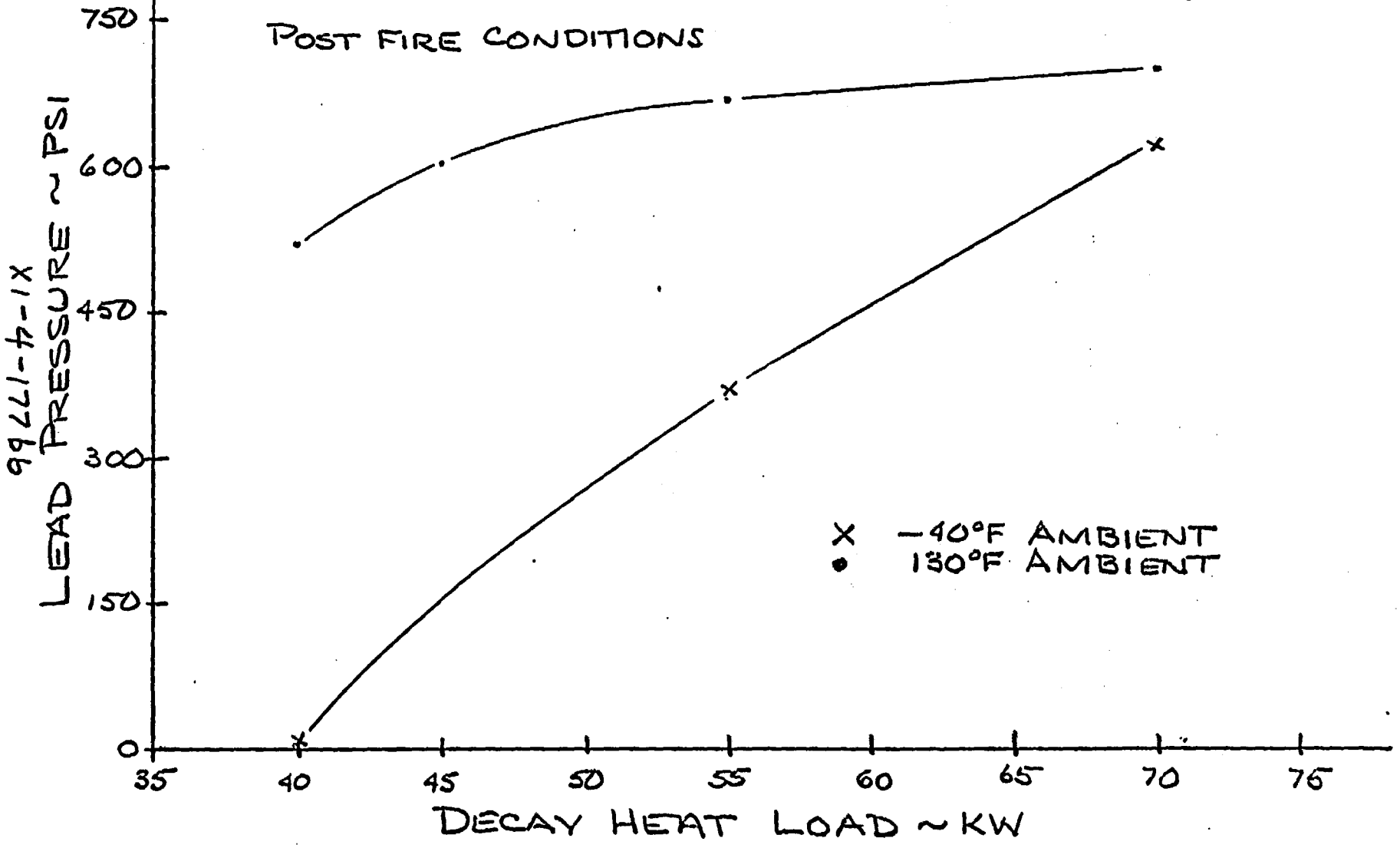

FIG. 4.9.6-15
REV. 1-1/6
JHA-74-1(C)

FIGURE 4.9.6-16. ANSYS MODEL USED FOR CIRCUMFERENTIAL CREEP SOLUTION

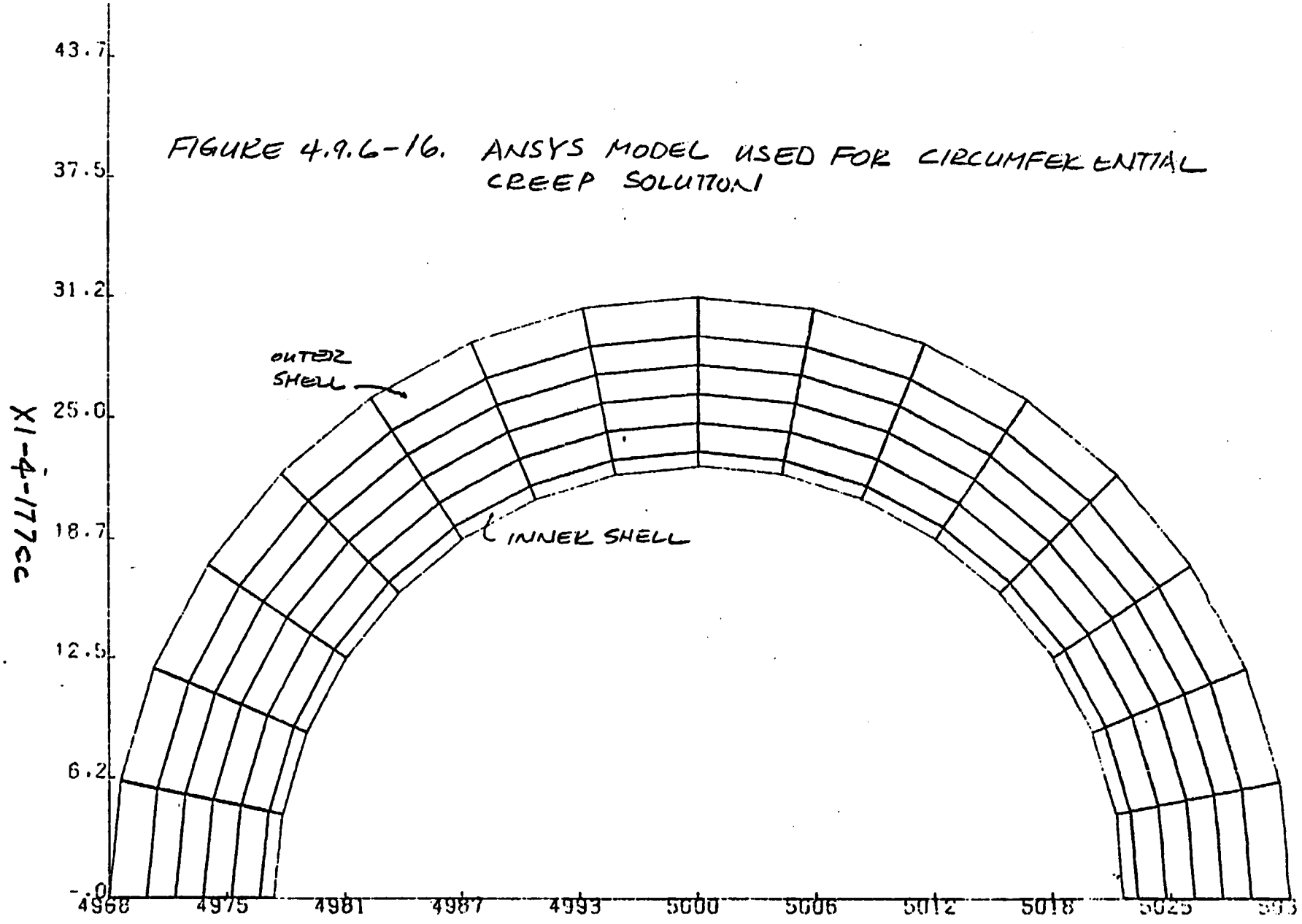

Fig. 4.9.6-16

Rev. 1-2/96

THIS PAGE INTENTIONALLY LEFT BLANK

4.9.7 Bottom Head Containment Vessel

The bottom head is loaded only by the internal pressure resulting from the post fire temperature. Maximum internal pressure (85.8 psig) exists with BWR fuel load assuming all fuel rods rupture. (Sect. 4.9.1)

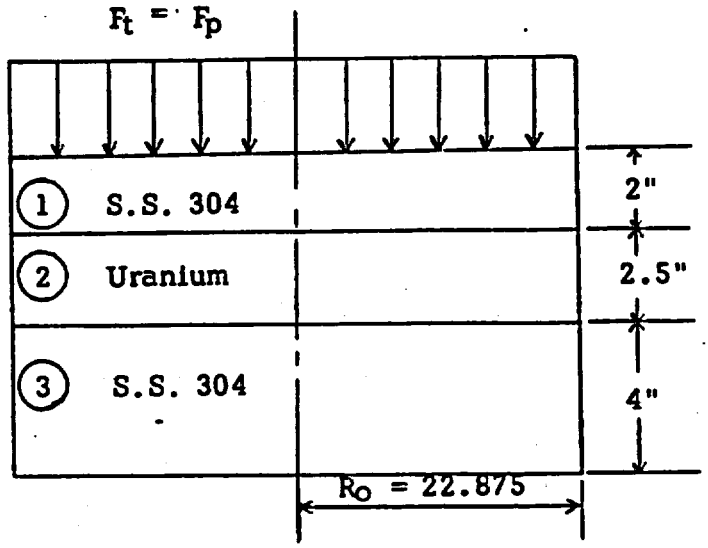

Term	(1) Inner S.S.	(2) Uranium	(3) Outer S.S.
Temp.° F	601	601	601
E, psi	25.5×10^6	23.2×10^6	25.5×10^6
v	0.3	0.22	0.3

Pressure load

$F_p = 85.8\ A$ $\qquad A = \pi(22.875^2) = 1644\ \text{in.}^2$

$F_p = 85.8 \times 1644 = 141055\ \text{lbs.}$

The three plates are constrained to have the same elastic deflection curves under lateral bending loads. Hence the deflection of each plate must be the same and the total lateral load supplied to the assembly can be divided among the individual plates in accord with each one's proportionate part of the total bending resistance. The appropropriate formulas for deflection, maximum stress are taken from Ref. 3 Table X,

Case 1 (for plates (1) , (2))

Center deflection, $y_c = \dfrac{3(1-\nu)(5+\nu)R_o^2}{16\pi Et^3} F = KF$

Max. stress at center $\sigma_c = \dfrac{3(3+\nu)}{8\pi t^2} F$

For Plate (3) the appropriate formulas for deflection, maximum stress are taken from Reference 3, Table X, Case 1.

Center deflection, $y_c = \dfrac{3(1-\nu^2)R_o^2}{16\pi Et^3} F = KF$

Max. stress at edge $\sigma_c = \dfrac{3}{4\pi t^2} F$

Equating the center deflection of the three plates gives:

$$K_1 F_1 = K_2 F_2 = K_3 F_3$$

Also, the total load imposed on the closures must equal the sum of the individual plate loads, so that :

$$F_t = F_1 + F_2 + F_3$$

Combining these equations in terms of outer plate loads, F_3 gives

$$F_t = K_3 F_3 \left(\frac{1}{K_1} + \frac{1}{K_2} + \frac{1}{K_3}\right)$$

These equations may be evaluated to obtain the force on each plate as follows:

$$F_t = F_p = 141055 \text{ lbs.}$$

Evaluating the compliance constant K gives:

$$K_1 = \frac{3\,(0.7)\,(5.3)\,(22.875^2)}{16\pi\,(25.5)\,(10^6)\,(2^3)} = 5.67959 \ (10^{-7}) \text{ in./lb.}$$

$$K_2 = \frac{3\,(0.78)\,(5.22)\,(22.875^2)}{16\pi\,23.2\,(10^6)\,(2.5^3)} = 3.50777 \ (10^{-7}) \text{ in./lb.}$$

$$K_3 = \frac{3\,(.91)\,(22.875^2)}{16\,\pi\,(25.5)\,(10^6)\,(4^3)} = 1.741385 \ (10^{-8}) \text{ in./lb.}$$

Now F_3 can be determined as follows:

$$F_t = K_3 F_3 \left(\frac{1}{K_1} + \frac{1}{K_2} + \frac{1}{K_3}\right)$$

$$141055 = 1.741385 \times 10^{-8} F_3 \left[1.760689 \times 10^6 + 2.850817 \times 10^6 + 5.742555 \times 10^7\right]$$

$$F_3 = \frac{141055}{1.0803} = 130570 \text{ lbs.}$$

$$F_1 = \frac{K_3 F_3}{K_1} = \frac{1.741385 \times 10^{-8} \times 130570}{5.67959 \times 10^{-7}} = 4003 \text{ lbs.}$$

$$F_2 = \frac{K_3 F_3}{K_2} = \frac{1.741385 \times 10^{-8} \times 130570}{3.507766 \times 10^{-7}} = 6482 \text{ lbs.}$$

Bending stress in each plate is determined as follows:

Plate (1) $\sigma_1 = \frac{3(3+v)}{8\pi t^2} F_1 = \frac{3 \times 3.3}{8\pi 2^2} \times 4003 = 394$ psi

Plate (2) $\sigma_2 = \frac{3(3+v)}{8\pi t^2} F_2 = \frac{3 \times 3.22}{8\pi 2.5^2} \times 6482 = 399$ psi

Plate (3) $\sigma_3 = \frac{3}{4\pi t^2} F_3 = \frac{3}{4\pi 4^2} \times 130570 = 1948$ psi

Calculating effective stresses on plates (1), (2), (3)

The formula for effective stress is

$$S_e = \sqrt{\frac{1}{2}} \sqrt{(\sigma_x - \sigma_y)^2 + (\sigma_y - \sigma_z)^2 + (\sigma_z - \sigma_x)^2 + 6\left(T_{xy}^2 + T_{yz}^2 + T_{zx}^2\right)}$$

Where σ_x, σ_y, σ_z are normal stresses and T_{xy}, T_{yz}, T_{zx} are shear stresses (Sect. 1.1)

Plate (1)

The highest stress area is at the center portion of the outer surface.

$\sigma_x = 394$ psi (radial Stress)

$\sigma_y = 394$ psi (tangential stress)

$\sigma_z = \frac{137052}{1644} = 83.36$ psi (axial stress)

$T_{xy} = T_{yz} = T_{zx} = 0$

$$S_{e3} = \sqrt{\frac{1}{2}} \sqrt{(394 - 394)^2 + (394 - (-83.36))^2 + (-83.36 - 394)^2}$$

$$S_{e3} = 477 \text{ psi}$$

Allowable stress ($0.8 S_{aa} = 0.7 S_u$) at 601°F for 304 S/S from Sect. 1.1 under containment vessel and Sect. 1.2 equals to $0.7 \times 58500 = 40950$ psi

$$M.S. = \frac{40950}{477} - 1 = 85$$

Plate (2)

The highest stress area is at the center portion of the outer surface.

$\sigma_x = 399$ psi (radial stress)

$\sigma_y = 399$ psi (tangential stress)

$\sigma_z = \frac{130570}{1644} = 79.4$ psi (axial stress)

$T_{xy} = T_{yz} = T_{zx} = 0$

$$S_{e4} = \sqrt{\frac{1}{2}} \sqrt{(399 - 399)^2 + (399 - (-79.4))^2 + (-79.4 - 399)^2}$$

$$S_{e4} = 478 \text{ psi}$$

Allowable stress ($S_{aa} = 0.9 S_u$) at 601°F for URANIUM from Sect. 1.1 under noncontainment structure and Sect. 1.2 equals to $0.9 \times 38500 = 34650$ psi

$$M.S. = \frac{34650}{478} - 1 = 71.4$$

Plate (3)

The highest stress area is at the edge portion of the inner surface.

σ_x = 1948 psi (radial stress)

From Ref. 3, Table X, Case 6

$$\sigma_y = \frac{3\,v\,F}{4\,\pi\,t^2} = \frac{3 \times 0.3 \times 130570}{4\,\pi\,4^2} = 584 \text{ psi (tangential stress)}$$

$$\sigma_z = \frac{130570}{1644} = 79.4 \text{ (axial stress)}$$

$$T_{zx} = \frac{130570}{45.75\,\pi\,4} = 227 \text{ psi (shear stress)}$$

$$T_{yz} = T_{xy} = 0$$

$$S_{e4} = \sqrt{\frac{1}{2}}\sqrt{(1948-584)^2 + (584-(-79.4))^2 + (-79.4-1948)^2 + 6(227}$$

S_{e4} = 1833 psi

Allowable stress ($S_{aa} = 0.9\,S_u$) at 601°F for 304 S/S from Sect. 1.1 under noncontainment structure and Sect. 1.2 equals to

0.9 x 58500 = 52650 psi

$$\text{M.S.} = \frac{52650}{1833} - 1 = 27.7$$

4.9.8 Inner Closure (For BWR fuel)

This analysis is performed on the inner closure head to determine the stresses due to internal pressure. The pressure assumed is that due to fuel pin rupture. The BWR case is chosen since if this fuel ruptures it causes higher fuel cavity pressures.

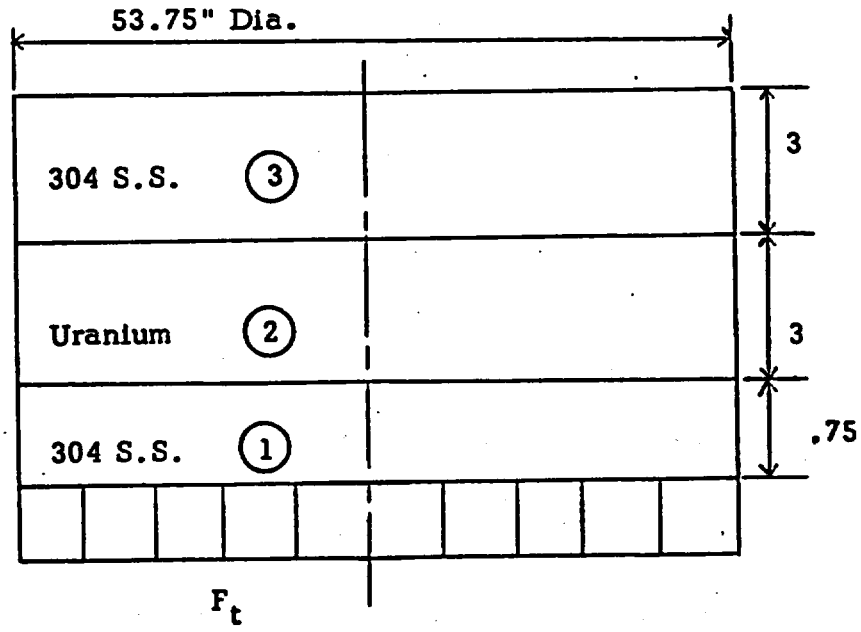

TERM	Inner S.S.	Uranium	Outer S.S.
Temp F	601	601	601
E. psi X 10^6	25.5	23.2	25.5
v	.3	.22	.3

The three plates are constrained to have the same elastic deflection curves under lateral bending loads. Hence the deflection of each plate must be the same and the total lateral load applied to the assembly can be divided among the individual plates in accordance with each ones proportionate part of the total bending resistance. The appropriate formulas for deflection and maximum stress are taken from reference 3 , table X, case 1.

Center deflection, $Y_c = \frac{3(1-r)(5+r)\,Ro^2}{16\,\pi\,Et^3} \quad F = KF$

Max. stress at center, $\sigma_c = \frac{3(3+r)}{8\pi t^2} \quad F$

Equating the center deflection of the three plates gives

$$K_1 F_1 = K_2 F_2 = K_3 F_3$$

Also, the total load imposed on the closure must equal the sum of the individual plate loads so that

$$F_T = F_1 + F_2 + F_3$$

Combining these equations in terms of the outer plate load, F_3 gives

$$F_t - K_3 F_3 \frac{1}{K_1} + \frac{1}{K_2} + \frac{1}{K_3}$$

These equations may be evaluated to obtain the force on each plate as follows. The internal pressure due to fuel rupture is 85.8 psig (Section 4.9)

$$A = \pi r^2 = \pi (26.875^2) = 2269 \text{ in}^2$$

$$F_p = 85.8A = 194680 \text{ lbs.}$$

$$F_t = F_p$$

Evaluating the compliance constant gives

$$K_1 = \frac{3\,(.7)\,(5.3)(26.875)^2}{16\pi(25.5 \times 10^6)\,(.75)^3} = 1.4866 \times 10^{-5} \text{ in./lb.}$$

$$K_2 = \frac{3\,(.78)\,(5.22)\,(26.875)^2}{16\pi(23.2 \times 10^6)\,(3)^3} = 2.80196 \times 10^{-7} \text{ in./lb.}$$

$$K_3 = \frac{3\,(.7)\,(5.3)\,(26.875)^2}{16\pi(25.5 \times 10^6)\,(3)^3} = 2.3228 \times 10^{-7} \text{ in./lb.}$$

Now F_3 can be found from the previous equations as follows.

$$194680 = 2.3228 \times 10^{-7} F_3 \left[6.7267 \times 10^4 + 3.5689 \times 10^6 \right.$$
$$\left. 4.3051 \times 10^6\right]$$

$$F_3 = \frac{194680}{1.8446}$$

$$= 105540 \text{ lbs.}$$

$$F_1 = \frac{K_3 F_3}{K_1} = \frac{2.3228 \times 10^{-7} (105540)}{1.4866 \times 10^{-5}} = 1649 \text{ lbs.}$$

$$F_2 = \frac{K_3 F_3}{K_2} = \frac{2.3228 \times 10^{-7} (105540)}{2.80196 \times 10^{-7}} = 87493 \text{ lbs.}$$

Plate (1) max. stress $= \frac{3 (3.3) (1649)}{8 \pi (.75)^2} = 1155$ psi

Plate (2) max. stress $= \frac{3 (3.22) (87493)}{8 \pi (3)^2} = 3736$ psi

Plate (3) max. stress $= \frac{3 (3.3) (105540)}{8 \pi (3)^2} = 4619$ psi

Calculating effective stresses on plate (1), (2), (3)

The proper formula for effective stress equals

$$S_e = \sqrt{\frac{1}{2}} \sqrt{(\sigma_x - \sigma_y)^2 + (\sigma_y - \sigma_z)^2 + (\sigma_z - \sigma_x)^2 + 6(T_{xy}^2 + T_{yz}^2 + T_{zx}^2)}$$

where σ_x, σ_y, σ_z are normal stresses, T_{xy}, T_{yz}, T_{zx} are shear stresses. (Sect. 1.1)

Plate (1) highest stress area is at the center portion of the outer surface.

$\sigma_x = 1155$ psi (Radial Stress)

$\sigma_y = 1155$ psi (Tangential Stress)

$\sigma_z = 85.07$ psi (Axial Stress) $\qquad \sigma_z = \frac{193031}{2269} = 85.07$ psi

$T_{xy} = T_{yz} = T_{zx} = 0$

$$S_{e3} = \sqrt{\frac{1}{2}} \sqrt{(1155 - 1155)^2 + (1155 - (-85.07))^2 + (-85.07 - 1155)^2}$$

$S_{e3} = 1240$ psi

Allowable stress ($.8S_{aa} = 0.7\ S_u$) at 601°F for 304 S/S from Sect. 1.1 under containment vessel and Sect. 1.2 equals to $0.7 \times 58500 = 40950$ psi

$$M.S. = \frac{40950}{1240} - 1 = 32$$

Plate (2) highest stress area is at the center portion of the outer surface.

$\sigma_x = 3736$ psi (Radial Stress)

$\sigma_y = 3736$ psi (Tangential Stress)

$\sigma_z = 46.5$ psi (Axial Stress) $\qquad \sigma_z = \frac{10538}{2269} = 46.5$ psi

$T_{xy} = T_{yz} = T_{zx} = 0$

$$S_{e3} = \sqrt{\frac{1}{2}}\sqrt{(3736 - 3736)^2 + (3736 - (-46.5))^2 + (-46.5 - 3736)^2}$$

$= 3782.5$ psi

Allowable stress ($.8\ S_{aa} = 0.7\ S_u$) at 601°F for URANIUM from Sect. 1.1 under containment vessel and Sect. 1.2 equals to $0.7 \times 38500 = 26950$ psi

$$M.S. = \frac{26950}{3782.5} - 1 = 6.12$$

Plate (3) highest stress area is at the center portion of the outer surface.

$\sigma_x = 4619$ psi (Radial Stress)

$\sigma_y = 4619$ psi (Tangential Stress)

$\sigma_z = 0$ (Axial Stress)

$T_{xy} = T_{yz} = T_{zx} = 0$

$$S_{e3} = \sqrt{\frac{1}{2}}\sqrt{(4619 - 4619)^2 + (4619 - 0)^2 + (0 - 4619)^2}$$

$S_{e3} = 4619$ psi

$$M.S. = \frac{40950}{4619} - 1 = 7.86$$

THIS PAGE INTENTIONALLY LEFT BLANK

4.9.9 Containment Vessel Valves

The containment vessel valve assembly uses two metal O-ring seals to provide leaktight joints between base plate, cover and forging (Drawing 70651F). Elastomer O-ring seals are also provided at these joints to facilitate operational checks of the metal seals. The metal O-rings are silver plated Inconel, which will withstand temperatures up to 1300°F. Temperatures at the valve assembly location in the fire and post fire conditions will not exceed 600°F (See section VIII).
At the seal seating load of 700 lb/inch provided by the bolting preload, the helium leak rate of the seal will be 10^{-6} cc/sec or less (p.VI-22, Ref. 83)

Maximum pressure in the containment vessel from the fire accident is 85.8 psig. (sect 4.9.1). The resulting load on the valve assembly joint is $P_1 = (\pi/4)(3.094^2)(85.8) = 645$ lb.
seal seating load, $P_2 = 6804$ lb. (Sect. 4.4.8)
total load per bolt, $F = (645 + 6804)/4 = 1862$ lb.
Since the bolts are each preloaded to 2533 lb (sect. 4.6.4), the joint seal is maintained in the fire accident.

M.S. = (2533/1862) -1 = 0.36

5.0 REFERENCES

1. ANSYS, Engineering Analysis Program, Swanson Analysis Systems, Inc., Elizabeth, Pennsylvania, 1973.

2. Meeting of McPherson Associates, Inc's. Personnel with Dr. John Swanson of Swanson Analysis Systems, Inc. on 8 April 1974.

3. Roark, "Formulas for Stress and Strain", 4th Ed., McGraw-Hill Book Co. New York, 1954.

4. Baker, Kovalevsky, Rish, "Structural Analysis of Shells", McGraw-Hill Book Co., New York, 1972.

5. ASME, "Pressure Vessel Code", Section VIII, Div. 2 and Section III.

6. Phillips, "Introduction to Plasticity", Ronald Press Co., New York, 1956.

7. Nadai, "Plasticity", McGraw-Hill, New York, 1931.

8. Timoshenko, "Strength of Materials, Part II", 2nd Ed., D. VanNostrand Co., New York, 1945.

9. ASME, "Criteria of Section III of the ASME Boiler and Pressure Vessel Code for Nuclear Vessels", 1964.

10. Hodge, "Shakedown of Elastic-Plastic Structures", in Residual Stress in Metals and Metal Construction, Osgood (Edit.), pp. 163-185, Reinhold Publishing Corp., New York, 1954.

11. Shigley , "Mechanical Engineering Design", 2nd Ed., McGraw-Hill Book Co., New York, 1972.

12. Simmons and Van Echo (Prep.) "The Elevated Temperature Properties of Stainless Steel, ASTM Data Series Publications DS 5-51, American Society for Testing and Materials, Philadelphia, 1965.

13. "Preliminary Design Criteria and Analysis Methods for F.F.T.F. Valves", January 27, 1971, Crane Report CR-0412.

14. "Alcoa Aluminum Handbook", Aluminum Company of America, Pittsburgh, Pennsylvania.

15. Tipton, C. R. Jr., (Edit.), "Reactor Handbook", 2nd Ed., Vol. 1, p. 486, Materials, Interscience Publishers, Inc., New York, 1960.

16. Baumeister and Marks, "Standard Handbook for Mechanical Engineers", 7th Ed., McGraw-Hill Book Co., New York, 1967.

17. Tipton, C. R. Jr., (Edit.), "Reactor Handbook", 2nd Ed., Vol. 1, p. 124, Interscience Publisher, Inc., New York, 1960.

18. Goldsmith, A., et. al, "Handbook of Thermophysical Properties of Solid Materials", revised Ed., Vol. 1, The MacMillan Co., New York, 1961.

19. Anderson, W. K. and Theilacker, J. S. (Edit.), "Neutron Absorber Materials for Reactor Control", United States Atomic Energy Commission, 1962.

20. Tietz, E. Thomas, "Determination of the Mechanical Properties of a High Purity Lead and a 0.05% Copper-lead Alloy", Stanford Research Institute, Menlo Park, California, April 1958, WADC Technical Report 57-695, ASTIA Document No. 151165.

21. W. Hoffman, "Lead and Lead Alloys", English Translation of the second revised German Edition, Springer-Verlag, New York - Heidelber, Berlin 1970.

22. Calvert Cliffs, Unit 1 and 2 FSAR, Baltimore Gas and Electric Co., Dockett 50-317.

23. "Dowtherm SR-1 Heat Transfer Fluid Catalog", Dow Chemical Co., 1970.

24. "1972 Annual Book of ASTM Standards" Part 1, Steel Piping, Tubing, and Fittings American Society for Testing and Materials, Philadelphia, 1972.

25. "Republic Precipitation Hardenable Stainless Steels", Republic Steel Corporation, Copyright 1962.

26. "The Influence of Impact Velocity on the Tensile Characteristics of Some Aircraft Metals and Alloys" , NACA-TN-868, Washington, October 1942.

27. "Strength of Metal Aircraft Elements", Military Handbook, MIL-HDBK-5, Armed Forces Supply Support Center, Washington 25, D.C.

28. "Ricon", Technical Data Bulletin No. RAD. 100, The Richardson Company, 2700 Lake Street, Melrose Park, Illinois 60160.

29. "Polybutadiene, Polyetnylene Copolymer Sheets, Virgin and Borated", MIL-P-24468 (Ships), October 20, 1972.

30. Scott, D. B., "Physical and Mechanical Properties of Zircaloy 2 and Zircaloy 4", WCAP-3269-41, May 1965.

31. "The Engineering Properties of Viton Fluoroelastomer", E. I. duPont deNemours and Co. (Inc.), Elastomers Chemical Department, Wilmington, Delaware 19898.

32. "Stresses From Radial Loads and External Moments in Cylindrical Pressure Vessels", P. P. Bijlaard Welding Research Supplement, December 1955.

33. Bruhn, E. F. "Analysis and Design of Flight Vehicle Structures", Tri-State Offset Co., Cincinnati, Ohio.

34. Timoshenko, "Theory of Plates and Shells", First Edition, McGraw-Hill Book Co., New York, 1940.

35. Kaufman, J. G., "Summary Report, The Effects of High Strain Rates on the Mechanical Properties of Aluminum Alloys", Alcoa Research Laboratories, Report No. 9-60-31 (1960), ASTIA, Document No. AD 249-964.

36. Harris and Crede (Edit.), "Shock and Vibration Handbook", Vol. 1, p. 14, and Vol. 3, pp. 45-21 thru 45-39, McGraw-Hill Book Co., New York 1961.

37. Guins and Tack (Edit.), "Anthology of Rail Vehicle Dynamics", Vol. 1 Freight Car Impact and Vol. 2 Effects of Train Action and Rail Car Vibration, ASME, New York, 1971.

38. Settles, J. C., "Vibration and Shocks in Freight Cars as Causes of Loading Damage", pp. 1622-1628, ASME Trans., November 1958.

39. Lahood, J. W., "Shock and Vibration Data Obtained From Trucks and Rail Shipment", pp. 99-108, Shock and Vibration Bulletin No. 33 part IV March 1964.

40. New York Central Railroad, "The Railroad Environment - A Guide for Shippers and Railroad Personnel", 9-17 Section II, III, IV, 1960.

41. Gens, M. B., "The Rail Transport Environment", pp. 14-20, Journal Environment Science, July - August 1970.

42. Clarke and Reddi, "Structural Integrity of Shipping Containers for Radioactive Materials, Part I : Study of Transport Operation and Container Construction" pp. 5-16, USAEC Report NYO-9859, July 1962.

43. "Aerospace Structural Metals Handbook" Revised March 1967.

44. "A survey of Environmental Conditions Incident to the Transportation of Materials" - General Transportation Corporation - October 1971 (NTIS PB-204 442)

45. "1974 Annual Book of ASTM Standards" Part 4, Steel Structural, Reinforcing Pressure Vessel Railway, American Society for Testing and Materials, Philadelphia, 1974.

46. "1974 Annual Book of ASTM Standards, Part 6, Copper and Copper Alloys, American Society for Testing and Materials, Philadelphia, 1974.

47. "HK Porter Co.," Thermoid Div. Trenton New Jersey.

48. Baron, H. G., "The Stress-Strain Curves of Some Material and Alloys at Low Temperatures and High Rates of Strain", Metallurgy Report 22/54, Armament Research Establishment, Ministry of Supply, UK, August 1954 (ASTIA AD No. 40921)

49. Manjoine, M J., "Influence of Rate of Strain and Temperature on Yield Stresses of Mild Steel", J. Appl. Mech., December 1944.

50. Clark and Wood, "The Tensile Impact Properties of Some Metals and Alloys", Trans. ASM, V. 42, pp. 45-74 (1950).

51. Goldsmith, Werner, "Impact", Edward Arnold Publ., London (1960)

52. Cristescu, N., "Dynamic Plasticity", North-Holland Publ. G., Amsterdam (j. Wiley & Sons, N.Y.) (1967).

53. Timoshenko, "Theory of elasticity", First Ed., Mc Graw-Hill Book Company, Inc., New York and London, 1934.

54. "Creep of Engineering Materials" by Finnie and Heller, 1959. McGraw-Hill Book Company.

55. Manson, S. S., "Thermal Stress and Low-Cycle Fatigue," McGraw-Hill Book Co., New York (1966).

56. Norris et. al. "Structural Design for Dynamic Loads," McGraw-Hill Book Co., New York, 1959.

57. R. Szilard, "Theory and Analysis of Plates", Prentice-Hall, Inc., Englewood Cliffs, N. J.

58. S. Timoshenko, "Theory of Elasticity", McGraw-Hill Book Co.,Inc., New York and London, 1936.

59. Save and Massonnet, "Plastic Analysis and Design of Plate, Shells and Disks", American Elsevier Publishing Co., Inc., New York, 1972.

60. "Steels for Elevated Temperature Service", United States Steel Co. Cat. No. ADUSS 43-1089-04.

61. "Engineering Handbook", Engineering Master Catalog, 1971.

62. Sartory, Walter K.,"PLACRE Computer Code", Oak Ridge National Laboratory, Oak Ridge, Tenn., 1972.

63. Sandor, Bela H., "Fundamentals of Cyclic Stress and Strain", University of Wisconsin Press, Madison, Wis., 1972.

64. "1974 SAE Handbook", Society of Automotive Engineers, New York, N.Y.

65. Communication from Grey Tool Co. pertaining to Greyloc seal ring, size 462 (Dwg. I-4633), M. E. Beasley, Mgr. Ind. Prod., Box 2291, Houston, Texas 77001.

66. Safety Analysis Report for NLI 1/2 LWT Cask, NRC Docket No. 71-9020

67. Letter from Armco Steel Corportaion dated September 11, 1975

69. "Manual of Steel Construction", American Institute of Steel Construction, New York (7th Ed., 1970)

69. "Fasteners Reference Issue", vol. 37, no. 6, Machine Design, Penton Publishing Co., Cleveland, Ohio (March 11, 1965)

70. D.O. Brush, E. V. Pittner., "Influence of Cushion Stiffness on the Stability of Cushion - Loaded Cylindrical Shells", Lockheed Missles and Space Company, Palo Alto, California. AIAA Journal, Vol. 3, No. 2, February 1965.

71. Nuclear Systems Materials Handbook (Vol. 1, Design Data) Hanford Eng. & Dev. Lab. (HEDL) Richland, Wash.

72. S. Radhakrishnan, Plastic Buckling of Circular Cylinders, Journal of Aeronautical Science., Vol. 23, No. 9., Sept. 1956

73. North American Aviation, Inc., Vol. 2, Los Angles Division, Report Number Ref. CP-4694, Jan. 1957.

74. Union Carbide and Carbon Research Laboratory data, as quoted in Metals Handbook, Am. Soc. Metals, 1948, p. 204.

75. "Mechanical and Physical Properties of the Austenitic Chromium-Nickel Stainless Steels at Sub-Zero Temperatures". The International Nickel Company, Inc., New York, 3rd Ed., March 1970.

76. "Handbook on Materials for Superconducting Machinery". Metals and Ceramics Information Center, Battelle, Columbus Laboratories, Report No. NCIC-HB-04.

77. C. J. Guntner and R. P. Reed: "Mechanical Properties of Four Austenitic Stainless Steels at Temperatures Down to 20°K." Advances in Cryogenic Engineering, Plenum Press, New York, Vol. 6, 1961.

78. Nerva Program, Material Data Book, Aerojet General (1964).

79. R. Michael McClintock and Hugh P. Gibbons; "Mechanical Properties of Structural Materials at Low Temperature", National Bureau of Standards, Monograph 13, Issued June 1, 1960.

80. John L. Everhart, W. Ear Lindlief, James Kanegis, Pearl G. Weissler and Freida Sieget. "Mechanical Properties of Metals and Alloys", United States, Washington Printing Office. Washington, 1943.

81. NL Industries internal test report on tensile properties of chemical lead at elevated temperatures, C. Gallagher, Central Research Laboratory, Hightstown, N. J. (Feb. 1976)

82. Parker O-Ring Handbook, OR 5700, Jan. 1975, Parker Seal Co., Lexington, Ky.

83. Kalasky, James E., "Characteristics of Metal O-Rings and Relationship to Sealing Capabilities", Nat'l. Conf. on Fluid Power & Fluid Power Society, Oct. 1970.

84. Communication of June 7, 1978 from J. H. Swartz Co. cites 2000 lb/in. seating laod for United Aircraft Products seal P/N U701756 per K. Moralles, UAP, Dayton, Ohio; also, closure lateral movement of 0.010 in. will not affect seal integrity.

85. Biach Industries, Inc., Cranford, N. J.: Operating and Maintenance Manual for Stud Tensioner Model No. 1-30471 (Biach Job No. 3639)

THIS PAGE INTENTIONALLY LEFT BLANK

SECTION XI

APPENDIX A

Comment on p. 4 of enclosure to NRC letter of 8/28/75 concerning section 4.4.7, Absorber Sleeves in Top End Impact.

Response

Comment questioned whether information taken from Szilard (p.701 ref. 57) was applied correctly in our buckling analysis of the absorber sleeve cladding. Pertinent pages are attached from Szilard and from two sources he cites (Pflüger, Gerard and Becker).

1) Both Pflüger (pp. 399, 397) and Gerard (pp. 80, 64) verify the value of $\lambda = 7$ for the buckling coefficient, since this is the minimum value for an infinitely long plate. The cladding length/width ratio is a/b = 156.75/9.6 = 16.3, and Pflüger states that for values of $a/b > 2/3$ the buckling coefficient is at the minimum of 6.97.

2) It is evident from discussions in Gerard (pp. 7, 67, 12-15), Szilard (p. 506), and Pflüger (pp. 16, 77) that the unloaded edges of a plate loaded in uniaxial compression may displace freely in the loading direction. In the derivation of buckling equations no restrictions are placed on plate displacements in the loading direction (in-plane forces are neglected). Figure 1 of Gerard (p.67) illustrates that the buckle pattern for minimum critical load cannot develope for the full length of the plate unless the plate can deflect freely in the loading direction.

Theory and Analysis of Plates

CLASSICAL AND NUMERICAL METHODS

Rudolph Szilard, Dr.-Ing., PE.

Professor of Civil Engineering
Adjunct Professor of Ocean Engineering
University of Hawaii

PRENTICE-HALL, INC. *Englewood Cliffs, New Jersey*

Library of Congress Cataloging in Publication Data

SZILARD, RUDOLPH
Theory and analysis of plates: classical and numerical methods.

(Civil engineering and engineering mechanics series)
Includes bibliographical references.
1. Plates (Engineering) I. Title.
TA660.P6S95 624'.1776 73-6699
ISBN 0-13-913426-3

To the memory of my father,
Dipl.-Ing. Rudolph Szilard (Seybold), Sr.

CIVIL ENGINEERING AND ENGINEERING MECHANICS SERIES

N. M. Newmark and W. J. Hall, editors

10 9 8 7 6 5 4 3 2 1

Printed in the United States of America

PRENTICE-HALL INTERNATIONAL, INC., London
PRENTICE-HALL OF AUSTRALIA, PTY. LTD., Sydney
PRENTICE-HALL OF CANADA, LTD., Toronto
PRENTICE-HALL OF INDIA PRIVATE LIMITED, New Delhi
PRENTICE-HALL OF JAPAN, INC., Tokyo

Case No.	Structural System and In-Plane Loading	Critical Load	Elastic Buckling Coefficients	Source	Notes
158	Subcases according to type of support along the unloaded edges General case Fixed or simply supported Free edge Free edge	$(\bar{n}_x)_{cr} = k_{cr}\frac{\pi^2 D}{b^2}$	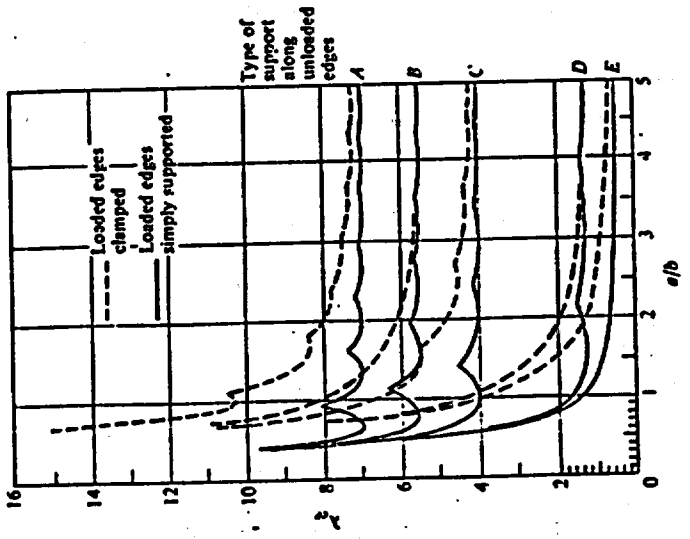	[A26], [A29], and [A30]	Use solid lines if loaded edges are simply supported. Use dashed lines if the loaded edges are clamped. For orthotropic plates with all edges simply supported, use aspect ratio given in Eq. (3.6.27).

701

In the mathematical formulation of classical plate buckling by the energy methods, we again use the *neutral state of equilibrium* at which bifurcation of displacements occurs, as discussed in Sec. 6.1. Furthermore, it is assumed that the in-plane displacements of the plate are due to the small bending (created by the buckling) and not due to the in-plane shortening. The reason for this assumption is clear if one considers that our datum configuration is the stable equilibrium condition of the plate immediately prior to buckling. Thus, up to this point, the strain energy due to compression of the middle surface equals the work done by the external in-plane forces and therefore cancels out ($\Pi_0 = 0$) in the energy equations.

a. Rayleigh's Method. Rayleigh's powerful method [6.3.1] is based on the principle of *conservation of energy* (6.1.2).

In formulating the buckling problem of a flat plate by energy methods, we first assume that the plate, subjected to

$$\bar{n}_x = -\lambda \bar{n}_{x0}, \qquad \bar{n}_y = -\lambda \bar{n}_{y0}, \qquad \text{and} \qquad \bar{n}_{xy} = -\lambda \bar{n}_{xy0} \tag{6.3.1}$$

in-plane edge forces,† is in a stable equilibrium. Next, the load is gradually increased. As we increase the load factor, λ, at a certain value, the plate will pass from its flat shape to its curved shape without changing its total potential; thus

$$W_i^* + \lambda W_e^* = U_b^*(w) + \lambda V^*(w) = 0. \tag{6.3.2}$$

Based on our previous discussion,‡ this expression is only a function of the lateral deflections. As already mentioned, the total potential, corresponding to the stable state of equilibrium, Π_0, has been eliminated from Eq. (6.3.2). Consequently, here we are only concerned with the total potential pertinent to the *neutral* state of equilibrium.

Since expansion of Eq. (6.3.2) yields only one algebraic equation, its use is limited to one undetermined coefficient, c, in the expression of the deflections

$$w(x, y) = cf(x, y) = cX(x)\,Y(y). \tag{6.3.3}$$

Furthermore, it is required that Eq. (6.3.3) satisfy at least the geometrical boundary conditions.

In Eq. (6.3.2) U_b^* represents the bending part of the strain energy, introduced in Sec. 2.5. The potential of the external forces is the negative work done by the external forces ($V^* = -W_e^*$) which remain constant during buckling, as previously defined. Since we have assumed that as the middle surface bends no membrane stresses are produced, but the edges draw together creating in-plane displacements; thus, we can neglect the membrane part of the strain energy ($U_m^* = 0$). From Fig. 3.1.2 the in-plane displacement in the X directions is

$$u^* = ds - dx \simeq \frac{1}{2}\left(\frac{\partial w}{\partial x}\right)^2 dx. \tag{6.3.4}$$

† See preceding sections for the definition of $\bar{n}_{x0}$, $\bar{n}_{y0}$, and $\bar{n}_{xy0}$.
‡ See also Sec. 6.1.

Stabilitätsprobleme der Elastostatik

Von

Dr.-Ing. habil. Alf Pflüger
Professor an der Technischen Hochschule Hannover

Zweite neubearbeitete Auflage

Mit 461 Abbildungen

Springer-Verlag
Berlin/Göttingen/Heidelberg/New York
1964

Vorzeichen in (21) gilt, $\varphi = \varphi_m$ und $\vartheta = \frac{\pi}{2}$ sein muß. Wir erhalten dann

$$C_2 = K \int_0^{\frac{\pi}{2}} \frac{d\vartheta}{\sqrt{1 - k^2 \sin^2 \vartheta}}$$

und damit für (21) die endgültige Form

$$x = K \left(\int_0^{\frac{\pi}{2}} \frac{d\vartheta}{\sqrt{1 - k^2 \sin^2 \vartheta}} \pm \int_0^{\vartheta} \frac{d\vartheta}{\sqrt{1 - k^2 \sin^2 \vartheta}} \right). \tag{23}$$

Diese beiden Integrale stellen die „LEGENDREsche Normalform der elliptischen Integrale erster Gattung" dar. Die erforderliche Umformung von (20) ist damit erledigt.

Für gegebene Werte der Steifigkeiten, der Belastung und des Winkels φ_m können wir nun auf Grund der vorliegenden Tabellenwerke zunächst x als Funktion von ϑ und daraus φ in Abhängigkeit von x erhalten. Aus (17a) folgt weiter die Dehnung ε. Will man auch noch die Verschiebungen u und w ermitteln, so berechnet man am einfachsten aus (14) die Ableitungen u' und w' und erhält dann u und w selbst durch eine Integration über x, die sich z. B. nach irgendeinem der üblichen numerischen Integrationsverfahren leicht erledigen läßt.

c) Weitere Ergebnisse und Näherungsformeln

Aus den bereits aufgestellten Formeln seien noch einige Beziehungen abgeleitet, die für die dann folgende ausführliche Besprechung des Rechnungsergebnisses von Nutzen sind. Nach den obigen Ausführungen läßt sich die Bestimmung des Verformungszustandes des Stabes leicht durchführen, wenn die Belastung P und die Anfangssteigung φ_m gegeben sind. Die Stablänge l ist dabei nicht als vorgegeben anzusehen, sondern ist erst ein Ergebnis der Rechnung. Praktisch wird natürlich meist umgekehrt P und l gegeben und φ_m gesucht sein. Es ist daher von Interesse, eine Beziehung zwischen P, l und φ_m aufzustellen.

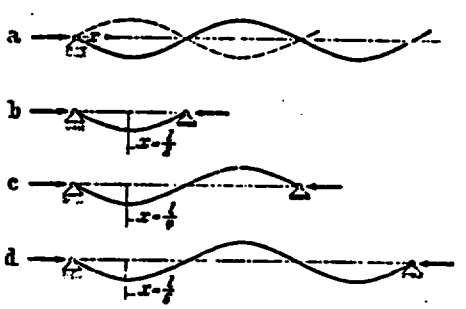

Abb. 11a–d.
Verschiedene Biegelinien des Knickstabes.

Hierzu müssen wir uns zunächst eine allgemeingültige wichtige Eigenschaft der Biegelinie des ausgeknickten Stabes klarmachen. Ermittelt man die Knickform in der oben beschriebenen Weise aus (23), so stellt man bei Benutzung der Formeln und Tabellen, die für die hier in Frage kommenden elliptischen Funktionen gelten, fest, *daß der Winkel φ und damit auch die Durchbiegung w einen periodischen Verlauf über x haben*[1]. Wir bekommen also für die Biegelinie z. B. den in Abb. 11a dargestellten wellen-

[1] Vgl. auch z. B. FRANK-MISES: Differentialgleichungen und Integralgleichungen der Mechanik und Physik, Braunschweig 1930, S. 167.

Abschnitt IV

Zwei- und dreidimensionale Probleme

Übersicht über Abschnitt IV: Es werden die Schwierigkeiten behandelt, die sich bei der Festlegung des Spannungs- und Verzerrungszustandes und der Aufstellung des Hookeschen Gesetzes ergeben, wenn das zu untersuchende System als zwei- oder gar dreidimensionales Kontinuum berechnet werden muß. Um zu möglichst einfachen Ansätzen zu kommen, erweist es sich dabei als notwendig, den Tensorcharakter des Spannungs- und Verzerrungszustandes bei nicht mehr kleinen Verformungen näher zu untersuchen. Es werden zunächst die Verhältnisse im Zweidimensionalen betrachtet; die Erweiterung auf das Dreidimensionale ist dann einfach. Zum Schluß wird auf die Besonderheiten hingewiesen, die bei Temperaturwirkungen zu beachten sind.

A. Allgemeines

Bei allen bisher aufgestellten Sätzen und Ableitungen haben wir zur Erläuterung entweder das Durchschlagproblem von Abb. 5 oder den Knickstab von Abb. 7 betrachtet. Wir haben uns damit auf die einfachsten Gebilde der Elastostatik, auf „eindimensionale" Stäbe beschränkt, was zunächst zweckmäßig war, um möglichst übersichtliche Beispiele zu erhalten. Praktisch haben wir es aber neben den Stäben vor allem auch mit Platten und Schalen[1], den sog. *Flächenträgern*, zu tun, die für die Rechnung als „zweidimensionale" Gebilde aufgefaßt werden müssen. Bei diesen Flächenträgern können genau so wie bei Stäben Instabilitätserscheinungen auftreten, bei denen wir dann allerdings nicht mehr von einem Knicken, sondern von einem *Beulen* sprechen. Zum Beispiel kann nach

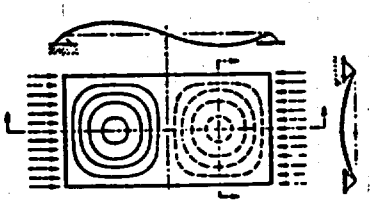

Abb. 42. Ausbeulen einer Rechteckplatte.

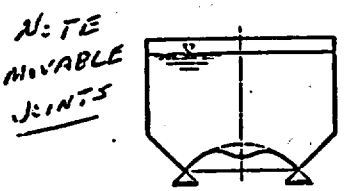

Abb. 43. Beulen eines Intze-Behälters.

Abb. 42 eine durch Druckkräfte beanspruchte Platte in der angedeuteten Art ausbeulen oder nach Abb. 43 der Kugelboden eines Intze-Behälters durch den Flüssigkeitsdruck Beulen bekommen und gegebenenfalls nach unten durchschlagen.

Bei der Berechnung von Flächenträgern gehen wir von der Voraussetzung aus, daß die Platten- bzw. Schalendicke stets klein gegenüber den Abmessungen der

[1] Die Kenntnis der wichtigsten Tatsachen der Platten- und Schalenstatik kleiner Verschiebungen wird im folgenden vorausgesetzt. Es sei z. B. hingewiesen auf S. Timoshenko: Theory of Plates and Shells, New York u. London 1940; W. Flügge: Statik und Dynamik der Schalen, 3. Aufl., Berlin/Göttingen/Heidelberg 1962; W. S. Wlassow: Allgemeine Schalentheorie und ihre Anwendung in der Technik, Berlin 1958; K. Girkmann: Flächentragwerke, 5. Aufl., Wien 1959; A. Pflüger: Elementare Schalenstatik, 3. Aufl., Berlin/Göttingen/Heidelberg 1960.

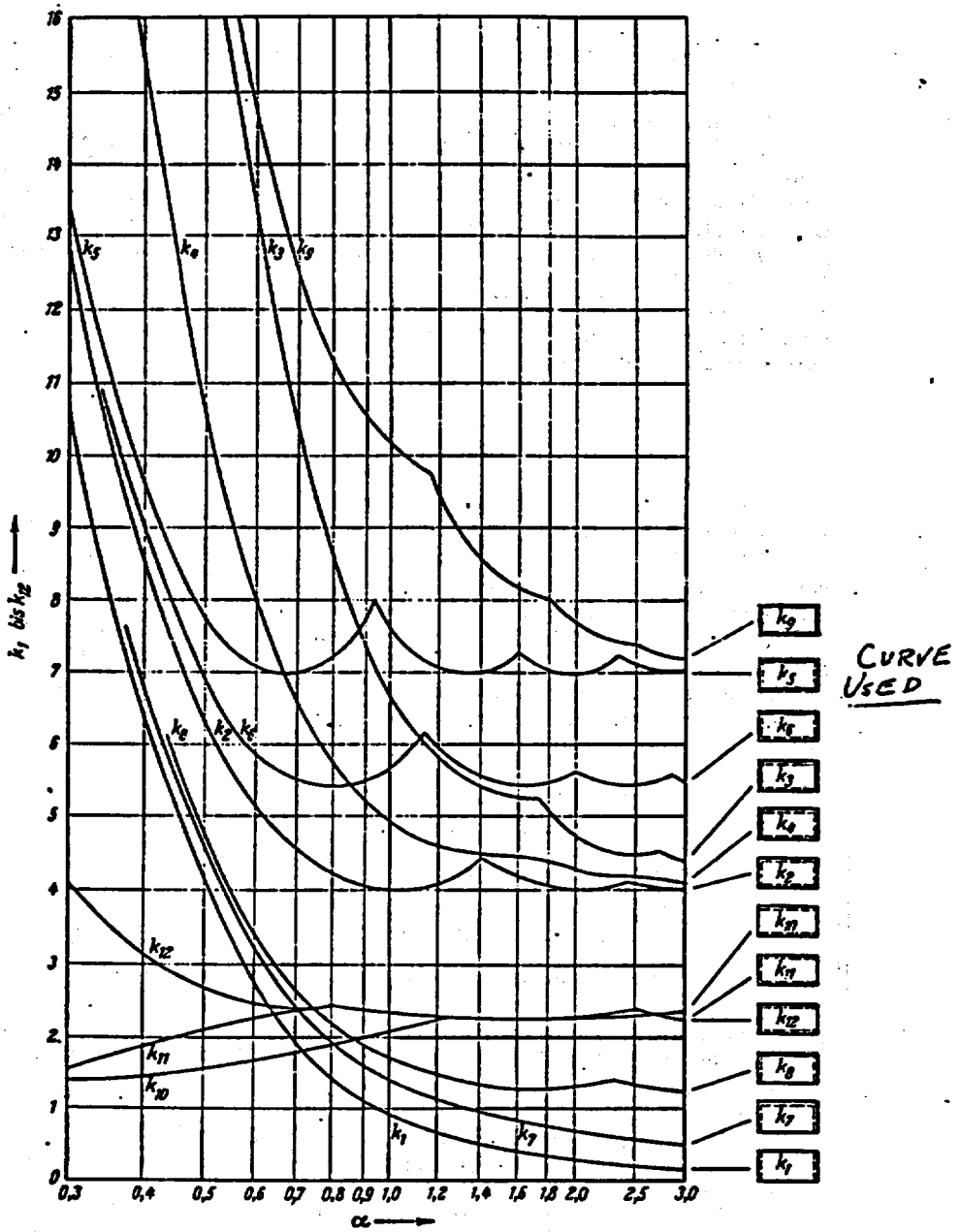

Abb. 36. k_1 bis k_{12}; $\mu = 0{,}3$.

a) Gleichmäßige einachsige Druckbelastung (Fortsetzung)

Nr.	Systemskizzen	Beulformeln	Abkürzungen	Quellen	Bemerkungen
II, A, a, 5		$\beta_1 \operatorname{th}\frac{\beta_1 b}{2} + \beta_2 \tan\frac{\beta_2 b}{2} = 0$ $N_K = k_s N_e$, k_s s. Abb. 36 für $\alpha = \infty$: $k_s = 6{,}97$	$\beta_{1,2} = \sqrt{\frac{\pi}{m\alpha}\left(\frac{\pi}{b}\sqrt{\frac{N_K}{N_e}} \mp \frac{m\pi}{a}\right)}$ $r = \beta_1^2 + \mu\frac{m^2\pi^2}{a^2}$; $s = \beta_1^2 - \mu\frac{m^2\pi^2}{a^2}$; $\alpha = \frac{a}{b}$, $N_e = \frac{\pi^2 E t^3}{12(1-\mu^2)b^2}$ $m = 1, 2, 3, \ldots$ Die das kleinste N_K liefernde Halbwellenzahl m ist maßgeblich.	[II, 70] [II, 27]. S. 161 [II, 35]	Näherung: $\alpha \leqq \frac{2}{3}$: $k_s \approx \frac{1}{\alpha^2} + 5{,}3\alpha^2 + 2{,}37$ $\alpha \geqq \frac{2}{3}$: $k_s \approx 6{,}97$
6		$\beta_2 \tan\beta_2 b - \beta_2 \operatorname{th}\beta_1 b = 0$ $N_K = k_s N_e$, k_s s. Abb. 36 für $\alpha = \infty$: $k_s = 3{,}41$		[II, 27]. S. 165 [II, 70]	
7		$\beta_2\left(\beta_1^2 - \mu\frac{m^2\pi^2}{a^2}\right)^2 \operatorname{th}\beta_1 b -$ $-\beta_1\left(\beta_2^2 + \mu\frac{m^2\pi^2}{a^2}\right)^2 \tan\beta_2 b = 0$ $N_K = k_7 N_e$, k_7 s. Abb. 36 für $\alpha = \infty$; $\mu = 0{,}3$: $k_7 = 0{,}406$		[II, 70] [II, 27]. S. 166 [II, 35]	Näherung: $k_7 \approx \frac{1}{\alpha^2} + 0{,}406$
8		$2rs + (r^2 + s^2)\cos\beta_2 b \operatorname{ch}\beta_1 b -$ $-\frac{1}{\beta_1\beta_2}(\beta_1^2 r^2 - \beta_2^2 s^2)\sin\beta_2 b \operatorname{sh}\beta_1 b = 0$ $N_K = k_8 N_e$, k_8 s. Abb. 36 für $\alpha = \infty$; $\mu = 0{,}3$: $k_8 = 1{,}25$		[II, 27]. S. 170 [II, 35] [II, 70]	Näherung: $\alpha \leqq 1{,}64$: $k_8 \approx \frac{1}{\alpha^2} + 0{,}13\alpha^2 -$ $- 0{,}23 + 1{,}15(1-\mu)$ $\alpha \geqq 1{,}64$: $k_8 \approx 0{,}47$ $+ 1{,}15(1-\mu)$

NATIONAL ADVISORY COMMITTEE FOR AERONAUTICS

TECHNICAL NOTE 3781

HANDBOOK OF STRUCTURAL STABILITY

PART I - BUCKLING OF FLAT PLATES

By George Gerard and Herbert Becker

New York University

Washington
July 1957

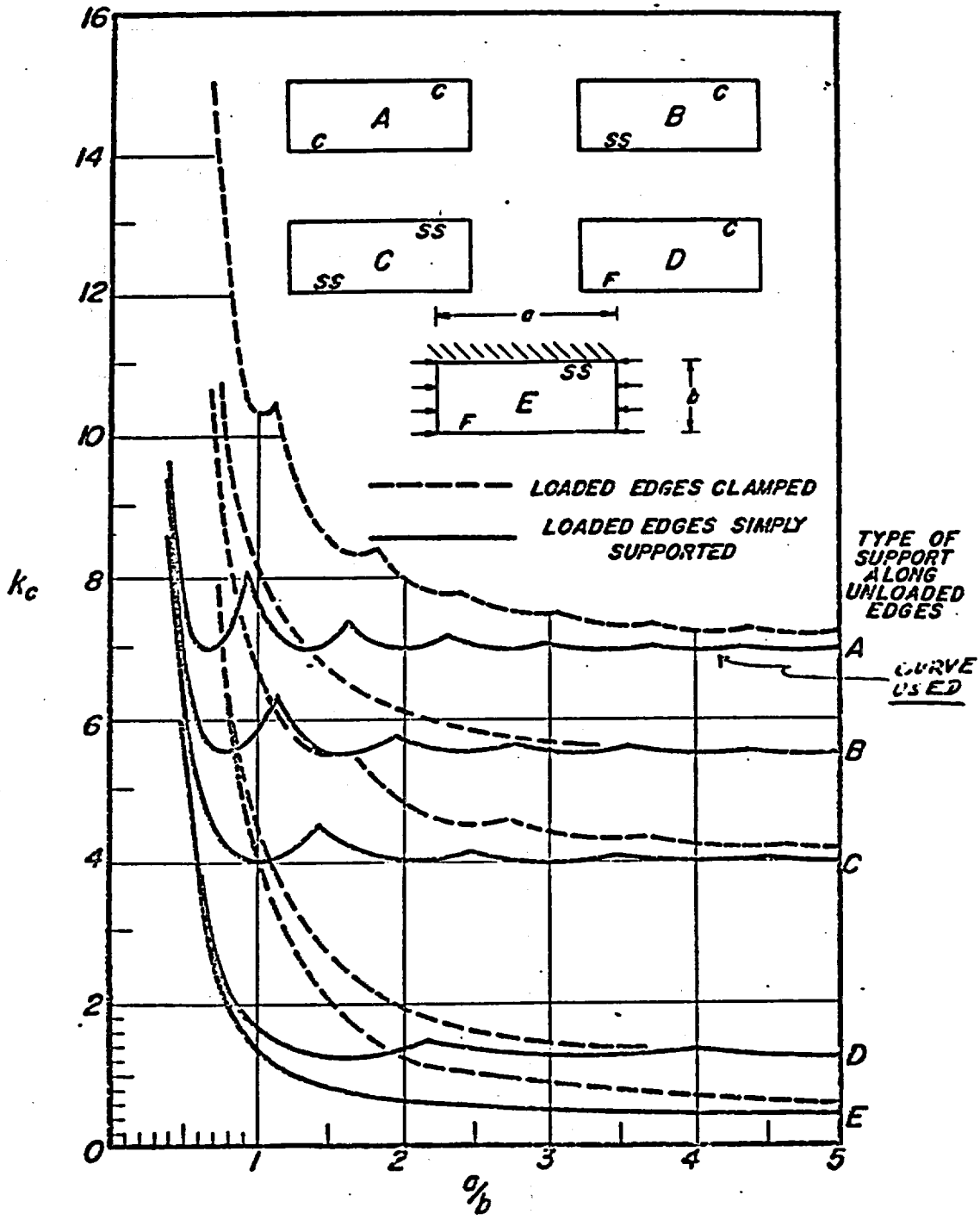

Figure 14.- Compressive-buckling coefficients for flat rectangular plates.

TABLE 7.- BUCKLING COEFFICIENTS FOR INFINITELY LONG PLATES UNDER VARIOUS TYPES OF LOADS

Loading	Edge support	Coefficient	
Compression 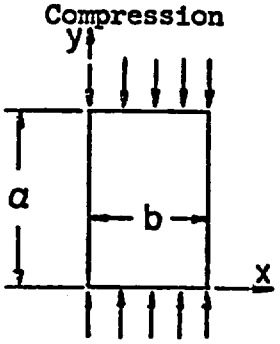	SS on all edges	$k_c = 4.0$	NACA Rep. 733 (ref. 29)
	C on all edges	$k_c = 6.98$	
	SS on y = 0, y = a, x = 0 F on x = b	$k_c = 0.43$	NACA Rep. 734 (ref. 8)
	C on y = 0, y = a, x = 0 F on x = b	$k_c = 1.28$	
Shear 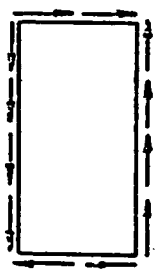	SS on all edges	$k_s = 5.35$	NACA TN 1222 (ref. 35)
	C on all edges	$k_s = 8.98$	NACA TN 1223 (ref. 43)
Bending 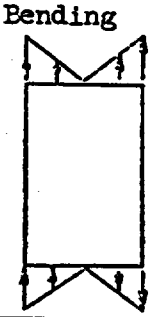	SS on all edges	$k_b = 23.9$	NACA TN 1323 (ref. 37)
	C on all edges	$k_b = 41.8$	

Edge conditions:

C	clamped
F	free
SS	simply supported (hinged)

In sketches accompanying figures, supported edges with elastic rotational restraint are shown shaded. Unshaded loaded edges are simply supported. Unshaded unloaded edges are free.

BASIC PRINCIPLES

General Remarks

The theoretical buckling stress of a flat structural element is the stress at which an exchange of stable equilibrium configurations occurs between the straight and the slightly bent form. It marks the region in which continued application of load results in accelerated growth of deflections perpendicular to the plane of the plate. Its importance lies in the fact that buckling initiates the physical processes which lead to eventual failure of the plate.

The mathematical solution of particular buckling problems requires that equilibrium and boundary conditions be satisfied. This can be accomplished by integration of the equilibrium partial differential equation of the flat plate or by use of mathematical methods which may not completely satisfy the boundary or equilibrium conditions. The former solutions are exact whereas the methods based generally on energy integrals are approximate although usually very accurate. The need for approximate methods arises from the fact that exact solutions can be found for only a limited number of buckling problems of practical importance.

In this section, a brief outline of the methods of analysis of buckling problems is presented. For extensive discussions of the various methods of analysis and their application to a wide variety of problems, reference to the books of Timoshenko, Sokolnikoff, and Bleich (refs. 2 to 4) is suggested.

Equilibrium Differential Equation

The general form of the differential equation describing the slightly bent equilibrium configuration of an initially flat plate was derived by Stowell in the following form (ref. 5):

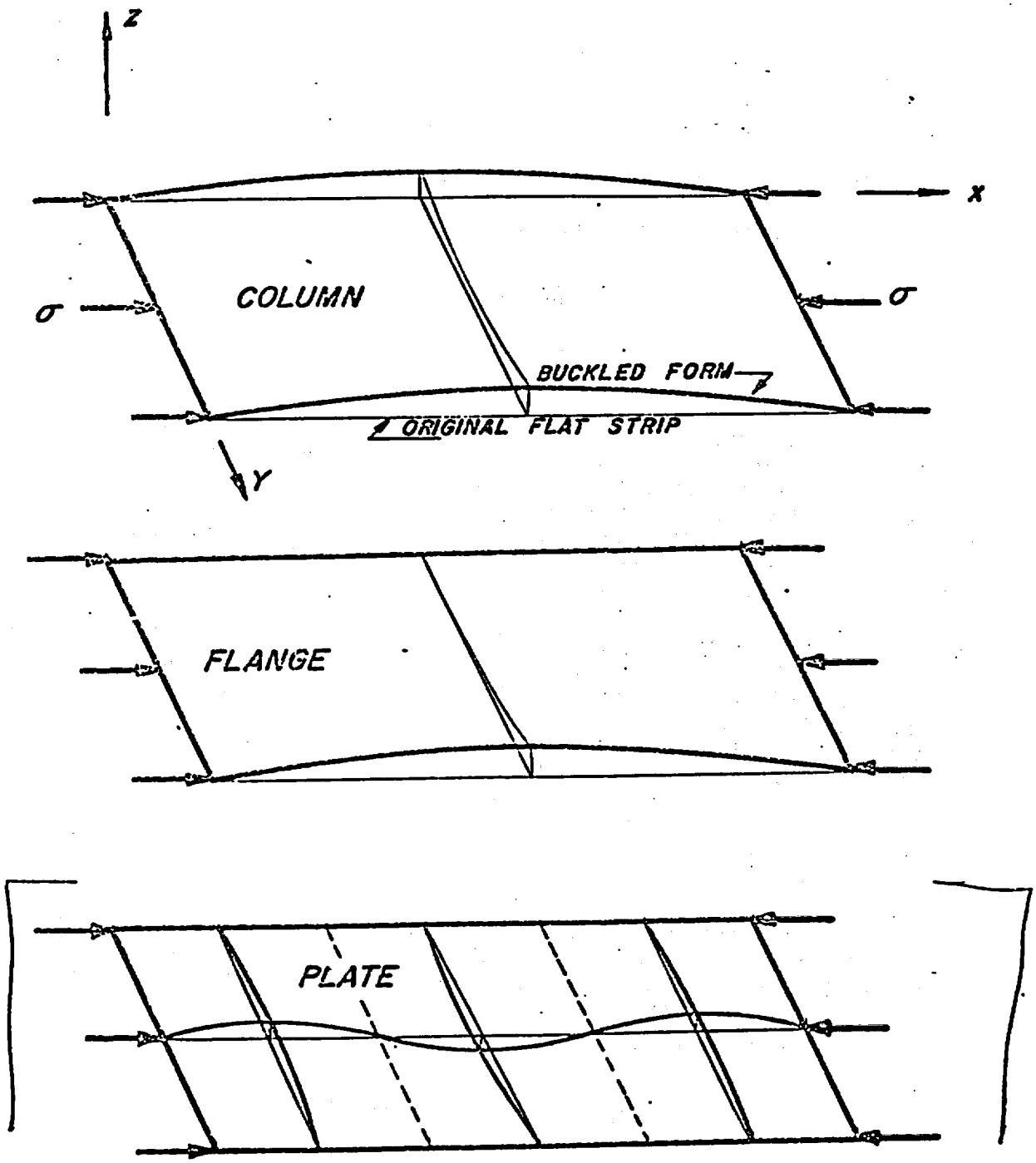

Figure 1.- Transition from column to plate as supports are added along unloaded edges. Note changes in buckle configurations.

This method and its application to specific problems is described by Budiansky and Hu (ref. 6). They have treated the Lagrangian multiplier method in a manner in which it is possible to obtain approximate solutions for both upper and lower bounds. As determinants of higher order are used to obtain better approximations, both the upper and lower bounds approach the true buckling stress. Thus, the Lagrangian multiplier method may be used to obtain results within any desired degree of accuracy.

In addition to the above procedures which are based on energy integrals, other methods of obtaining approximate solutions of buckling problems have been used which involve the equilibrium differential equation. Functions which satisfy the geometrical boundary conditions exactly are used to satisfy the governing differential equation approximately by processes that lead to integration of these functions. Galerkin's method, finite-difference equations, relaxation techniques, and iteration are some of the numerical methods that can be used.

BOUNDARY CONDITIONS

The nature of the buckle pattern in a plate depends not only upon the type of applied loading but also upon the manner in which the edges are supported. This is illustrated in figure 1 in which the same axial compressive loading is seen to generate three types of buckle patterns on a long rectangular plate with different geometrical boundary conditions. The single wave is representative of column behavior, the twisted wave is representative of flange behavior, and the multiple-buckle pattern is representative of plate behavior.

To indicate the manner in which the geometric boundary conditions mathematically influence the buckling behavior and also to demonstrate the solution of the equilibrium differential equation (eq. (4)) for some particular cases, the plates shown in figure 1 are analyzed. Boundary conditions which characterize simply supported wide columns, flanges, and plates are considered.

Mathematical Analysis

The equilibrium differential equation for elastic buckling of a uniaxially compressed plate can be obtained from equation (4) in the form

$$\frac{\partial^4 w}{\partial x^4} + 2\frac{\partial^4 w}{\partial x^2 \partial y^2} + \frac{\partial^4 w}{\partial y^4} + \frac{\sigma t}{D}\frac{\partial^2 w}{\partial x^2} = 0 \qquad (7)$$

It is assumed that the loaded edges of the plate are simply supported and therefore an appropriate solution of equation (7) is

$$w = \left(c_1 \cosh \frac{\bar{\alpha}y}{b} + c_2 \sinh \frac{\bar{\alpha}y}{b} + c_3 \cos \frac{\bar{\beta}y}{b} + c_4 \sin \frac{\bar{\beta}y}{b}\right)\cos \frac{\pi x}{\lambda} \tag{8}$$

where

$$\bar{\alpha} = \pi\left(\frac{b}{\lambda}\right)^{1/2}\left[\frac{b}{\lambda} + \left(k_c\right)^{1/2}\right]^{1/2} \tag{9}$$

$$\bar{\beta} = \pi\left(\frac{b}{\lambda}\right)^{1/2}\left[-\frac{b}{\lambda} + \left(k_c\right)^{1/2}\right]^{1/2} \tag{10}$$

$$k_c = \frac{12\left(1 - \nu_e^2\right)\sigma_{cr}}{\pi^2 E}\left(\frac{b}{t}\right)^2 \tag{11}$$

The coefficients c_1 to c_4 are to be determined by the geometrical boundary conditions along the unloaded edges of the plate.

For the wide column, the unloaded edges located at $y = \pm b/2$ are free, and consequently the edge moments and reduced shears must be zero. Therefore,

$$\left(\frac{\partial^2 w}{\partial y^2} + \nu_e \frac{\partial^2 w}{\partial x^2}\right)_{y=\pm b/2} = 0$$

$$\left[\frac{\partial^3 w}{\partial y^3} + 2\left(1 - \nu_e\right)\frac{\partial^3 w}{\partial x^2 \partial y}\right]_{y=\pm b/2} = 0 \tag{12}$$

For the flange, the unloaded edge at $y = 0$ is assumed to be simply supported and that at $y = b$ is free:

$$\left.\begin{aligned} (w)_{y=0} &= 0 \\ \left(\frac{\partial^2 w}{\partial y^2} + \nu_e \frac{\partial^2 w}{\partial x^2}\right)_{y=0,b} &= 0 \\ \left[\frac{\partial^3 w}{\partial y^3} + 2\left(1 - \nu_e\right)\frac{\partial^3 w}{\partial x^2 \partial y}\right]_{y=b} &= 0 \end{aligned}\right\} \tag{13}$$

The plate is assumed to be simply supported along the unloaded edges located at $y = \pm b/2$:

$$\left.\begin{aligned} (w)_{y=\pm b/2} &= 0 \\ \left(\frac{\partial^2 w}{\partial y^2} + \nu_e \frac{\partial^2 w}{\partial x^2}\right)_{y=\pm b/2} &= 0 \end{aligned}\right\} \tag{14}$$

Incorporation of these boundary conditions into the solution given by equation (8) leads to the following implicit expressions for k_c.

For the column,

$$\bar{p}^2\bar{\beta} \tan(\bar{\beta}/2) + \bar{q}^2\bar{\alpha} \tanh(\bar{\alpha}/2) = 0 \tag{15}$$

for the flange,

$$\bar{p}^2\bar{\beta} \sinh \bar{\alpha} \cos \bar{\beta} - \bar{q}^2\bar{\alpha} \cosh \bar{\alpha} \sin \bar{\beta} = 0 \tag{16}$$

and for the plate

$$\left[\bar{\alpha} \tanh(\bar{\alpha}/2) + \bar{\beta} \tan(\bar{\beta}/2)\right]^{-1} = 0 \tag{17}$$

where

$$\bar{p} = \bar{\alpha}^2 - \nu_e(\pi b/\lambda)^2$$

and

$$\bar{q} = \bar{\beta}^2 + \nu_e(\pi b/\lambda)^2$$

The buckling coefficient for wide columns and flanges is shown as a function of ν_e and a/b in figure 2. The solutions for wide columns were given by Houbolt and Stowell by use of the differential equation for simply supported loaded edges and the energy method for clamped loaded edges (ref. 7).

The buckling coefficient for a simply supported flange was derived by Lundquist and Stowell (ref. 8) in the form

$$k_c = (6/\pi^2)\left\{(1 - \nu_e) + \left[(\pi b/\lambda)^2/6\right]\right\} \quad (18)$$

When the unloaded edge is clamped,

$$k_c = 0.83 - 0.93\nu_e + 1.34(\lambda/\pi b)^2 + 0.10(\pi b/\lambda)^2 \quad (19)$$

For the simply supported plate

$$k_c = \left[(\lambda/b) + (b/\lambda)\right]^2 \quad (20)$$

Anticlastic Curvature

As may be seen from the solutions in the preceding section, the buckling coefficient for the simply supported plate depends upon only b/λ and is independent of Poisson's ratio, while the coefficients for the wide column and flange are functions of both ν_e and b/λ. This situation is not limited to the case of simple support alone but pertains to any degree of rotational restraint along the unloaded edges of a plate. The influence of ν_e upon k_c is traceable to the reduced-shear terms at the free edges of flanges and columns. Boundary conditions such as simple support do not impose the requirement of zero reduced shear along the unloaded edges, which eliminates the ν_e influence from the relationship for k_c.

The value of the compressive buckling coefficient for an element containing a free unloaded edge depends upon the degree of anticlastic curvature developed. For a very narrow element such as a beam, complete

THIS PAGE INTENTIONALLY LEFT BLANK

APPENDIX B

EVALUATION FOR LEAD PRESSURE

B.1 INTRODUCTION

The purpose of the analysis described in this section was to provide a better understanding of the interaction of the lead with the shells of the cask during the cool-down from the lead casting procedure and during the normal operational cycling. Additionally, the analysis was to determine an approximate temperature level at which the lead pressure fell to zero.

A special purpose finite element program was used to investigate the lead behavior. To keep the finite element model simple, some approximations were necessary; however, the important mechanical features of the structural system such as elastic-plastic-creep response of the lead, elastic-plastic response of the stainless steel shells, and the possibility for axial movement of the lead were included.

The model was cycled through temperature histograms which covered a spectrum of typical cask operating histories for the normal condition.

B.2 SUMMARY AND CONCLUSIONS

Significant results of the lead pressure evaluation were:

a. During cool-down from the casting stage, the large thermal contraction of the lead relative to the shells produces significant tensile stresses in the lead. The stresses are sufficient to cause yielding in the inner shell.

b. Because of the low strain hardening assumed for the stainless steel, the final resulting stress state of the lead after casting was essentially independent of the temperature point at which

it was assumed the lead began to gain strength following its solidification in the casting process.

c. In the short axial length of the shells analyzed, it was found that there was little axial movement of the lead even for long hold periods at room and elevated temperatures. The implication of this observation is that the pressures developed in the lead do not relax with time. This conclusion will hold also for the longer shells of the cask.

d. The analysis indicates that a stable lead pressure cycle is established on the first cycle after the cool from melt.

e. A zero-lead-pressure temperature of 360°F was established. This temperature is unique to the system of shells of the cask since it is dependent on the yielding of the inner shell. Further, at the zero-lead-pressure temperature, the residual stresses in the shells, both axial and hoop, were also approximately zero.

B.3 ANALYSIS

The computer program used to develop the lead history solutions was an ORNL research program called PLACRE (Ref. 62). This program was written specifically to solve elastic-plastic-creep problems for simple plane and axisymmetric structures. For this particular problem, the PLACRE program is much more efficient than the large general-purpose programs.

Solving a problem involving creep of lead by the technique used in most of the available finite element codes (including PLACRE) is a difficult task. This technique, the initial strain approach, requires that the creep strain increment during a given solution step be fairly small in relation to the

elastic strains. For lead, which can creep large amounts at relatively small stresses, programs utilizing the initial strain approach require that very small time steps be taken to insure stability of the numerical procedure. For the small model used, PLACRE could develop the required number of solutions efficiently. Additionally, PLACRE contained a number of controls that automatically selected the time step to insure a stable and accurate solution.

A sketch of the structure modeled is shown in Fig. B.3-1. As seen from the sketch, the axisymmetric model included the lead and the inner and outer shells. The axial length was taken as 24 inches. The axial dimension was controlled by three factors: (1) The model should be long enough to be independent of shell boundary affects. Therefore, the axial length was taken at least $2.5\sqrt{Rt}$ for the outer shell. (2) If there is significant axial movement of the lead, the longer the model, the better will be the simulation of the real lead stresses developed in the cask. (3) The size of the model in terms of nodes and elements must be small enough to allow a computer solution reasonable in costs. The length selected is a compromise between the second and third factors.

In Fig. B.3-2, the nodal and element structure of the PLACRE model is shown. The inner two triangular ring elements make up the inner shell, the next eight triangular elements simulate the lead, and the outer elements model the outer shell. A perfect bond between the lead and stainless steel was considered.

Boundary conditions on the model consisted of radial rollers on the $z=0$ face (including both the lead and stainless steel). This condition simulates a long cylinder. The other end of the model was left free. The free-end condition was necessary since it was not feasible to model an end

forging and keep the model within the nodal and element size limitations. For these same reasons, the water jacket was not included in the PLACRE model.

The loading conditions on the model consisted of isothermal temperature cycling. No pressure cycling was considered. Schematics of the temperature load histories are given in Fig. B.3-3. The cooling rates, heating rates, and hold times were selected to simulate the cask temperatures from melt and the temperature history for the normal 14 day, loading-unloading cycle. In Load History A of Fig. B.3-3, a starting temperature of 500° F was used as the temperature at which the stresses begin to develop in the cooling lead from melt. Load History A consists of one complete load-unload-return cycle. Load History B of Fig. B.3-3 simulated only the cool from melt, assuming the stresses began at 400° F. This later history was included to assess the affect of the starting temperature assumption.

The material properties for the stainless steel were taken from the curves of Section XI of this SAR, as were the properties for the lead. The lead stress-strain curves and their bilinear approximation are given in Section B.5 of this appendix. In addition to these properties, lead creep properties were required. The creep curves of Ref. 20 were translated into an empirical expression which was acceptable to PLACRE. In the conversion to the empirical expression, only the steady-state (minimum) creep rate was considered, the primary creep being assumed small in relation to the total amount of creep. The determination of the parameters of the empirical expression is also given in Section B.5 of this appendix.

B.4 RESULTS

The results for the simulated initial cool from casting for the two load

histories are shown in Figs. B.4-1 & 2. In these figures, the radial stress in the lead at the inner and outer shells, respectively, is shown as a function of temperature.

In the initial cool-down, the results show the contracting lead producing tension fields at both the inner and outer shells. In this cool-down, the stainless steel shells are also contracting, but not at as rapid a rate as the lead. This is due to the larger coefficient of thermal expansion of the lead. The curves of Figs. B.4-1 & 2 show a linear relation between the lead tension and temperature until the tension reaches the point where it can yield the inner shell at the particular temperature in the cool-down (the temperature-dependent yield of stainless steel was modeled). After the inner shell yields, the lead tension increases with decreasing temperature as a function of the yield vs. temperature properties of the inner stainless steel shell.

This dependence on the yield vs. temperature response of the lead temperature is demonstrated by the similarity of the lead tension results for the two load cases after the inner shell has yielded. It follows that if the inner shell yields in the cool from melt, the final room-temperature lead tension will be independent of the starting temperature. This statement will not hold if the stainless steel is modeled with a steep or multilinear stress vs. plastic strain slope. But for the case as analyzed, i.e., with the strain hardening of the stainless steel relatively flat, the room-temperature lead tension is independent of the starting temperature.

An interesting parameter useful in the cask evaluation is available from the curves of Fig. B.4-1 and the PLACRE print-out. In particular, the results for the initial cool-down can provide a rough approximation of

the relation between the lead pressure change and the plastic strain in the inner shell. To determine the relation, the slope is determined for the temperature vs. pressure response while the inner shell is elastic. The 70°F intercept, assuming elastic inner shell response, is then computed. It follows then that the pressure reduction caused by the yielding of the inner shell would be simply the difference between the elastic line 70°F intercept and the actual calculated pressure at 70°F. If the pressure change and the plastic strain are assumed to be linearly related, the computed slope of the pressure change vs. plastic strain is $7.8(10)^5$ psi/in./in. This result indicates the very small amount of plastic strain involved in the shell with a substantial change of lead pressure.

Following the initial cool-down, for both the load histories, a 1,000 hour hold period was simulated. During this hold, the stress in the lead did not relax, but only redistributed itself slightly as indicated in Fig. B.4-2.

In the re-heat to 400°F for Load History A, the lead stress response is seen again to be linear, with approximately the same slope as observed in the initial cool-down. The indicated stress-free temperature is 360°F. At the final 400°F temperature, the lead is exerting a pressure on the shells. This pressure results from the change in volume of the lead cavity with the outward (tensile) yielding of the inner shell. The heat-up time of 96 hours represents the estimated time for the fuel to heat the cask.

The upper temperature level was held for the remaining 10 days of the anticipated 14 day, average travel time. Again, the stress levels did not relax and there was little indicated axial movement of the lead.

One additional initial cool-down case was completed. This case was made to assess the influence of lead creep on the results of the PLACRE calculations. This is an important question since the computer model of

the entire cask considers only the plastic properties of the lead. For this case, the loading consisted of a temperature step from 400°F to 70°F, with the creep calculations of PLACRE suppressed.

The results, shown in Figs. B.4-1 & 2, indicate that approximately the same path is followed with or without creep. Examination of the computer results indicates that the total inelastic strains for the creep and no-creep cases are essentially the same, thus demonstrating that the low yield stress of the lead allows the plastic flow in the absence of creep.

The no-creep solution, moreover, indicates that the rates of cool-down, and probably heat-up, are not important factors of computations.

Continuing the Load History A, the PLACRE model was cycled to room temperature in 8 hours to simulate the cool-down in the unloading process. With this cool-down, the first cycle was complete. The temperature vs. radial lead pressure results for the cool-down are given in Figs. B.4-3 & 4. The curves of these figures indicate that a stable cycle has been established. At the inner shell, the cooling path (temperature vs. pressure) is very close to the heating results. At the outer shell, the pressure during the cool-down is larger than during the heat-up, but after a 14 day hold at room temperature, the pressure at the outer shell falls to essentially the level at the end of the 1,000 hour hold period of Load History A. It is anticipated that repeated cycles would simply follow the pressure history established in the last heat-up and cool-down of Load History A.

It is also of interest to examine the residual stresses in the stainless steel shells during the different phases of the temperature cycling. These stress responses for the loading cycles are given in Figs. B.4-5 through 7.

The important result indicated in Figs. B.4-5 & 6 is that the stresses in the shells are also approximately zero at the zero-lead-pressure tempera-

ture of 360°F. Thus, the PLACRE results indicate, neglecting the water jacket shell, that the lead and stainless steel system is approximately stress-free at 360°F.

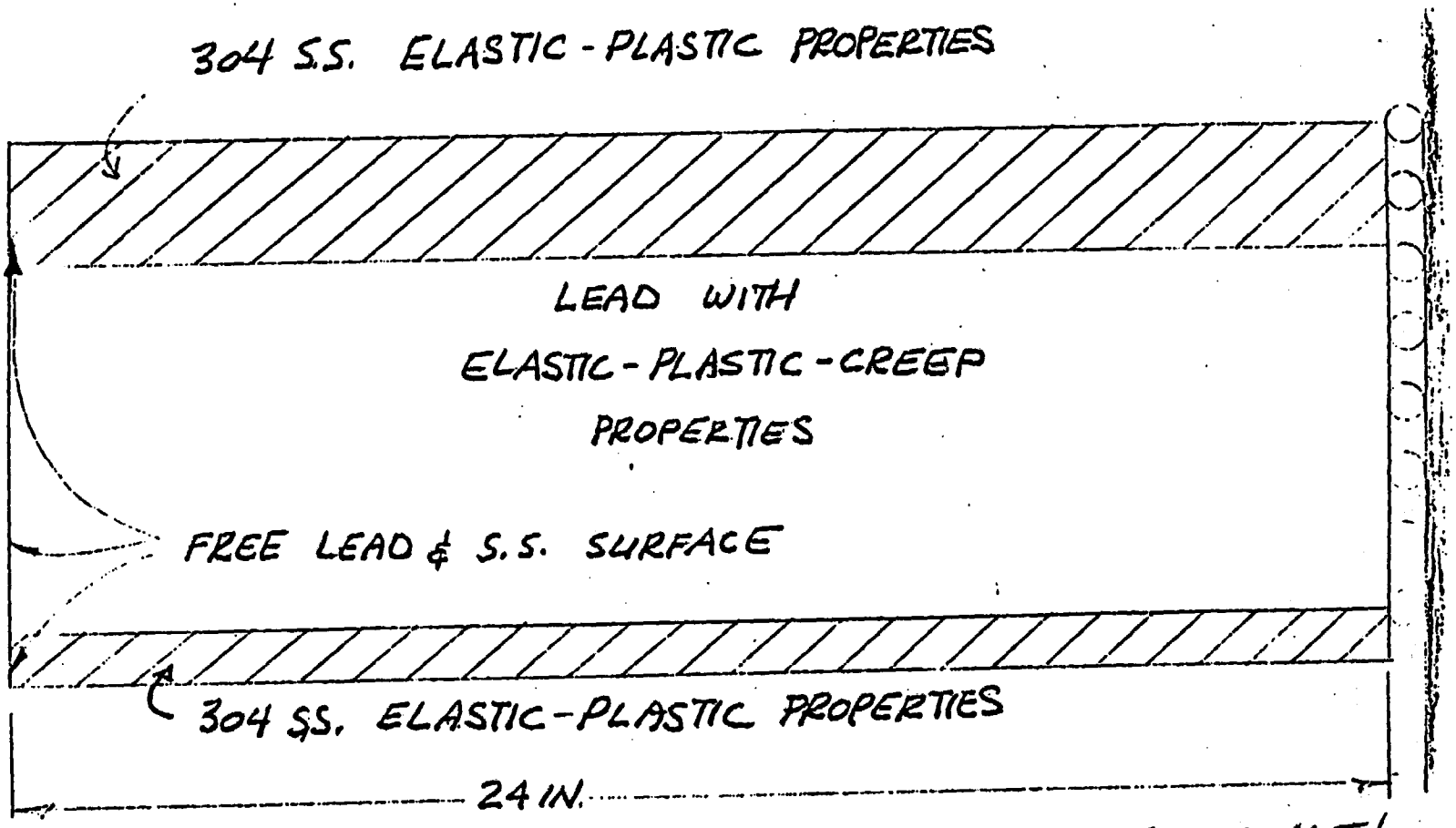

LEAD PRESSURE EVALUATION MODEL

ORNL PLACRE COMPUTER PROGRAM

PLACRE LEAD PRESSURE MODEL

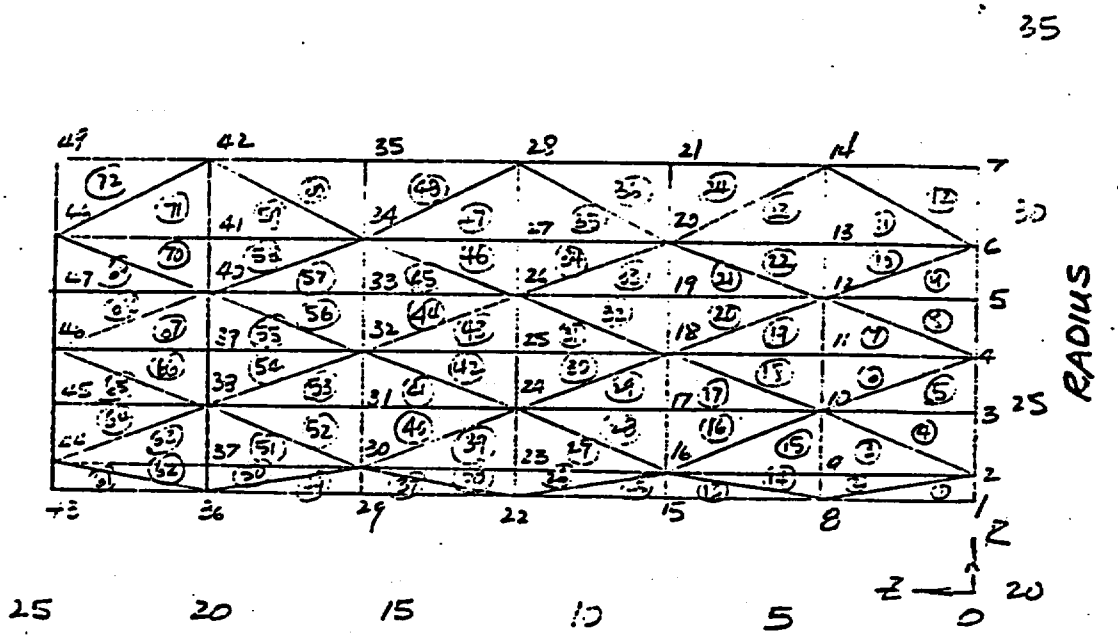

LEAD PRESSURE EVALUATION
IMPOSED TEMPERATURE HISTOGRAMS

LOAD HISTORY A!

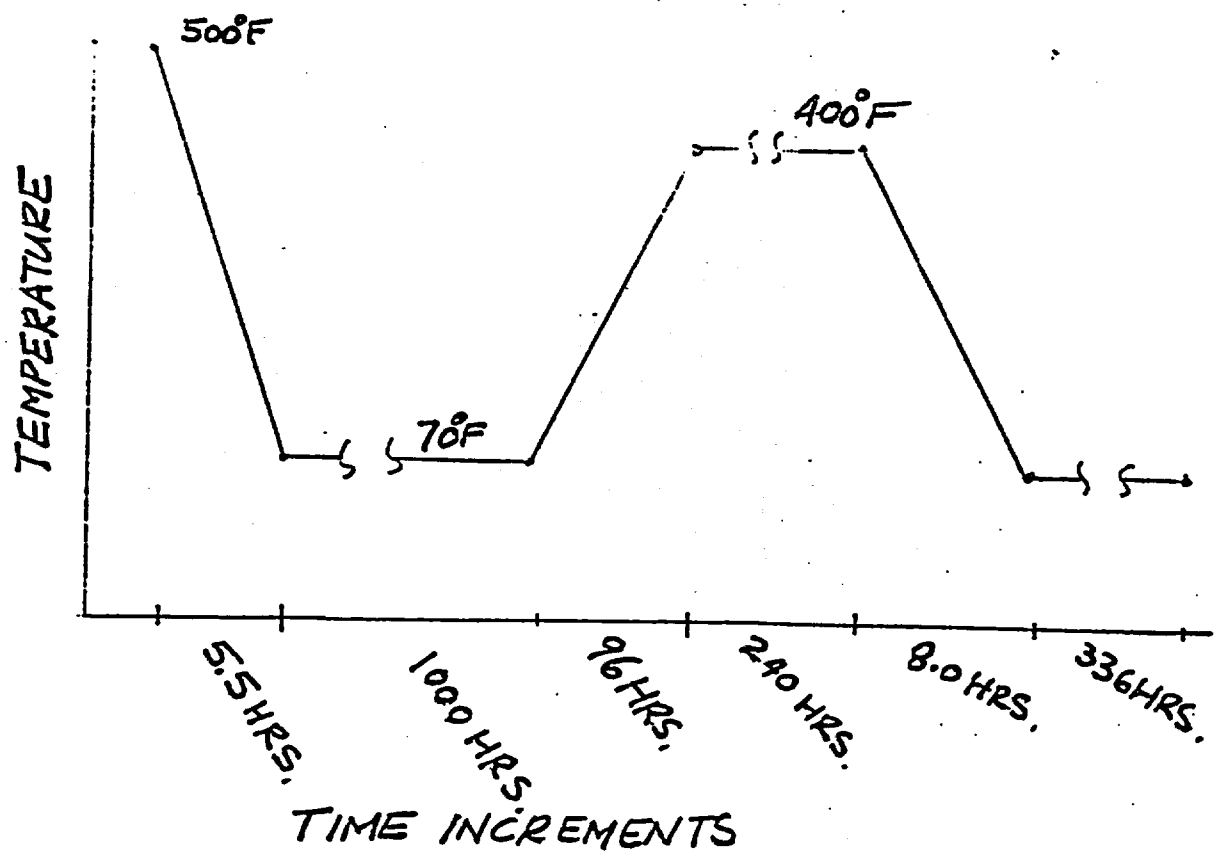

LOAD HISTORY B!

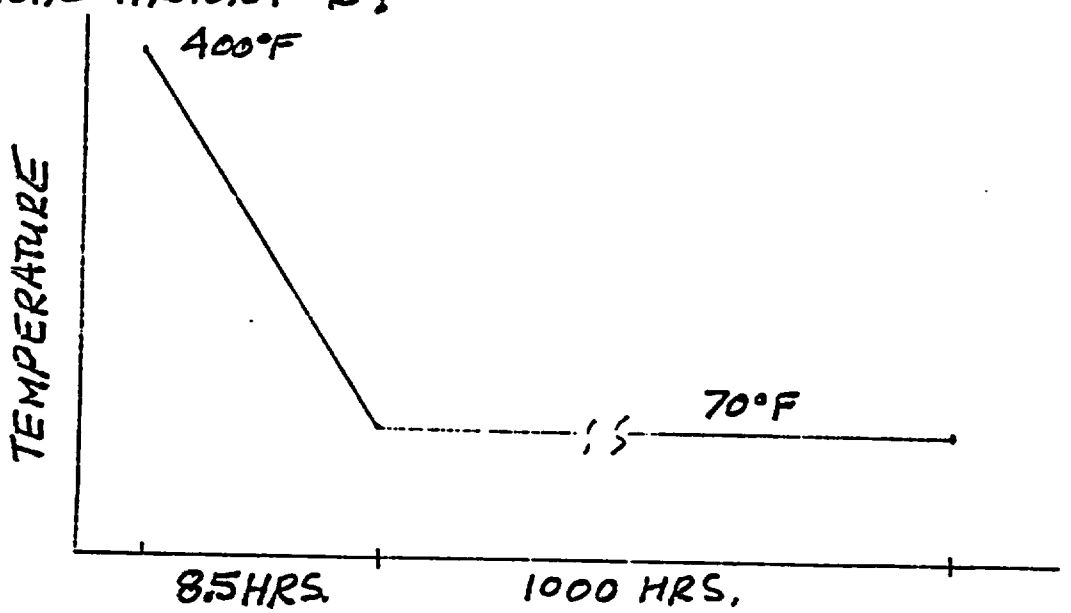

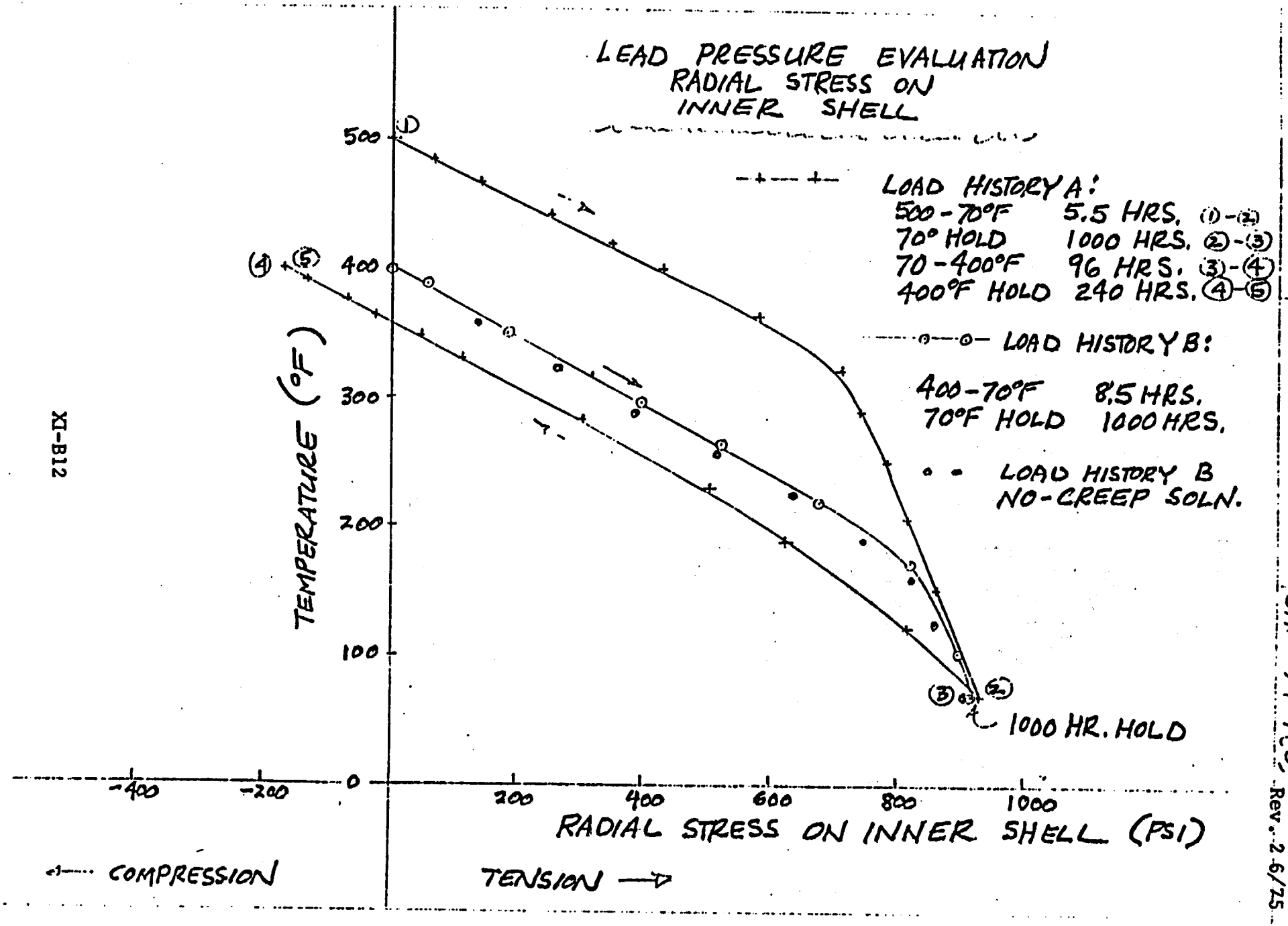

XI-B12

6/12/75 Rev. 2 6/25/75 THI-74-1(6)

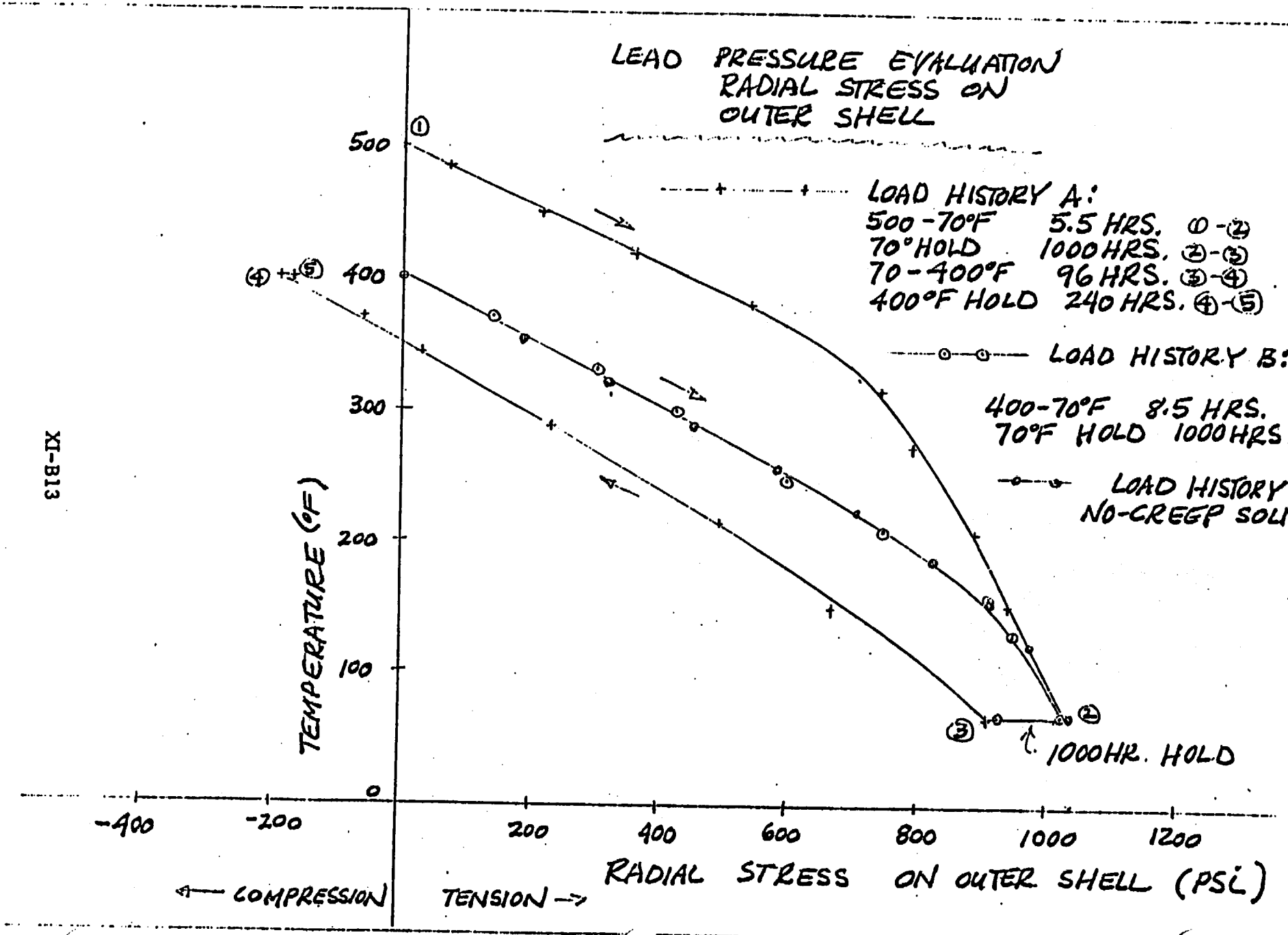

XI-B13

FIG. 5.4-2

JPH-24-1(B) Rev. 2 6/75

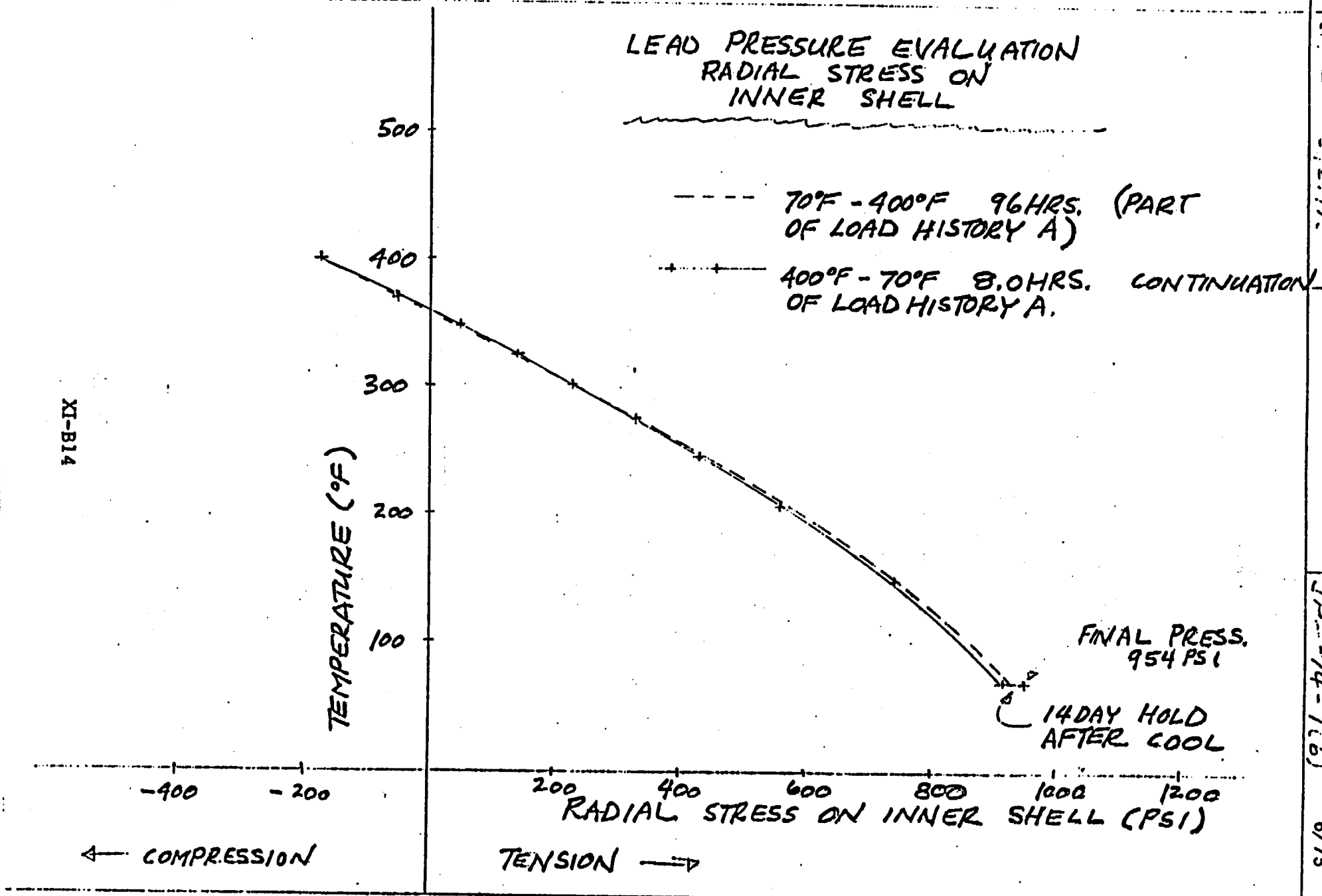

XI-B14

TR-74-1(01) 6/75

FIG. B4 - 5

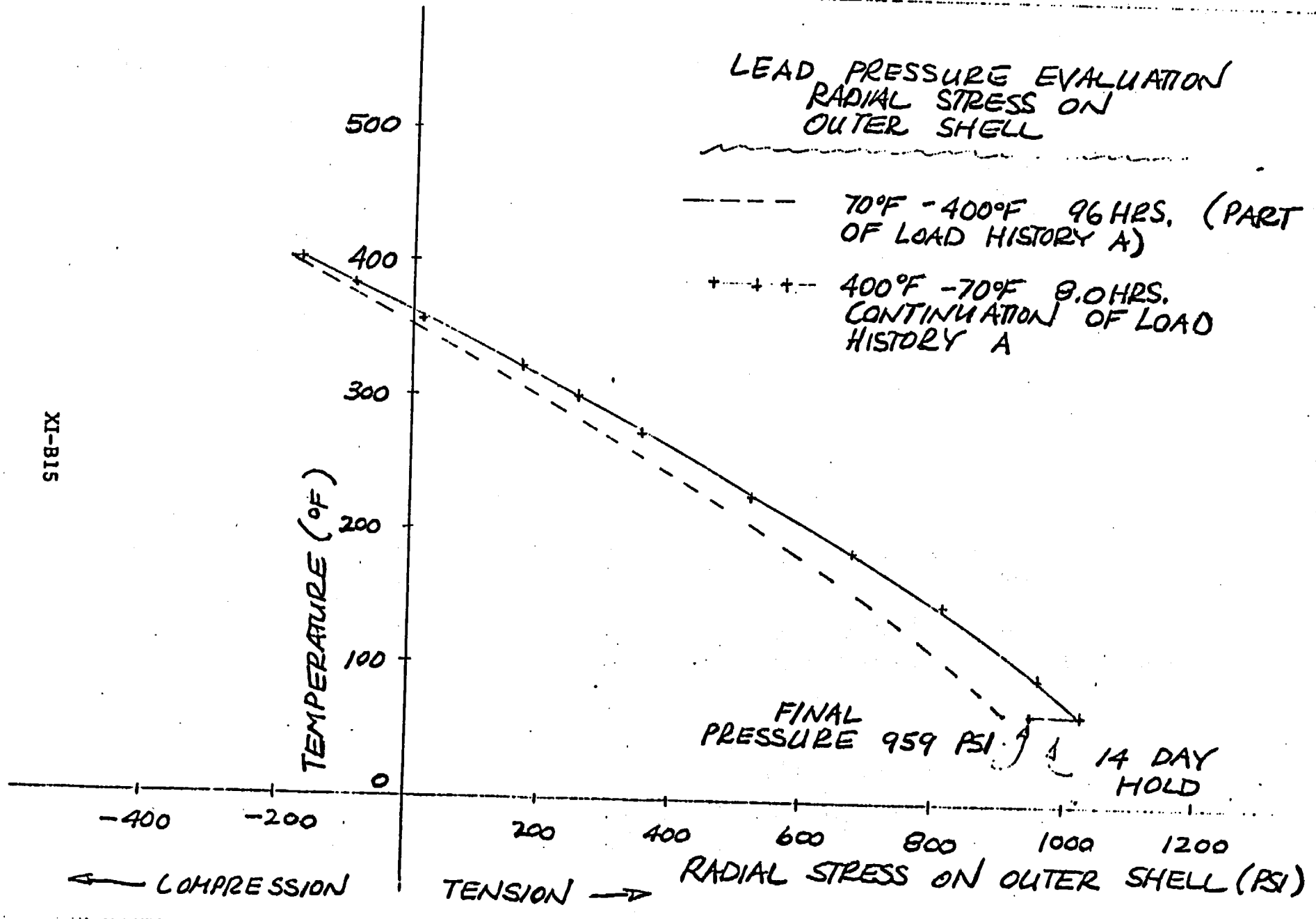

XI-B15

JH--74-1(G) 6/75

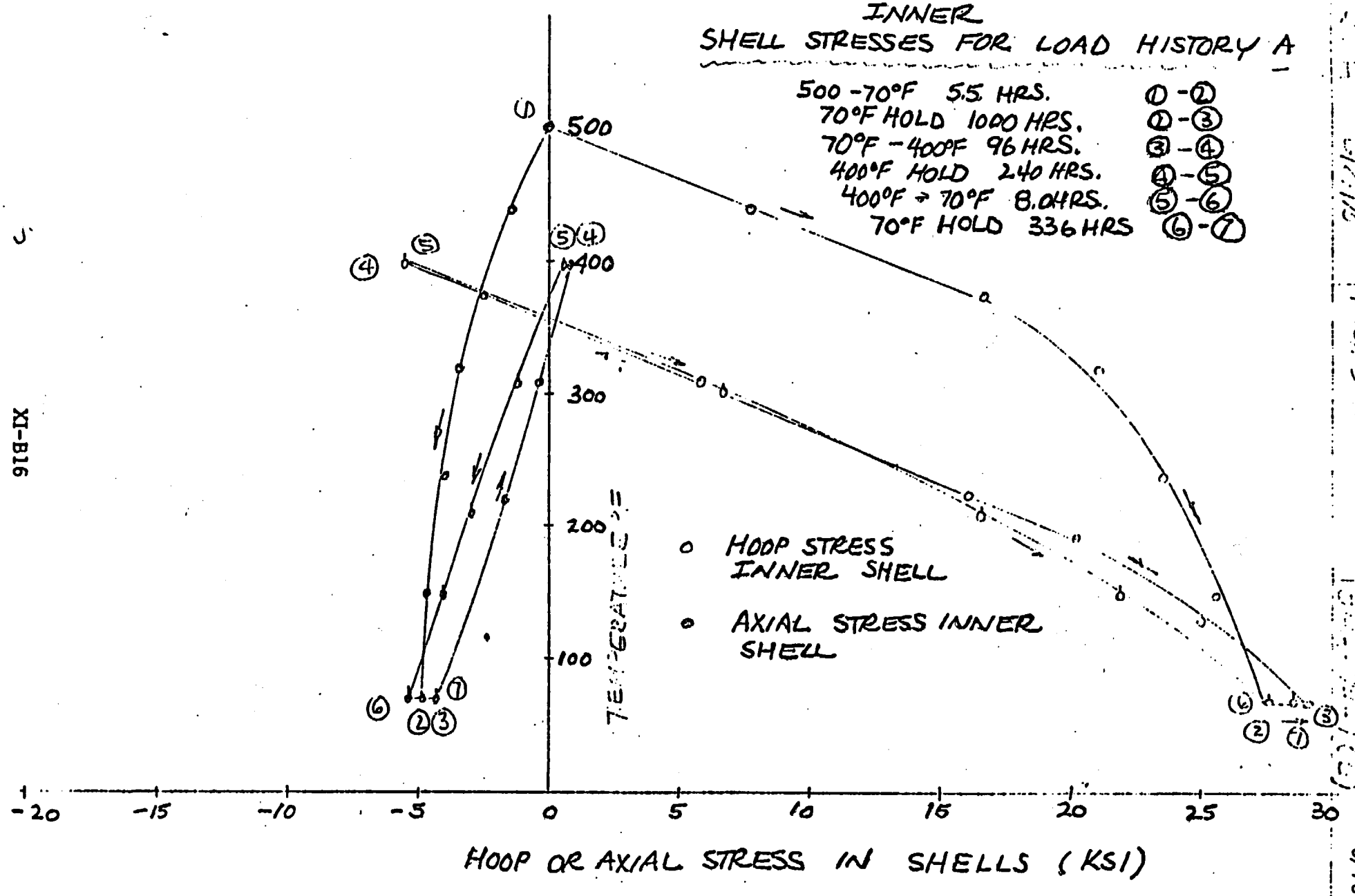
INNER
SHELL STRESSES FOR LOAD HISTORY A
500 -70°F 5.5 HRS. ① -②
70°F HOLD 1000 HRS. ① -③
70°F -400°F 96 HRS. ③ -④
400°F HOLD 240 HRS. ④ -⑤
400°F → 70°F 8.0 HRS. ⑤ -⑥
70°F HOLD 336 HRS ⑥ -①
500
400
300
200
100
TEMPERATURE °F
HOOP STRESS INNER SHELL
AXIAL STRESS INNER SHELL
-20
-15
-10
-5
0
5
10
15
20
25
30
HOOP OR AXIAL STRESS IN SHELLS (KSI)

XI-816

6/75

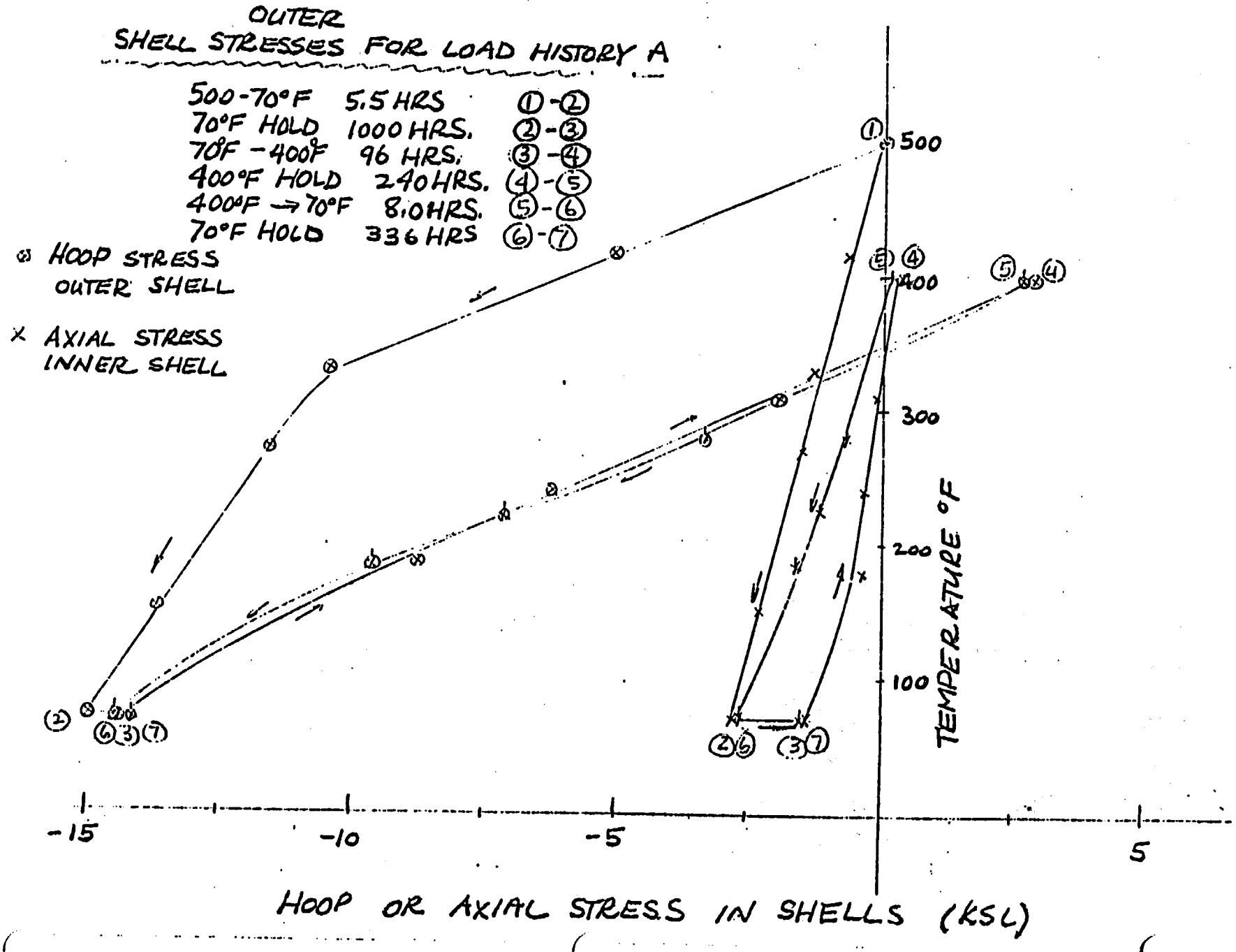
OUTER
SHELL STRESSES FOR LOAD HISTORY A
500-70°F 5.5 HRS ①-②
70°F HOLD 1000 HRS. ②-③
70°F-400°F 96 HRS. ③-④
400°F HOLD 240 HRS. ④-⑤
400°F → 70°F 8.0 HRS. ⑤-⑥
70°F HOLD 336 HRS ⑥-⑦
⊗ HOOP STRESS OUTER SHELL
× AXIAL STRESS INNER SHELL
500
400
300
200
100
TEMPERATURE °F
-15
-10
-5
5
HOOP OR AXIAL STRESS IN SHELLS (KSL)

XI-B17

6/75

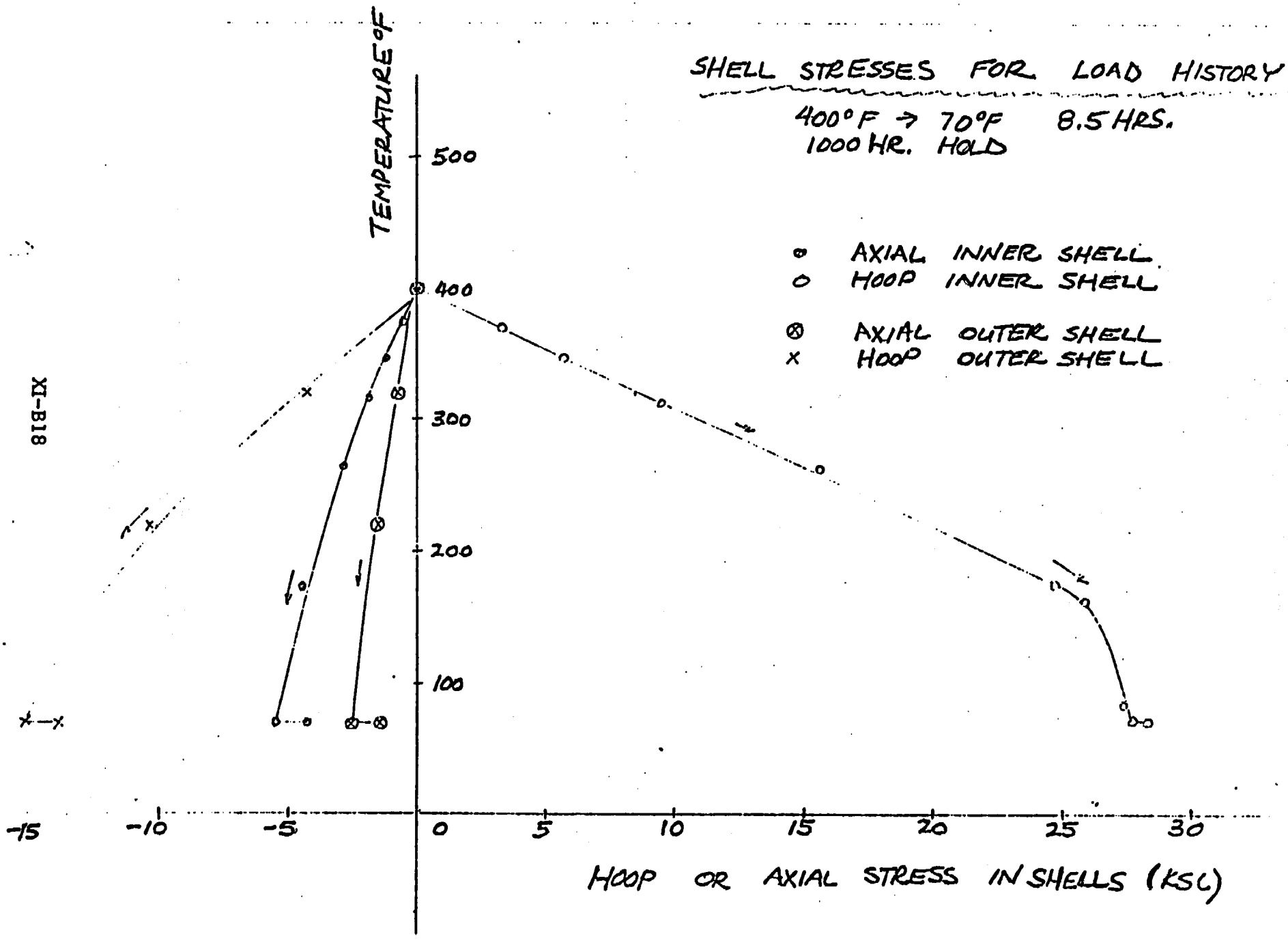

XI-818

FIG. 4.4.4-7

CHI-74-1(3)

6/75

STRESS STRAIN CURVES FOR LEAD

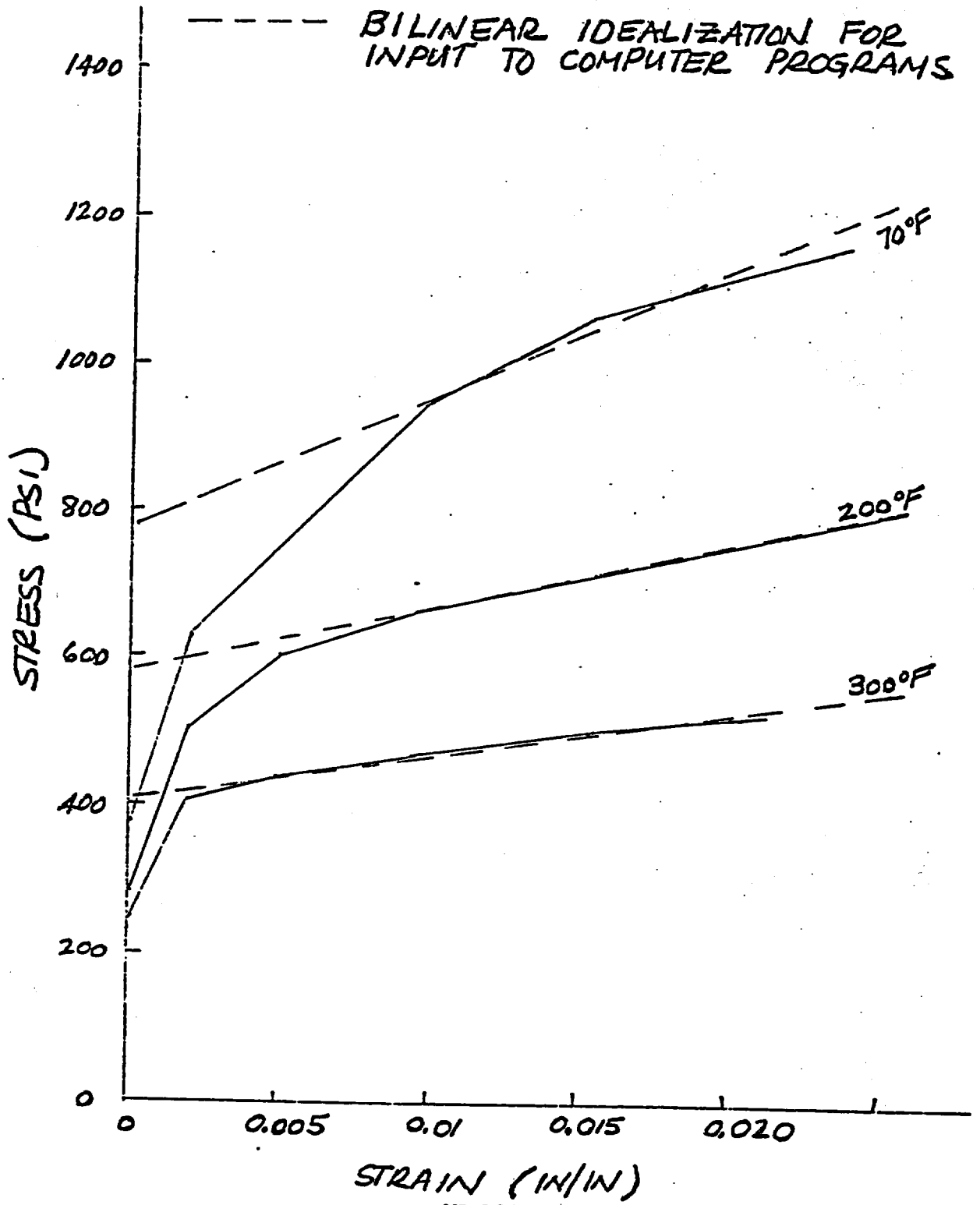

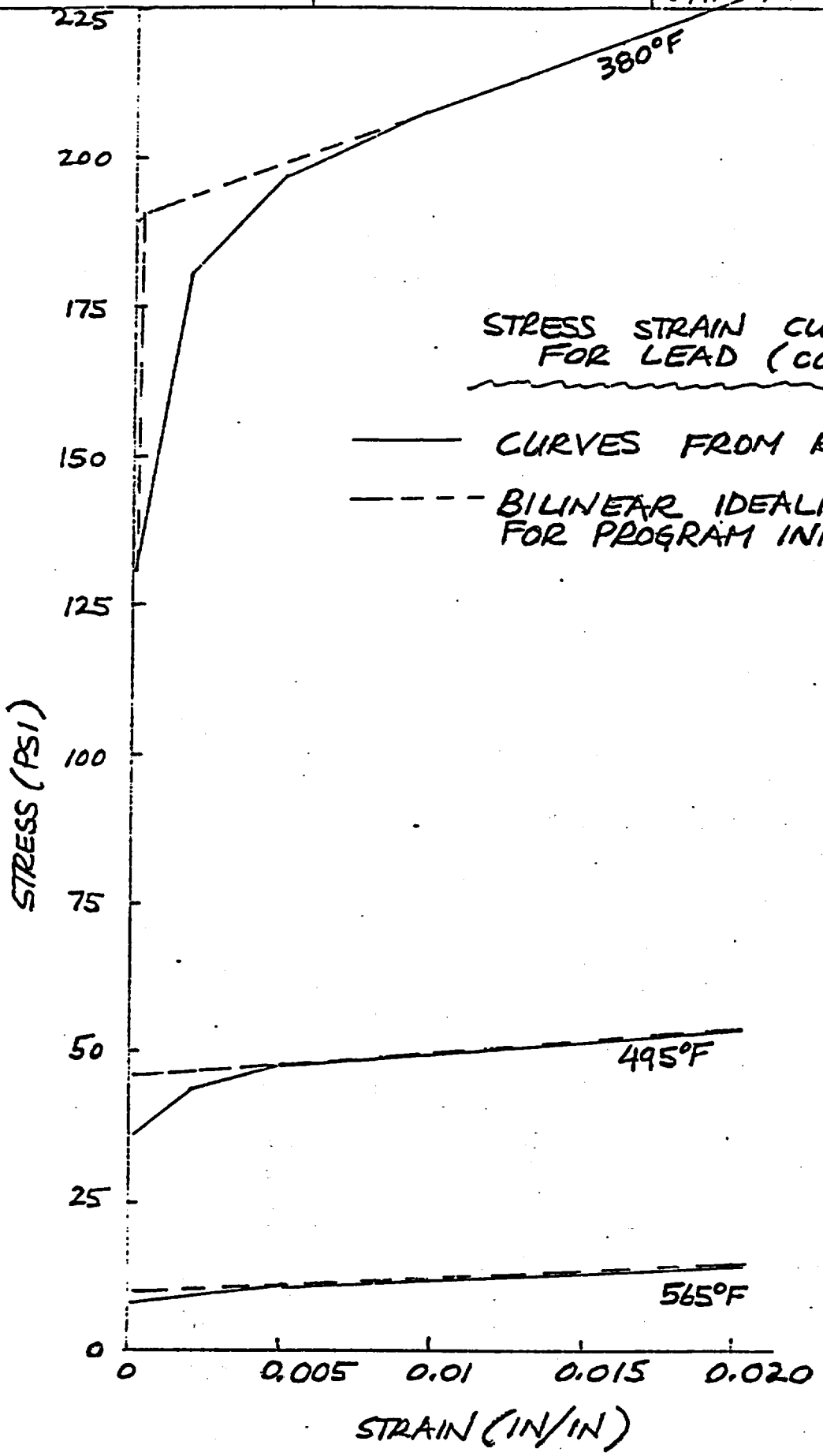

STRESS STRAIN CURVES FOR LEAD (CONT.)

——— CURVES FROM REF. 3

– – – – BILINEAR IDEALIZATION FOR PROGRAM INPUT

Expression for Steady-Creep of Lead

To input the creep of lead into the ANSYS Program the creep data of Ref. 20 must be converted to an Empirical Expression. The Steady-State creep of the lead will be considered and the primary creep assumed small. The Empirical Expression selected is:

$$\dot{\epsilon} = A e^{-\frac{k}{T_r}} \sigma^m$$

Where:

$\dot{\epsilon}$ = Creep Rate in in./in./Hr.

A, k, & m = Empirical Constants Determined From Experimental Data

T_r = Temperature (Absolute)

σ = Stress (PSI)

From Ref. 20 the following Data was extracted:

TEMP °F	σ	$\dot{\epsilon}$
100	800 580 240	$1.0(10)^{-3}$ $1.9(10)^{-4}$ $6.25(10)^{-6}$
175	500 330 190	$1.33(10)^{-3}$ $1.80(10)^{-4}$ $1.63(10)^{-5}$
250	270 210 120	$2.30(10)^{-3}$ $2.95(10)^{-4}$ $6.0(10)^{-5}$
325	180 120 56	$4.3(10)^{-3}$ $4.95(10)^{-4}$ $7.00(10)^{-6}$

Expression for Steady-State Creep of Lead (Cont.)

On the following page the Ref. 4 Data is plotted ($\dot{\epsilon}$ vs. σ). The slope of the lines gives the m Parameter.

$$\dot{\epsilon} = A\, e^{-\frac{k}{T_r}}\, \sigma^m$$

$$\log \dot{\epsilon} = \log \left(A e^{-\frac{k}{T_r}}\right) + m \log \sigma$$

The slopes of the four lines

Temp°F	Slope $\dot{\epsilon}$ vs. σ
100	4.21
175	4.44
250	4.54
325	5.50

The average slope taken as m

$$m = 4.67$$

Computing the intercept at $\sigma = 1.0$ using the average slope yields:

Temp.	$A e^{-\frac{k}{T_r}}$ (= The $\sigma = 1.0$ intercept)
100	$2.70\ (10)^{-17}$
175	$2.93\ (10)^{-16}$
250	$9.76\ (10)^{-15}$
325	$5.82\ (10)^{-14}$

Writing the creep rate expression as

$$\log \dot{\epsilon}_{1.0} = 0.434\, k \left(\frac{1}{T_r}\right) + m \log 1.0^{\circ} + \log A$$

CREEP EXPRESSION FOR STEADY-CREEP OF LEAD (CONT.)

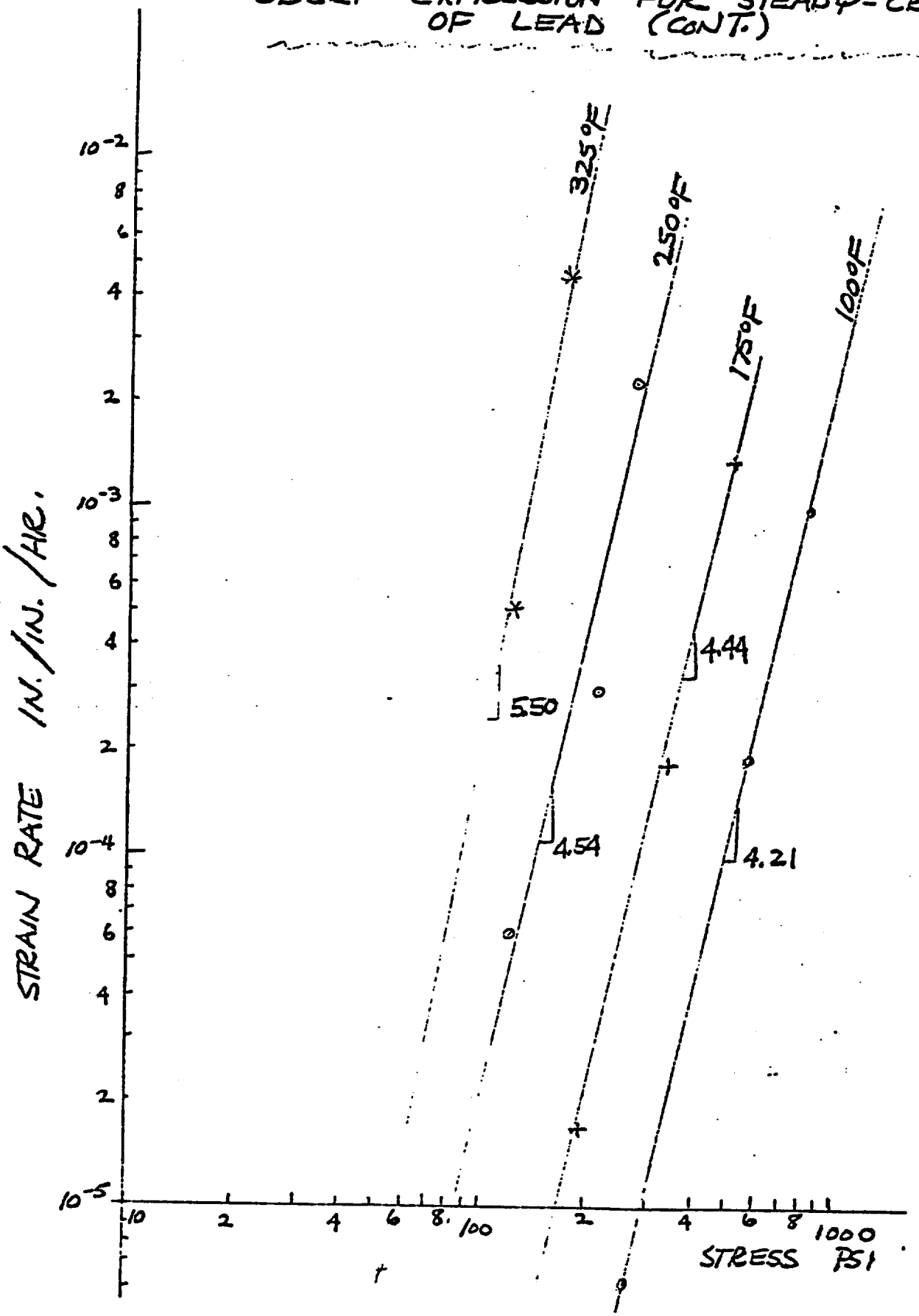

EXPRESSION FOR STEADY-STATE CREEP OF LEAD (CONT.)

PLOTING THIS LAST EXPRESSION ON SEMI-LOG AXIES WILL YIELD THE REMAINING REQUIRED CONSTANTS.

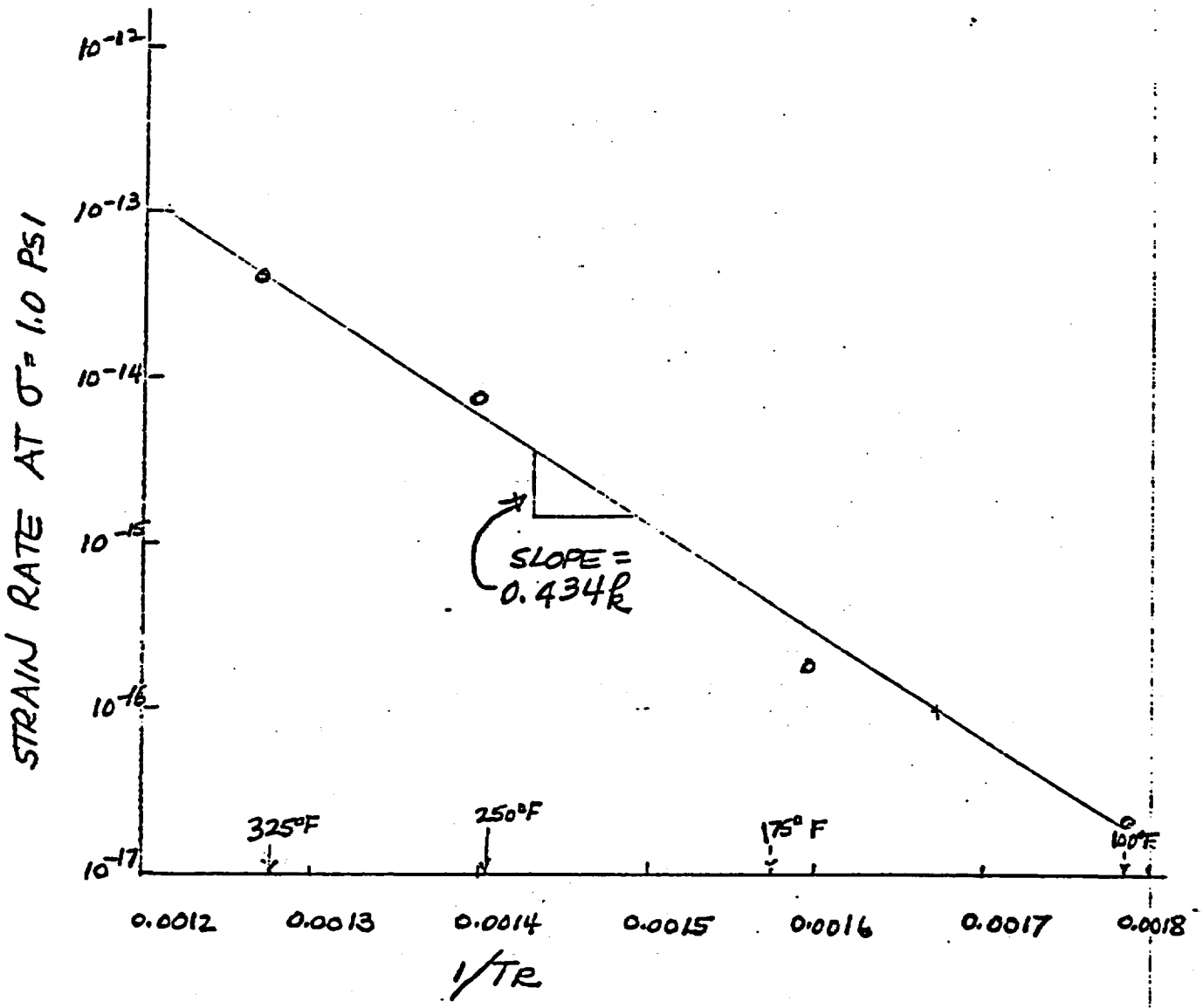

FROM THE SLOPE, THE CONSTANT k IS FOUND TO BE:

$$k = 15030.$$

Expression for Steady-State Creep of Lead (Cont.)

Including the k Parameter in the creep rate expression for $\sigma = 1.0$

$$\log \dot{\epsilon}_{1.0} = (-0.434)\,(15030.)\,\frac{1}{T_r} + \log A$$

Selecting a point from the last plot and solving for the A Parameter yields:

$$A = 7.82\,(10)^{-6}$$

Thus the final expression is:

$$\dot{\epsilon} = 7.82\,(10)^{-6}\; e^{\,-\frac{15030}{T_r}}\quad \delta\ 4.67 \text{ in/in/Hr}$$

Checking the expression against the original data extracted from Rev. 20 yields the following table:

TEMP °F	δ	$\dot{\epsilon}$ (EXP.)	$\dot{\epsilon}$ (EQN.)
100	800	$1.0\,(10)^{-3}$	$6.23(10)^{-4}$
	580	$1.9\,(10)^{-4}$	$1.39(10)^{-4}$
	240	$6.25\,(10)^{-6}$	$2.25(10)^{-6}$
175	500	$1.33\,(10)^{-3}$	$1.65(10)^{-3}$
	330	$1.80\,(10)^{-4}$	$2.37(10)^{-4}$
	190	$1.63\,(10)^{-5}$	$1.80(10)^{-5}$
250	270	$2.30\,(10)^{-3}$	$1.133(10)^{-3}$
	210	$2.95\,(10)^{-4}$	$3.50(10)^{-4}$
	120	$6.0\,(10)^{-5}$	$2.57(10)^{-5}$
325	180	$4.30(10)^{-3}$	$4.29(10)^{-3}$
	120	$4.95(10)^{-4}$	$1.94(10)^{-4}$
	56	$7.00(10)^{-6}$	$5.52(10)^{-6}$

THIS PAGE INTENTIONALLY LEFT BLANK

SECTION XI
APPENDIX C

Buckling Analysis of Concentric Shell Configuration

A buckling analysis of a three-layer cylindrical shell under various prebuckling states of stress is given below. Each layer is treated as an annular region with its own properties and its own prebuckling state of stress. Conditions of continuity of surface tractions and displacements are used to piece together the 3 layers into the composite shell. Boundary conditions at the ends of the shell are assumed to be analogous to the classical simple-support end conditions for a thin shell. These boundary conditions do not reflect the actual end conditions of the cask shell, however, they allow buckling modes which can be separated into independent sinusoidal functions in the axial and circumferential directions. Ordinary differential equations govern the radial dependence of the buckling modes. These equations are solved numerically. The final buckling condition, once the 3 layers are made compatible, is found when the determinant of a 6 x 6 stiffness-type matrix vanishes.

The formulation of the problem is exact. For simplicity it has been assumed that the prebuckling stresses and properties are uniform within each layer. The incremental moduli of a layer must be obtained from a plasticity theory as a function of the prebuckling stress. Deformation theory has been used to calculate the incremental moduli since it

represents a more conservative estimate of plastic buckling loads than flow theory (ie., Prandtl-Reuss theory).

The following derivation is based on a single layer segment. The computer program solution combines the three concentric segments and satisfies strain compatibility and equilibrium of interface traction forces.

From figure 1, the stress rate-strain rate relations at the instant of bifurcation are:

$$\dot{\sigma}_{rr} = C_{11}\dot{\varepsilon}_{rr} + C_{12}\dot{\varepsilon}_{\theta\theta} + C_{13}\dot{\varepsilon}_{xx}$$

$$\dot{\sigma}_{\theta\theta} = C_{12}\dot{\varepsilon}_{rr} + C_{22}\dot{\varepsilon}_{\theta\theta} + C_{23}\dot{\varepsilon}_{xx}$$

$$\dot{\sigma}_{xx} = C_{13}\dot{\varepsilon}_{rr} + C_{23}\dot{\varepsilon}_{\theta\theta} + C_{33}\dot{\varepsilon}_{xx}$$

$$\dot{\sigma}_{r\theta} = 2C_{44}\dot{\varepsilon}_{r\theta}\,,\quad \dot{\sigma}_{rx} = 2C_{55}\dot{\varepsilon}_{rx}\,,\quad \dot{\sigma}_{\theta x} = 2C_{66}\dot{\varepsilon}_{\theta x}\,,$$

and the strain rate-displacement rate equations are;

$$\left.\begin{aligned} &\dot{\varepsilon}_{rr} = \dot{W}_{,r}\,,\quad \dot{\varepsilon}_{\theta\theta} = r^{-1}(\dot{V}_{,\theta} + \dot{W})\,,\quad \dot{\varepsilon}_{xx} = \dot{U}_{,x} \\ &\dot{\varepsilon}_{r\theta} = \tfrac{1}{2}(\dot{V}_{,r} + r^{-1}\dot{W}_{,\theta} - r^{-1}\dot{V})\,,\quad \dot{\varepsilon}_{rx} = \tfrac{1}{2}(\dot{U}_{,r} + \dot{W}_{,x}) \\ &\dot{\varepsilon}_{\theta x} = \tfrac{1}{2}(r^{-1}\dot{U}_{,\theta} + \dot{V}_{,x}) \end{aligned}\right\} \quad (1)$$

The incremental form of the principal of virtual work(ref. 1) in terms of the strain-displacement variations is;

$$\int_V \left\{ \dot{\sigma}_{ij}\,\delta\varepsilon_{ij} + \overset{\circ}{\sigma}_{ij}\,\dot{u}_{k,i}\,\delta u_{k,j} \right\} dV = \int_S \dot{T}_i\,\delta u_i\,dS \qquad (2)$$

Specialization of equation 2 to cylindrical coordinates and setting the coeficients of the variation on w, v, and u to zero, the equilibirum equations and boundary conditions are as follows.

$$\dot{\sigma}_{rr,r} + r^{-1}\dot{\sigma}_{r\theta,\theta} + \dot{\sigma}_{rx,x} + r^{-1}(\dot{\sigma}_{rr} - \dot{\sigma}_{\theta\theta}) + \overset{\circ}{\sigma}_{rr}(\dot{w}_{,rr} + r^{-1}\dot{w}_{,r})$$

$$+ \overset{\circ}{\sigma}_{\theta\theta}\, r^{-2}(\dot{w}_{,\theta\theta} - 2\dot{v}_{,\theta} - \dot{w}) + \overset{\circ}{\sigma}_{xx}\,\dot{w}_{,xx} = 0 \qquad (3)$$

$$\overset{\circ}{\sigma}_{r\theta,r} + r^{-1}\dot{\sigma}_{\theta\theta,\theta} + \dot{\sigma}_{\theta x,x} + 2r^{-1}\dot{\sigma}_{r\theta} + \overset{\circ}{\sigma}_{rr}(\dot{v}_{,rr} + r^{-1}\dot{v}_{,r})$$

$$+ \overset{\circ}{\sigma}_{\theta\theta}\, r^{-2}(\dot{v}_{,\theta\theta} + 2\dot{w}_{,\theta} - \dot{v}) + \overset{\circ}{\sigma}_{xx}\,\dot{v}_{,xx} = 0 \qquad (4)$$

$$\dot{\sigma}_{rx,r} + r^{-1}\dot{\sigma}_{\theta x,\theta} + \dot{\sigma}_{xx,x} + r^{-1}\dot{\sigma}_{rx} + \overset{\circ}{\sigma}_{rr}(\dot{u}_{,rr} + r^{-1}\dot{u}_{,r})$$

$$+ \overset{\circ}{\sigma}_{\theta\theta}\, r^{-2}\dot{u}_{,\theta\theta} + \overset{\circ}{\sigma}_{xx}\,\dot{u}_{,xx} = 0 \qquad (5)$$

The boundary conditions on the lateral sides of the shells are;

$$\dot{T}_r = \dot{\sigma}_{rr} + \overset{\circ}{\sigma}_{rr}\,\dot{w}_{,r} \quad \text{on (fig. C-1)} \quad r = r_I, r_o \qquad (6)$$

$$\dot{T}_\theta = \dot{\sigma}_{r\theta} + \mathring{\sigma}_{rr}\dot{v}_{,r} \quad \text{on (fig. C-1)} \quad r = r_I, r_o$$

$$\dot{T}_x = \dot{\sigma}_{rx} + \mathring{\sigma}_{rr}\dot{u}_{,r} \quad \text{on (fig. C-1)} \quad r = r_I, r_o$$

The buckling mode shapes are assumed to be of the form;

$$\left.\begin{aligned} \dot{w} &= f(r)\sin\lambda x \sin\eta\theta \\ \dot{v} &= g(r)\sin\lambda x \cos\eta\theta \\ \dot{u} &= h(r)\cos\lambda x \sin\eta\theta \end{aligned}\right\} \qquad (7)$$

Substituting these expressions into equation 1, and the stress rate-strain rate relations yields the following;

$$\dot{\varepsilon}_{r\theta} = f\,ss\,,\quad \dot{\varepsilon}_{\theta\theta} = r^{-1}(-\eta g + f)\,ss\,,\quad \dot{\varepsilon}_{xx} = -h\lambda\,ss$$

$$\dot{\varepsilon}_{r\theta} = \tfrac{1}{2}(g' + r^{-1}f\eta - r^{-1}g)\,sc\,,\quad \dot{\varepsilon}_{rx} = \tfrac{1}{2}(h' + f\lambda)\,cs$$

$$\dot{\varepsilon}_{\theta x} = \tfrac{1}{2}(r^{-1}h\eta + g\lambda)\,cc$$

$$\dot{\sigma}_{rr} = \left[C_{11}f' + C_{12}r^{-1}(-\eta g + f) - C_{13}h\lambda\right]ss$$

$$\dot{\sigma}_{\theta\theta} = \left[C_{12}f' + C_{22}r^{-1}(-\eta g + f) - C_{23}h\lambda\right]ss$$

$$\dot{\sigma}_{xx} = \left[C_{13}f' + C_{23}r^{-1}(-\eta g + f) - C_{33}h\lambda\right]ss$$

$$\dot{\sigma}_{r\theta} = C_{44}\left(g' + r^{-1} f \eta - r^{-1} g\right) sc$$

$$\dot{\sigma}_{rx} = C_{55}\left(h' + f\lambda\right) cs$$

$$\dot{\sigma}_{\theta x} = C_{66}\left(r^{-1} h \eta + g\lambda\right) cc$$

For $0 \le x \le L$, $0 < \theta \le 2\pi$ with $\lambda = \frac{m\pi}{L}$, $m = 1, 2, \cdots$, $\eta = 1, 2, 3 \cdots$, the above modes satisfy the boundary conditions which are analogous to the simply supported conditions for a thin shell, namely that on the ends of the shell,

$\dot{w} = 0$, $\dot{v} = 0$, $\dot{\sigma}_{xx} = 0$.

By integrating through the thickness,

$$\dot{N}_{xx} = \int \dot{\sigma}_{xx}\, dr = 0$$

$$\dot{M}_{xx} = \int \dot{\sigma}_{xx}\, r\, dr = 0$$

Substituting these expressions back into the equilibrium and boundary condition equations results in;

Equation 3

$$C_{11} f'' + C_{12} r^{-1}(-\eta g' + f') - C_{12} r^{-2}(-\eta g + f) - C_{13} h'\lambda$$
$$- C_{44} r^{-1}(g'\eta + r^{-1} f \eta^2 - r^{-1} g \eta) - C_{55}(h'\lambda + f\lambda^2)$$
$$+ (C_{11} - C_{12}) r^{-1} f' + (C_{12} - C_{22}) r^{-2}(-\eta g + f) + (C_{23} - C_{13}) r^{-1} h \lambda$$
$$+ \sigma^{\circ}_{rr}(f'' + r^{-1} f') + \sigma^{\circ}_{\theta\theta} r^{-2}(-(1+\eta^2) f + 2 g \eta) - \sigma^{\circ}_{xx} f \lambda^2 = 0$$

Equation 4

$$C_{44}(g''+r^{-1}f'\eta - r^2 f\eta - r^{-1}g' + r^{-2}g) + C_{12}r^{-1}f'\eta + C_{12}r^{-2}(-\eta^2 g + f\eta)$$
$$- C_{23}r^{-1}h\lambda\eta - C_{66}(r^{-1}h\lambda\eta + g\lambda^2) + 2C_{44}r^{-1}(g' + r^{-1}f\eta - r^{-1}g)$$
$$+ \sigma^{\circ}_{rr}(g'' + r^{-1}g') + \sigma^{\circ}_{\theta\theta}(-(1+\eta^2)g + 2f\eta) - \sigma^{\circ}_{xx}g\lambda^2 = 0$$

Equation 5

$$C_{56}(h'' + f'\lambda) - C_{66}r^{-1}(r^{-1}h\eta^2 + g\lambda\eta) + C_{13}f'\lambda + C_{23}r^{-1}(-g\lambda)\eta + f\lambda)$$
$$- C_{33}h\lambda^2 + C_{55}r^{-1}(h' + f\lambda) + \sigma^{\circ}_{rr}(h'' + r^{-1}h')$$
$$- \sigma^{\circ}_{\theta\theta}r^{-2}h\eta^2 - \sigma^{\circ}_{xx}h\lambda^2 = 0$$

The surface tractions on $r = r_i$ and $r = r_o$ becomes;

$$\dot{T}_r = \left[C_{11}f' + C_{12}r^{-1}(-\eta g + f) - C_{13}h\lambda + \sigma^{\circ}_{rr}f'\right]ss \equiv \overline{T}_r\, ss$$

$$\dot{T}_\theta = \left[C_{44}(g' + r^{-1}f\eta - r^{-1}g) + \sigma^{\circ}_{rr}g'\right]sc \equiv \overline{T}_\theta\, sc$$

$$\dot{T}_x = \left[C_{56}(h' + f\lambda) + \sigma^{\circ}_{rr}h'\right]cs \equiv \overline{T}_x\, cs$$

Now let $\quad Y = (f', g', h', f, g, h)$

$$Y' = (f'', g'', h'', f', g', h')$$

and equations 3,4, and 5 can be written as;

$$Y' + A\,Y = 0 \qquad (8)$$

where A is a 6x6 matrix.
From page C-4 we find;
with,

$$\mu_1 = (C_{11} + \overset{\circ}{\sigma}_{rr})^{-1},\ \mu_2 = (C_{44} + \overset{\circ}{\sigma}_{rr})^{-1},\ \mu_3 = (C_{55} + \overset{\circ}{\sigma}_{rr})^{-1}$$

$$A_{11} = \mu_1 \left[C_{11} r^{-1} + \overset{\circ}{\sigma}_{rr} r^{-1} \right] = r^{-1}$$

$$A_{12} = \mu_1 \left[-(C_{12} + C_{44}) r^{-1} \eta \right]$$

$$A_{13} = \mu_1 \left[-(C_{13} + C_{55}) \lambda \right]$$

$$A_{14} = \mu_1 \left[-C_{22} r^{-2} - C_{44} r^{-2} \eta^2 - C_{55} \lambda^2 - \overset{\circ}{\sigma}_{\theta\theta} (1+\eta^2) r^{-2} - \overset{\circ}{\sigma}_{xx} \lambda^2 \right]$$

$$A_{15} = \mu_1 \left[C_{22} r^{-2} \eta + C_{44} r^{-2} \eta + 2 r^{-2} \overset{\circ}{\sigma}_{\theta\theta} \eta \right]$$

$$A_{16} = \mu_1 \left[(C_{23} - C_{13}) r^{-1} \lambda \right]$$

$$A_{21} = \mu_2 \left[C_{44} r^{-1} \eta + C_{12} r^{-1} \eta \right]$$

$$A_{22} = \mu_2 \left[C_{44} r^{-1} + \overset{\circ}{\sigma}_{rr} r^{-1} \right]$$

$$A_{23} = 0$$

$$A_{24} = \mu_2 \left[C_{44} r^{-2} \eta + C_{22} r^{-2} \eta + 2 \overset{\circ}{\sigma}_{\theta\theta} r^{-2} \eta \right]$$

$$A_{26} = \mu_2 \left[-C_{44} r^{-2} - C_{22} r^{-2} \eta^2 - C_{66} \lambda^2 - \overset{\circ}{\sigma}_{\theta\theta} r^{-2} (1+\eta^2) - \overset{\circ}{\sigma}_{xx} \lambda^2 \right]$$

$$A_{26} = \mu_2 \left[-C_{23} r^{-1} \lambda \eta - C_{66} r^{-1} \lambda \eta \right]$$

$$A_{31} = \mu_3 \left[C_{55} \lambda + C_{13} \lambda \right]$$

$$A_{32} = 0$$

$$A_{33} = \mu_3 \left[C_{55} r^{-1} + \overset{\circ}{\sigma}_{rr} r^{-1} \right] = r^{-1}$$

$$A_{34} = \mu_3 \left[C_{23} r^{-1} \lambda + C_{55} r^{-1} \lambda \right]$$

$$A_{35} = \mu_3 \left[-C_{66} r^{-1} \lambda \eta - C_{23} r^{-1} \lambda \eta \right]$$

$$A_{36} = \mu_3 \left[-C_{66} r^{-2} \eta^2 - C_{33} \lambda^2 - \overset{\circ}{\sigma}_{\theta\theta} r^{-2} \eta^2 - \overset{\circ}{\sigma}_{xx} \lambda^2 \right]$$

$$A_{41} = -1 \quad (A_{4i} = 0, \; i \neq 1)$$

$$A_{52} = -1 \quad (A_{5i} = 0, \; i \neq 2)$$

$$A_{63} = -1 \quad (A_{6i} = 0, \; i \neq 3)$$

The numerical solution procedure in the annular region begins with the solution of equation 8.

Let $\Delta = (r_o - r_I)/N$

$r_i = r_I + \Delta(i-1)$

$Y_i \equiv Y(r_i)$

$Y_i' = (Y_{i+1} - Y_i)/\Delta$

Equation 8 becomes;

$$\frac{Y_{i+1} - Y_i}{\Delta} + A_i \frac{(Y_{i+1} + Y_i)}{2} = 0$$

where A_i is evaluated at $r_i + \Delta/2$

$$\left(I + \tfrac{\Delta}{2} A_i\right) Y_{i+1} = \left(I - \tfrac{\Delta}{2} A_i\right) Y_i$$

$$Y_{i+1} = \left[\left(I + \tfrac{\Delta}{2} A_i\right)^{-1}\left(I - \tfrac{\Delta}{2} A_i\right)\right] Y_i \equiv Q_i Y_i$$

$$Y_{N+1} = \left[Q_N Q_{N-1} \cdots Q_2 Q_1\right] Y_1$$

$$Y_{N+1} = H Y_1$$

Now let $X_I = (\bar{T}_{rI}, \bar{T}_{\theta I}, \bar{T}_{xI}, f(r_I), g(r_I), h(r_I))$

and $X_o = (\bar{T}_{ro}, \bar{T}_{\theta o}, \bar{T}_{xo}, f(r_o), g(r_o), h(r_o))$

Introduce, $X_o = K_L X_L$ where K_L is a 6x6 matrix.

Now, $X = R Y$ where R is a 6x6 matrix.

$R_{11} = C_{11} + \bar{\sigma}^{o}_{rr}$, $R_{14} = C_{12} r^{-1}$, $R_{15} = -C_{12} r^{-1} \eta$, $R_{16} = -C_{13} \lambda$

$$R_{22} = C_{44} + \sigma^{o}_{rr} \; , \; R_{24} = C_{44}\, r^{-1} \eta \; , \; R_{25} = -C_{44}\, r^{-1}$$

$$R_{33} = C_{55} + \sigma^{o}_{rr} \; , \; R_{34} = C_{55}\, \lambda$$

$$R_{44} = 1 \; , \; R_{55} = 1 \; , \; R_{66} = 1 .$$

All other components are zero.

Thus, $$X_0 = R_0\, Y_{N+1} = K_L\, R_I\, Y_1$$

$$Y_{N+1} = \left[R_0^{-1} K_L R_I \right] Y_1$$

$$= H\, Y_1$$

and $$K_L = R_0\, H\, R_I^{-1}$$

The buckling of a single shell under dead load surface loads ($\bar{T}_{RI} = \bar{T}_{\theta I} = \bar{T}_{xI} = \bar{T}_{R0} = \bar{T}_{\theta 0} = \bar{T}_{x0} = 0$) is:

$$\begin{bmatrix} 0 \\ U_0 \end{bmatrix} = K_L \begin{bmatrix} 0 \\ U_I \end{bmatrix}$$

where $$U_0 \equiv \left(f(r_0), g(r_0), h(r_0) \right)$$

$$U_I \equiv \left(f(r_I), g(r_I), h(r_I) \right)$$

Let $\overset{*}{U} = (U_0, U_I)$ and rearrange the above equations according to

$$K \overset{*}{U} = 0$$

where K is a 6x6 matrix given by

$$K_{ij} = 0 \qquad i = 1,3 \; ; \; j = 1,3$$

$$K_{ij} = -K_{L\,ij} \qquad i = 1,3 \; ; \; j = 4,6$$

$$K_{ij} = \delta_{i,j+3} \qquad i = 4,6 \; ; \; j = 1,3$$

$$K_{ij} = -K_{L\,ij} \qquad i = 4,6 \; ; \; j = 4,6$$

The criteria for buckling is that the determinant of K equal zero, $|K| = 0$. (9)

The buckling condition for the three layer composite shell is as follows;

$X_o = K_L X_I$ middle shell (see fig. 2)

$X_I = K_I X_1$ inside shell

$X_2 = K_o X_o$ outside shell

$$X_2 = K_o X_o = K_o K_L X_I = K_o K_L K_I X_1$$

let $M = K_o K_L K_I$ (6x6 matrix)

Write $X_2 = \{T_2, U_2\}$, $X_1 = \{T_1, U_1\}$

$T_1 = (\bar{T}_{r1}, \bar{T}_{\theta 1}, \bar{T}_{x1})$, $U_1 = (f(r_1), g(r_1), h(r_1))$

$T_2 = (\bar{T}_{r2}, \bar{T}_{\theta 2}, \bar{T}_{x2})$, $U_2 = (f(r_2), g(r_2), h(r_2))$

$$\begin{bmatrix} T_2 \\ U_2 \end{bmatrix} = M \begin{bmatrix} T_1 \\ U_1 \end{bmatrix}$$

Since $T_2 = T_1 = 0$ at the instant of buckling then

$$\begin{bmatrix} 0 \\ U_2 \end{bmatrix} = M \begin{bmatrix} 0 \\ U_1 \end{bmatrix}$$

or $K U^* = 0$ where $U^* = (U_2, U_1)$

where K is given by

$$K_{ij} = 0 \qquad i = 1,3 \; ; \; j = 1,3$$

$$K_{i,j+3} = -M_{i,j+3} \qquad i = 1,3 \; ; \; j = 1,3$$

$$K_{i+3,j} = \begin{cases} 1 & i = j \\ 0 & i \neq j \end{cases} \qquad i = 1,3 \; ; \; j = 1,3$$

$$K_{i+3,j+3} = -M_{i+3,j+3} \qquad i = 1,3 \; ; \; j = 1,3$$

The buckling condition therefore becomes $|K| = 0$ (10)

The moduli from J_2 - deformation theory used in this solution is as follows;(ref. 1)

Let $S_{ij} = \sigma_{ij} - \frac{1}{3}\sigma_{pp}\delta_{ij}$; $\sigma_e = \sqrt{\frac{3}{2} S_{ij} S_{ij}}$ effective stress

with $\overset{*}{\sigma}_{ij} = \bar{L}_{ijkl}\dot{\varepsilon}_{kl}$

therefore the moduli are;

$$\bar{L}_{ijkl} = \frac{E}{1+\nu+g}\left\{\frac{1}{2}(\delta_{ik}\delta_{jl} + \delta_{il}\delta_{jk}) + \frac{3\nu+g}{3(1-2\nu)}\delta_{ij}\delta_{kl} - \frac{g' S_{ij} S_{kl}}{1+\nu+g+4g'\sigma_e^2/2}\right\}$$

where

$$g = \frac{3}{2}\left[\frac{E}{E_s} - 1\right] \; , \; g' = \frac{9}{4}\frac{E}{\sigma_e^2}\left[\frac{1}{E_t} - \frac{1}{E_s}\right]$$

The formulation up to this point, is exact if one identifies the stress increments correctly as the physical components of the rates of the convected contravarient components of the Kirchkoff stress. The rates in equation II are taken as the Jaumann rates of the Cauchy stress since these rates are the "true" stress rates and are consistent with the definitions of tangent and secant moduli . When the stress levels are comparable to the moduli, it is necessary to distinguish between the two rates. The conversion, (ref. 2), of the moduli from $\overset{*}{\sigma}_{ij} = \bar{L}_{ijkl}\dot{\varepsilon}_{kl}$ to $\overset{\circ}{\sigma}_{ij} = L_{ijkl}\dot{\varepsilon}_{kl}$ is given by

$$L_{ijkl} = \bar{L}_{ijkl} - \frac{1}{2}\left[\delta_{ik}\overset{\circ}{\sigma}_{jl} + \delta_{jk}\overset{\circ}{\sigma}_{il} + \delta_{il}\overset{\circ}{\sigma}_{jk} + \delta_{jl}\overset{\circ}{\sigma}_{ik}\right]$$

In the derivation of equation 10 it is assumed that the hydrostatic pressure is small compared with the elastic bulk modulus, otherwise, the conversion is exact and

$$C_{11} = L_{1111}\ , \quad C_{12} = L_{1122}$$

$$C_{44} = L_{1212}$$

A more simplistic representation of the incremental moduli of an elastic-plastic material is sometimes convenient to use when the stress state is predominantly hydrostatic. This representation only involves the tangent modulus at the effective stress level and is generally extremely conservative when used in incremental buckling calculations, as will be discussed further below. Let E_t again denote the tangent modulus at the current level of $\bar{\sigma}_e$ and let B denote the elastic bulk modulus. The incremental moduli are taken to correspond to an isotropic solid with Young's modulus E_t and bulk modulus B. The associated shear modulus G_t is given by

$$\frac{1}{G_t} = \frac{3}{E_t} - \frac{1}{B}\ ,$$

The relation between the stress-rates and strain-rates in this "isotropic theory" is

$$\dot{\sigma}_{ij} = 2G_t \dot{e}_{ij} + \frac{1}{3} B \dot{\epsilon}_{kk} \delta_{ij}$$

where $\dot{e}_{ij} = \dot{\epsilon}_{ij} - \frac{1}{3}\dot{\epsilon}_{kk}\delta_{ij}$ is the deviator strain-rate. The term "isotropic theory" is perhaps misleading since it has nothing to do with isotropic strain hardening.

In this theory, the incremental moduli are all (except the

bulk modulus) proportional to the tangent shear modulus G_t and therefore very low compared to predictions of J_2 deformation theory and J_2 flow theory (i.e.,Prandtl-Reuss theory based on J_2). As an illustration consider an element of material subject to uniaxial compression into the plastic range, $\sigma_{11} = -\sigma_o$. Now calculate the incremental shear modulus, $\bar{G}$, for an increment of shear stress $\dot{\sigma}_{13}$, i.e.,

$$\dot{\epsilon}_{13} = \dot{\sigma}_{13}/(2\bar{G})$$

The isotropic theory gives

$$\bar{G} = G_t \cong \frac{E_t}{3}$$

where the latter holds if $B >> E_t$. The J_2 deformation theory gives

$$\bar{G} = G\left[1+3G(1/E_s-1/E)\right]^{-1} \cong E_s/3$$

where E_s is the secant modulus and G is the elastic shear modulus. On the other hand, J_2 flow theory (as well as any flow theory with a smooth yield surface) gives

$$\bar{G} = G$$

As is well known, buckling predictions based on moduli from J_2 flow theory are often unconservative. Those based on J_2 deformation theory, which predicts that all the incremental moduli will be reduced, are generally on the conservative side. The "isotropic theory" is even more conservative when used in buckling calculations since the moduli, as illustrated above, are reduced even further.

THIS PAGE INTENTIONALLY LEFT BLANK

Computer Program Verification

The results of HBUCK were compared to several classical buckling solutions in order to verify the theory and the compptational techniques used in the code. There should be slight differences in the comparison , due to the fact that Sanders' small deflection theory in HBUCK is more accurate than Donnell's theory when n (circumferential buckling mode number) is small. As the wave length of the buckling mode decreases (n increases) the difference in the two theories diminishes. The verification cases are disoussed in some detail as follows:

Case 1 Cylinder Under Lateral Pressure

A simply supported cylinder, 160" long, was evaluated for buckling under uniform lateral pressure along its length. From figure C-3, the HBUCK results indicate that the cylinder buckled at a critical hoop stress of $\sigma_T = -25400$ psi in the $m = 3$ buckling mode.

This was compared with the solution presented in NASA SP-8007, Buckling of Thin-Walled Circular Cylinders, (1965), which states that the critical buckling stress is:

$$\sigma_y = k_y \frac{\pi^2 E}{12(1-\mu^2)} \cdot \left(\frac{t}{\ell}\right)^2$$

where $$k_y = \frac{(1+\beta^2)^2}{\beta^2} + \frac{12}{\pi^4} \cdot \frac{\gamma^2 Z^2}{\beta^2(1+\beta^2)^2}$$

and $$\beta = \frac{m\ell}{\pi R}$$

For n=3, the classical critical buckling stress is -24,836 psi as compared to the -25400 psi from HBUCK. These results

compare within 2.2% which indicates good correlation.

Case 2 Cylinder Under Axial Compression

A cylinder under axial compression with dimensions shown in figure C-4 was analyzed. The classical solution used was:

$$\sigma_x = \frac{E}{\sqrt{3(1-\mu^2)}} \cdot \left(\frac{t}{R}\right) \quad \text{(NASA SP-8007)}$$

The classical solution resulted in a compressive stress of -516,000 psi as compared to -510,000 psi from HBUCK. These results are within 1% of each other, which indicates excellent correlation.

Case 3 Buckling of a Ring Under a Dead Load Pressure

The buckling of a ring with dimensions shown in figure C-4 under a dead load pressure is the solution of a pre-stressed ring on an elastic foundation.

$$P_c = \frac{E}{3(1-\mu^2)} \cdot \left(\frac{t}{R}\right)^3$$

The classical solution yields a buckling pressure of the 3.61 psi as compared to 3.58 psi from HBUCK. These results correlate with 0.8%.

Case 4 Brush-Pitner (Ref. 70)

HBUCK was compared with the work of Brush-Pitner (Ref. 70) as applied to the 10/24 Cask dimensions. The comparison is shown in figure C-6 which represents buckling pressure of the inner shell as a function of the tangent modulus of lead. Figure C-6 shows a very close correlation in the lower range

of lead tangent modulus applicable to the conditions in the Cask.

References

1. Hutchins on, J. W., (1974). Plastic Buckling. Adv. App. Mech. Vol. 14, pg. 87

2. Hill, R. (1967). On the classical constitutive relations for elastic/plastic solids. In "Recent Progress in Applied Mechanics", the Folke Odqvist Vol. pp. 241-249. Almqvist and Wiksell, Stockholm.

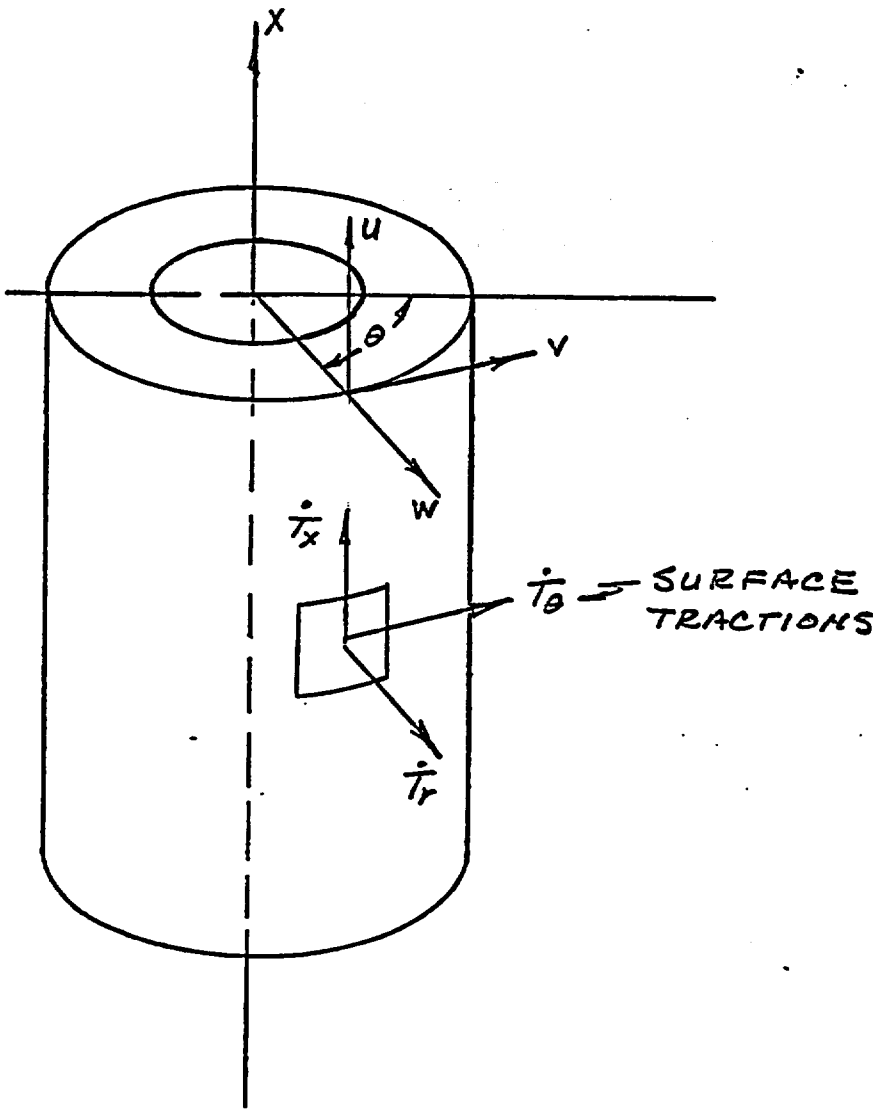

COORDINATES WITHIN A SINGLE SEGMENT

FIGURE C-1

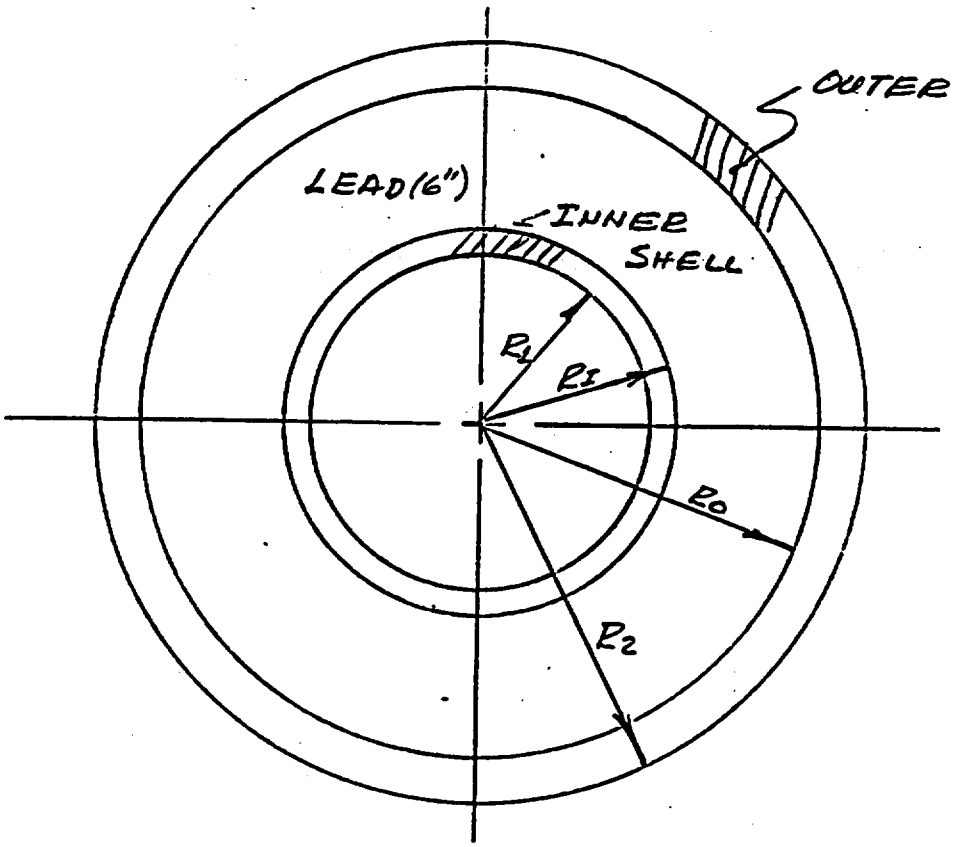

THREE SHELL COMPOSITE. NOTATION

FIGURE C-2

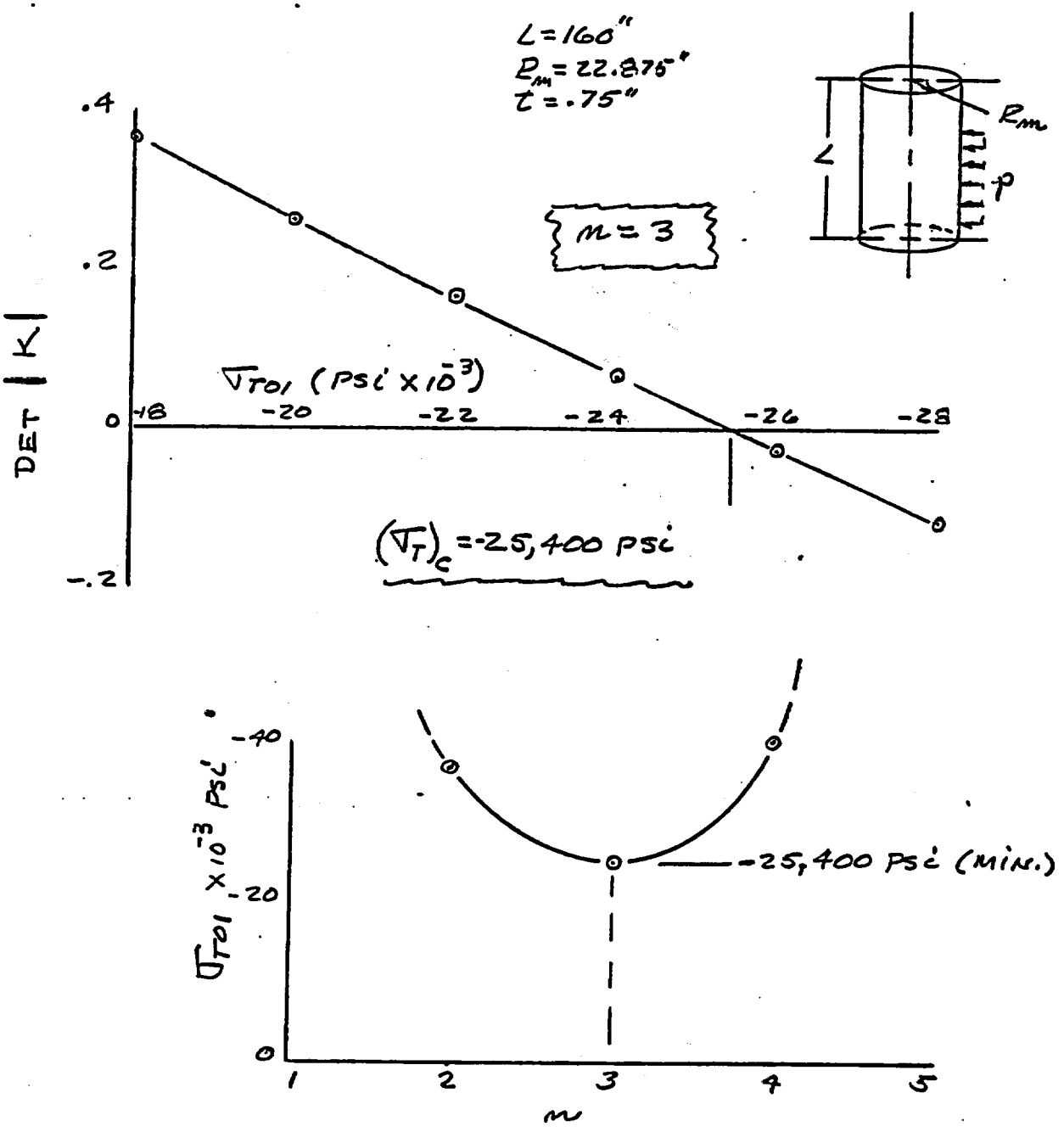

"HBUCK" RESULTS FOR BUCKLING OF CYLINDER WITH LATERAL PRESSURE

FIGURE C-3

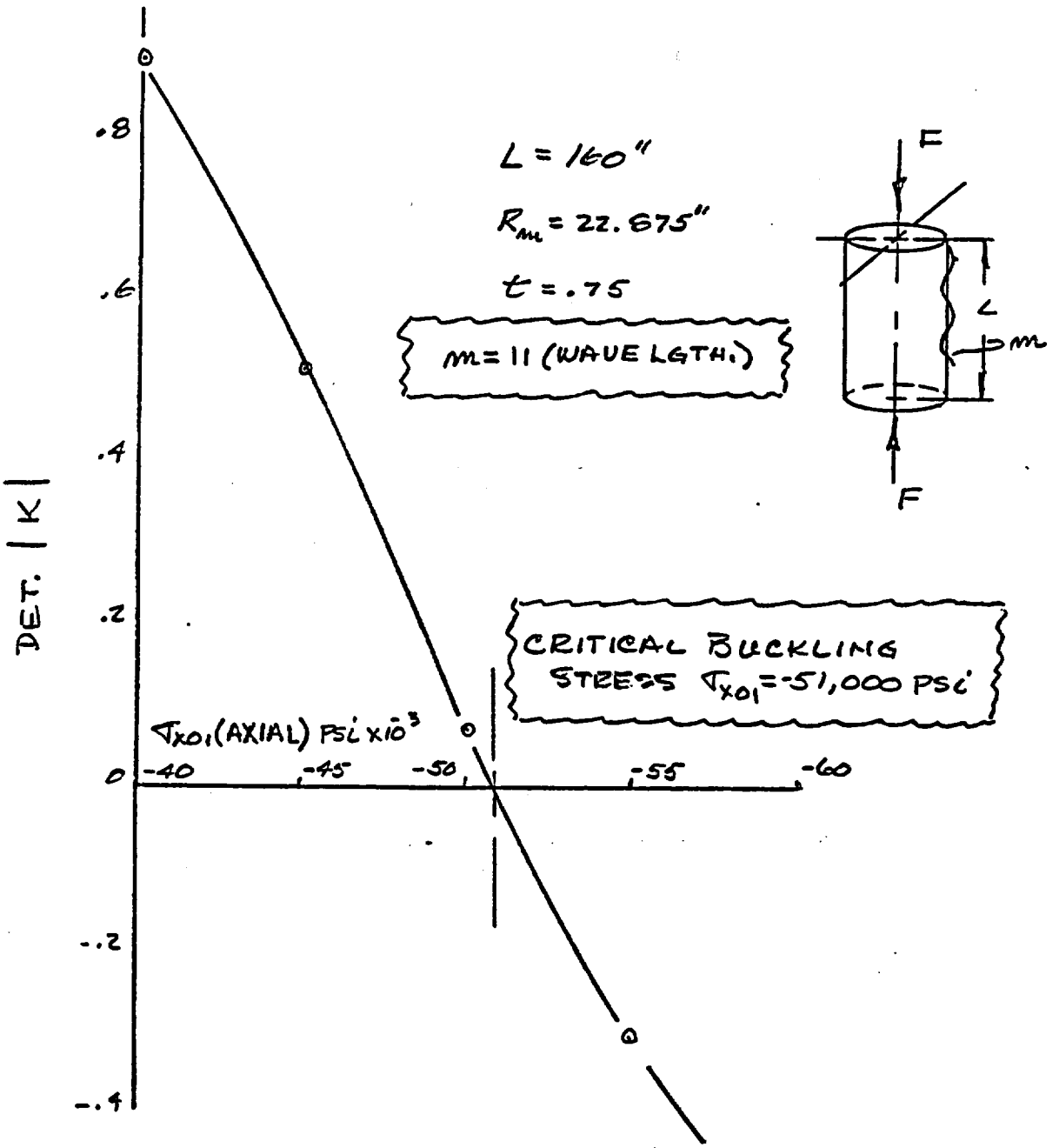

"HBUCK" RESULTS FOR BUCKLING OF CYLINDER WITH AXIAL LOAD

FIGURE C-4

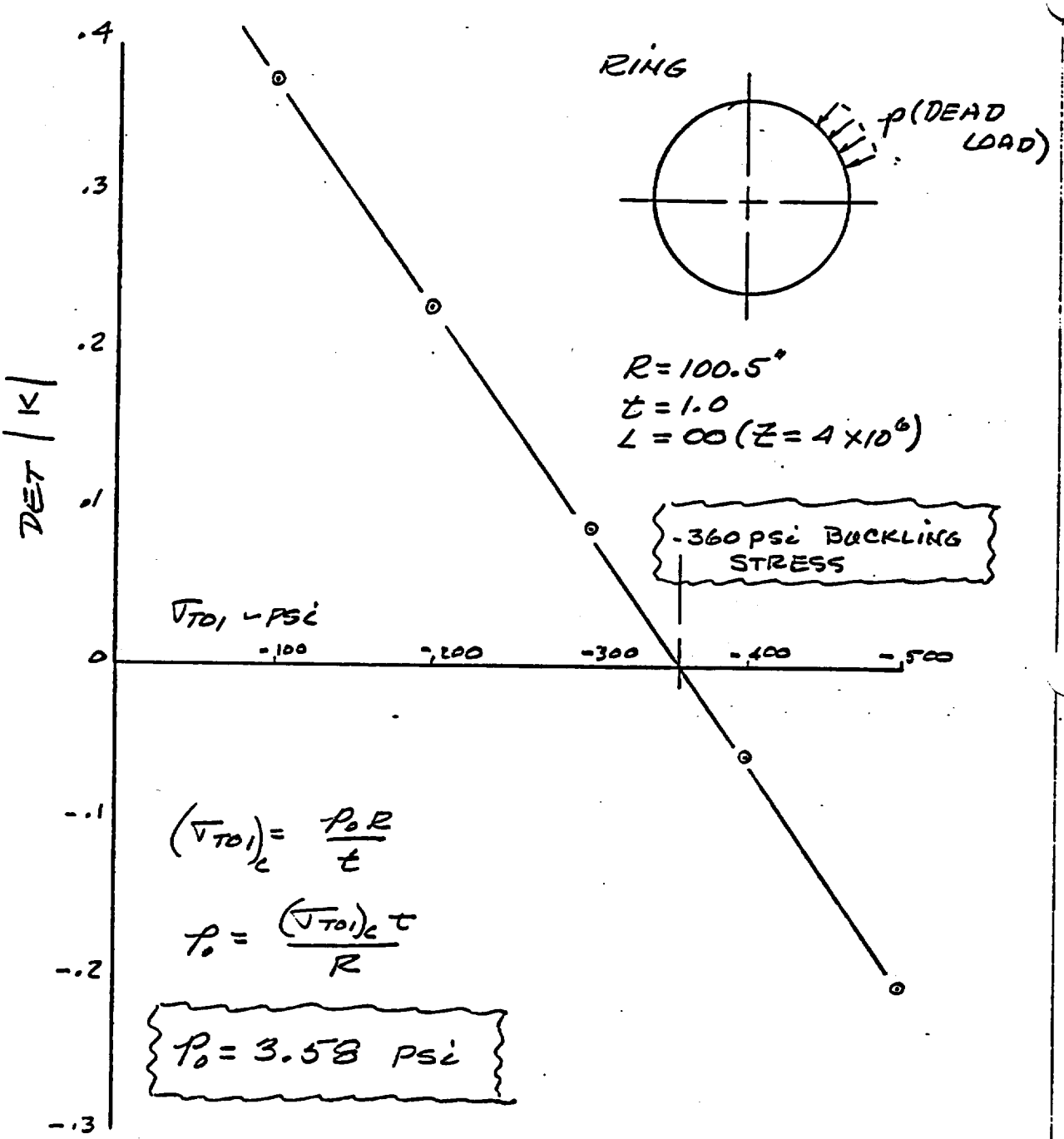

"HBUCK" RESULTS FOR BUCKLING OF LONG (RING) CYLINDER UNDER DEAD LOAD PRESSURE

FIGURE C-5

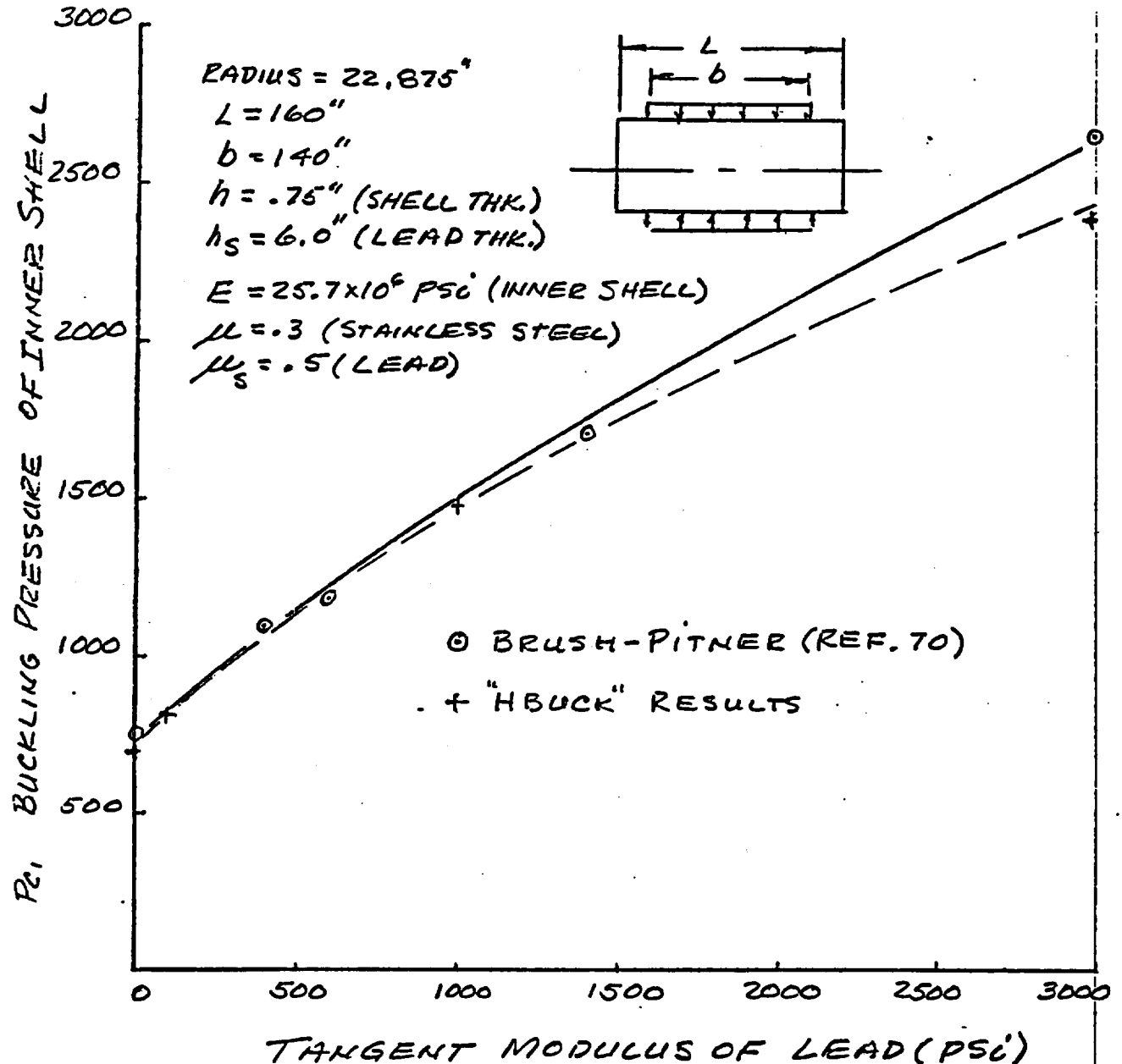

COMPARISON OF "HBUCK" PROGRAM WITH THE WORK OF BRUSH AND PITNER (1965)

FIGURE C-6

Section XI

Appendix D

Cask Model Test to Determine Lead Behavior in 30 Foot Drop Accident Test

A cask model constructed by NLI for Battelle's Columbus Laboratories was utilized by NLI to simulate lead behavior in the NLI 10/24 cask. The model cask, with lead shielding bonded to the steel walls, was used by BCL in similar lead slump tests at elevated temperatures. The BCL tests showed no significant lead movement which indicates that the lead and lead bond retained sufficient strength at elevated temperatures to resist the loads imposed by the end impact resulting from a 30 foot free fall onto an unyielding surface. The original configuration of the model is as shown on page XI-D-9. The model was designed to simulate a 1/3 scale model of the BCL-6 spent fuel shipping cask.

With the proper modifications, NLI considered the model to be an adequate representation of the NLI 10/24 rail cask for the purpose of demonstrating lead behavior at elevated temperatures. By adjusting the height of the lead column and the impact limiter performance, the loads imposed on the lead and lead bond as a result of end impact could be scaled to represent those expected to be experienced in the actual NLI 10/24 cask.

The bond between the lead shield and the steel walls was ultrasonically

tested. The tests showed that a bond existed over essentially 100% of the area of the cylindrical steel walls. Since the bond requirements on the NLI 10/24 cask permit a minimum of 75% bond, the load to be imposed on the bonded lead shielding was increased to account for the possible 25% difference in bond area between model and actual cask.

The bottom end of the original cask was cut off reducing the overall length of the cask to 52 inches. A new bottom plate $2\frac{1}{2}$ inches thick was machined to simulate the configuration of the bottom end of the NLI 10/24 cask. The principle feature is the support of the inner diameter of the lead shield while the outer diameter has no support and is free to move. The modifications to the original model are as shown on page XI-D-9. Four holes were drilled thru the bottom plate to provide access to the lead surface for the purpose of measuring any change in the position of the lead surface.

Test Procedure

Dimensions of certain cask features are to be taken and recorded as follows:

1. Bottom-lead position. Distance from outside surface of end plate to lead surface measured thru four holes in bottom plate spaced 90 degrees apart. Measurements to be taken at four different times.

a) at room temperature before drop.

b) at elevated temperature before drop.

c) at elevated temperature after drop.

d) at room temperature after drop.

2. Diameter of the cask. Two measurements taken 90 degrees apart and 1½ inches up from the bottom of the cask. Measurements to be taken at room temperature before and after drop test.

3. Cask length. Four measurements taken 90 degrees apart at room temperature before and after drop test.

4. Impact limiter height before and after drop test.

Thermocouples are to be attached to the exterior and interior of the assembly for temperature monitoring. Quartz accelerometers are to be attached to the top of the assembly to monitor the impact g-value.

The model is to be heated to a temperature of 400° F. The assembly shall then be elevated to position the bottom of the impact limiter 30 feet above the drop target. The model is to be released so as to permit a free fall with the vertical center line of the model perpendicular to the target surface.

Test Results

The cask model was prepared for the drop experiment at Battelle's

Columbus Laboratories (BCL). The model weight was 1066 lbs. The assembly was dimensioned and the values are presented in Table 1. Three thermocouples were tack welded to the exterior and interior of the assembly for temperature monitoring. Electrical heating tapes and an insulating blanket were wrapped on the exterior of the model, and it was heated to 400° F. Two quartz accelerometers were attached to the top of the assembly to monitor the impact g-value.

When the average of the temperatures indicated by the thermocouples attained 410° F., the distance to the lead surface at the bottom of the assembly was measured again as reported in Table 1.

The heaters were removed and the model was rewrapped in the insulating blanket. A balsa wood impact limiter was attached to the bottom of the model to provide a low g-force to the model during impact. The limiter was constructed to align the grain of the wood with the direction of force. Preliminary experiments with similar balsa wood limiters and a dummy drop weight indicated a g-value of 120 should be expected.

The assembly was elevated to position the bottom of the impact limiter 30 feet above the drop site. The elapsed time between discontinuing heating and making the drop was approximately 20 minutes; the estimated minimum assembly temperature was 380° F. The assembly was dropped on a 1-inch-thick steel plate resting on a thin bed of sand,

and restrained around the plate periphery by sand bags. In the drop, the assembly crushed and splintered the limiter, as expected, and than fell on its side. Approximately 10 minutes after the drop, the lead position at the bottom of the assembly was measured again (Table 1). The assembly was allowed to cool to room temperature, and all dimensions were measured again as shown in Table 1. The assembly did not display any visible exterior damage.

TABLE 1. MEASUREMENTS OF PHYSICAL DIMENSIONS OF THE NLI IMPACT MODEL CASK

Location		Pretest, inches R.T.	Pretest, inches 410 F	Post Test, inches 370 F	Post Test, inches R.T.
Bottom-Lead Position[a]					
	1	2.4840	2.4542	2.448	2.4651
	2	2.4795	2.4482	2.44	2.4563
	3	2.4818	2.4653	2.463	2.4730
	4	2.4875	2.4660	2.4635	2.4842
Diameter[b]					
	1-3	8.8515	--		8.8495
	2-4	8.8619	--		8.8661
Length					
	1	51-59/64	--	--	51-15/16
	2	51-29/32	--	--	51-29/32
	3	51-15/16	--	--	51-59/64
	4	51-59/64	--	--	51-15/16
Limiter Height		7.95	--	--	~4-5/8

(a) Distance from outside surface of end plate to lead surface. Four locations spaced 90 degrees apart.

(b) Taken 1-1/2 inch above bottom and 90 degrees from each other.

Based on the measured limiter deformation, the estimated average g-value was 110. This estimate was probably low owing to the manner in which the limiter yielded and splintered. The peak g-value as measured by the accelerometers was 150; the accelerometer output is reproduced in Figure 1. Examination of the data in Table 1 shows little change in the exterior dimensions of the model. The differences are attributed to the method of measurement and surface condition of the model. Comparison of lead position measurements indicates an average downward movement of 0.0136 inches. The dimensional changes in the lead can be considered as representing the actual lead behavior since there was no discernable change in the steel shells to mask the lead behavior.

In a bottom end impact of either the NLI 10/24 cask or the model, any axial movement of the unsupported part of the lead shield depends upon the bond shear stress. At the same shear stress both the 10/24 cask and the model would experience equal shear strains. Hence, the 10/24 cask, if subjected to the same bond shear stress as the model, would have a lead shield displacement greater than the model by the ratio of shield lengths, or (146/48.5)(0.0136) = 0.041 inches.

The shear stress in the model at the peak acceleration of 150 g was

$$\text{unsupported lead weight} = (\pi/4)(8.5^2 - 5.75^2)(48.5)(0.41) = 612 \text{ lb.}$$

$$\text{shear area} = \pi\,(8.5 + 5.75)(48.5) = 2171 \text{ in.}^2$$

$$\text{shear stress} = 150\,(612)/2171 = 42.3 \text{ psi}$$

The shear stress in the 10/24 cask at the 30 g acceleration which results from a 30 foot free fall is

unsupported lead weight = 34410 lb.

shear area @ 75% bond = $2\ \pi\ 29.25\ (0.75) + 26\ \ (146) = 43975$ in.^{2}

shear stress = $30\ (34410)/43975 = 23.5$ psi

The model test was thus conservative, since the bond shear stress in it was nearly twice the shear stress that would occur in the NLI 10/24 cask in a 30 foot bottom end impact.

The measurements of bottom-lead position (Table 1) indicate that only part of the total observed downward movement of the lead was due to the impact loading. The difference in lead position before and after impact with the model still at elevated temperature was only 0.0048 inches, or 0.0088 inches less than the total lead movement of 0.0136 inches observed when the model returned to room temperature after the test. Evidently, differential thermal expansion of the lead and the steel shells when the model was heated to 410° F caused the lead displacement of 0.0088 inches. In order to determine if repeated heating might cause further lead movement, the model was subjected to two additional thermal cycles between room temperature and 400° F. Bottom-lead position and outside diameter at two locations were measured before and after each thermal cycle with the results given in Table 2. No change in outside diameter was observed. The first thermal

cycle caused a small bottom-lead movement of 0.005 inches; no further movement occurred in the second thermal cycle (Table 2). Hence, the total bottom-lead movement that resulted from thermal cycling plus impact loading was 0.0186 inches. The equivalent total displacement at the bottom end of the lead shield in the 10/24 cask, if subjected to similar thermal and impact conditions as the model, would thus be (146/48.5)(0.0186) = 0.056 inches. This displacement is insignificant and is conservative in any case, since the expected impact and thermal conditions for the 10/24 cask are less severe than those imposed on the model.

The procedures followed in preparing the steel shells for bonding and pouring of the lead shielding are the same as those used in production of the prototype cask. ASTM B-29, chemical grade lead is used in both the model and the prototype cask.

TABLE 2

ADDITIONAL THERMAL CYCLE TESTS

OF NLI IMPACT MODEL CASK

Location	Dimension[a] (inches) Pretest	Post Cycle 1	Post Cycle 2
Bottom-Lead Position[b]			
1	2.467	2.462	2.462
2	2.459	2.453	2.455
3	2.485	2.475	2.474
4	2.481	2.481	2.482
Average	2.473	2.468	2.468
Outside Diameter[c]			
1-3	8.849	8.842	8.842
2-4	8.857	8.861	8.864
Average	8.853	8.852	8.853
Outside Diameter[d]			
1-3	8.857	8.856	8.856
2-4	8.867	8.868	8.869
Average	8.862	8.862	8.862

(a) Measurements taken with model at RT. Model thermal cycle was from RT to 400° F and back to RT.

(b) Outside of bottom to lead surface. Four places, 90° apart.

(c) Taken 1-1/2 inches from bottom, 90° apart.

(d) Taken 3 inches from bottom, 90° apart.

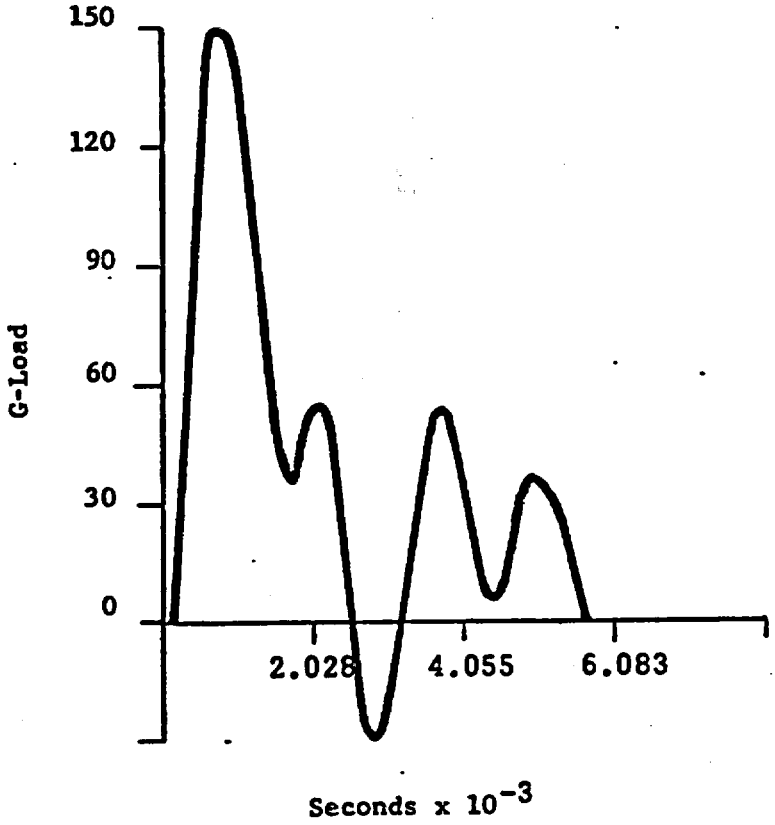

FIGURE 1. ACCELEROMETER OUTPUT FOR IMPACT OF NLI MODEL CASK

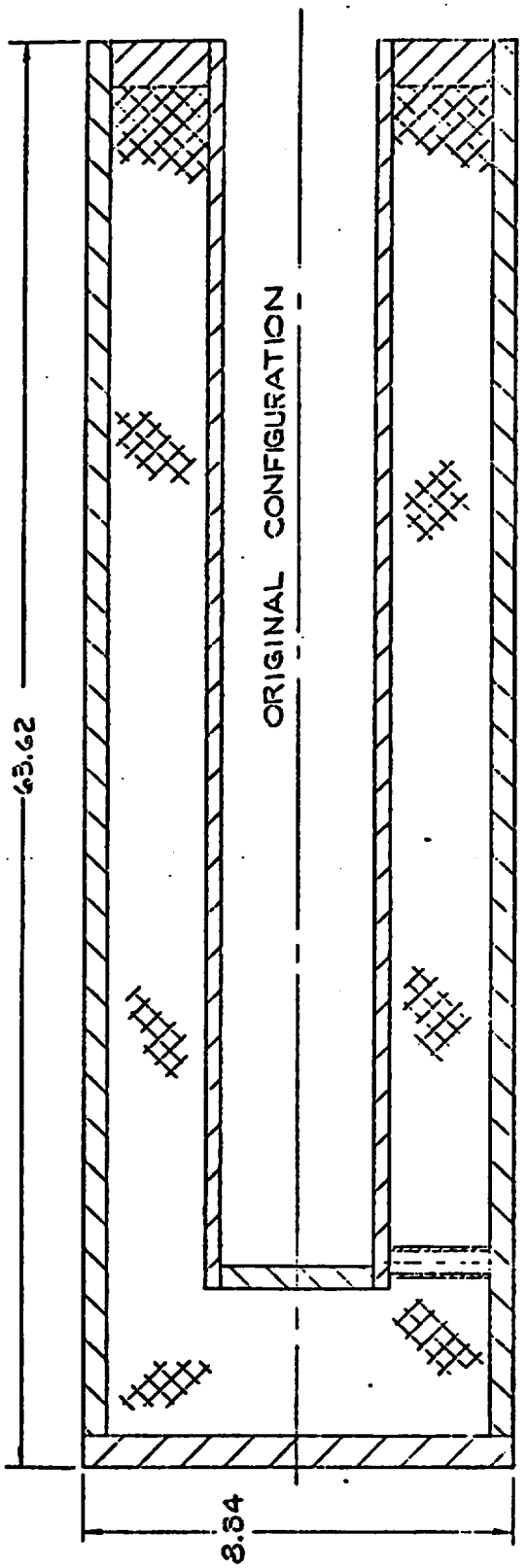
ORIGINAL CONFIGURATION
63.62
8.84

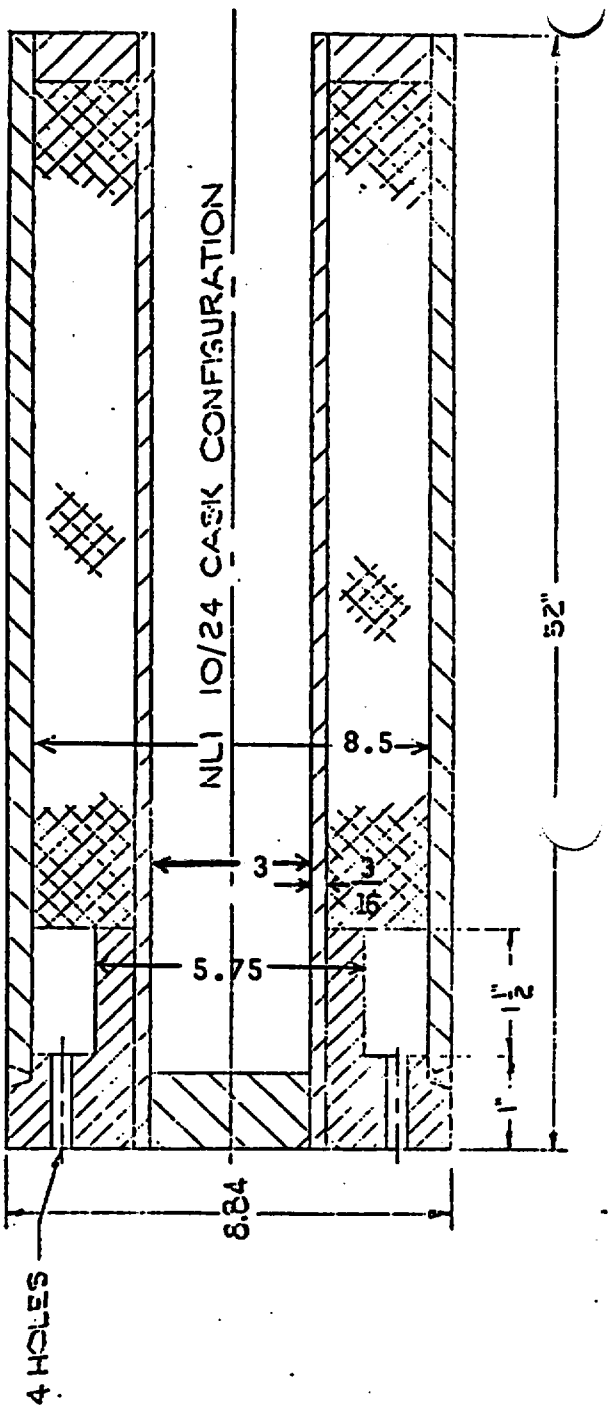
NLI 10/24 CASK CONFIGURATION
52"
8.5
3
3/16
5.75
1 1/2"
1"
8.84
4 HOLES

TEST OF ¼ SCALE PARTIAL CASK MODEL AT NORMAL AND POST-FIRE TEMPERATURES

A ¼ scale partial cask model was constructed in order to investigate interaction of the bonded lead shield with the inner and outer cask shells as a result of the lead casting operation and subsequent exposure to elevated temperatures. Configuration of the model is shown on page XI-D-13 . Bonding and pouring of the lead shielding (chemical grade, ASTM B-29) was carried out by the same procedures used in the prototype 10/24 cask. To simulate the minimum 75% bonding permitted in the prototype, unbonded areas (about 30 in^2 each) were located 180° apart at both inner and outer lead/shell interfaces. Ultrasonic inspection verified the presence of complete lead/shell bonding everywhere except in the intentionally unbonded areas. A small threaded plug was inserted in the model top plate to permit measurement of the position of the top surface of the lead.

Measurements were made during the tests of the inside and outside diameters at locations 90° apart (designated x-x and y-y), the position of the bottom lead surface (4 locations 90° apart), and the position of the top lead surface (by removing threaded plug at one location). Model temperature was observed by means of thermocouple attached to inner and outer surfaces of the shells. All measurements were made at room temperature.

The dimensional changes that resulted from the lead pour and two temperature cycles (to 350°F and 600°F) are given in Table 2.

TABLE 2 DIMENSIONAL CHANGES IN THE $\frac{1}{4}$ SCALE PARTIAL CASK MODEL

	Inside Diameter		Outside Diameter		Top Lead (in)	Bottom Lead (in)
	Y-Y	X-X	Y-Y	X-X		
After lead pour	+.0368	-.0198	-.0026	-.0117	+.024	———
After 350°F	+.0377	-.0262	-.0001	-.0119	+.022	+.0016
After 600°F	+.0373	-.0245	+.0010	-.0145	+.029	+.0025

Note that positive numbers are an increase in dimension. In Y-Y position lead is bonded; unbonded area is in X-X position.

In the tests at elevated temperature the model was oriented vertically with the bottom end down. In this position the lead was free to move into the bottom void under the action of gravity — no such movement occurred. Although the presence of unbonded lead areas tended to distort the diameter measurements, there was a net outward movement of the inner shell after the lead pour averaging 0.017 in., as well as an inward movement of the top lead surface of 0.024 in. These dimensional changes show the presence of a substantial radial tensile stress between the lead and inner shell, which qualitatively confirms the results of the PLACRE analysis of AppendixB. The subsequent thermal cycles to 350°F and 600°F produced no further significant dimensional changes in the model as shown by the data in Table 2. Ultrasonic inspection of the lead bond after the thermal cycles showed no change from the original condition after the lead pour. The PLACRE analysis of Appendix B indicates a radial pressure of about 1000 psi between the lead and the inner shell at a 600°F isothermal condition. Hence, the lead behavior in the model at 600°F should be very similar to the lead behavior

that could be expected in the 10/24 cask at the post-fire condition.

TOP END

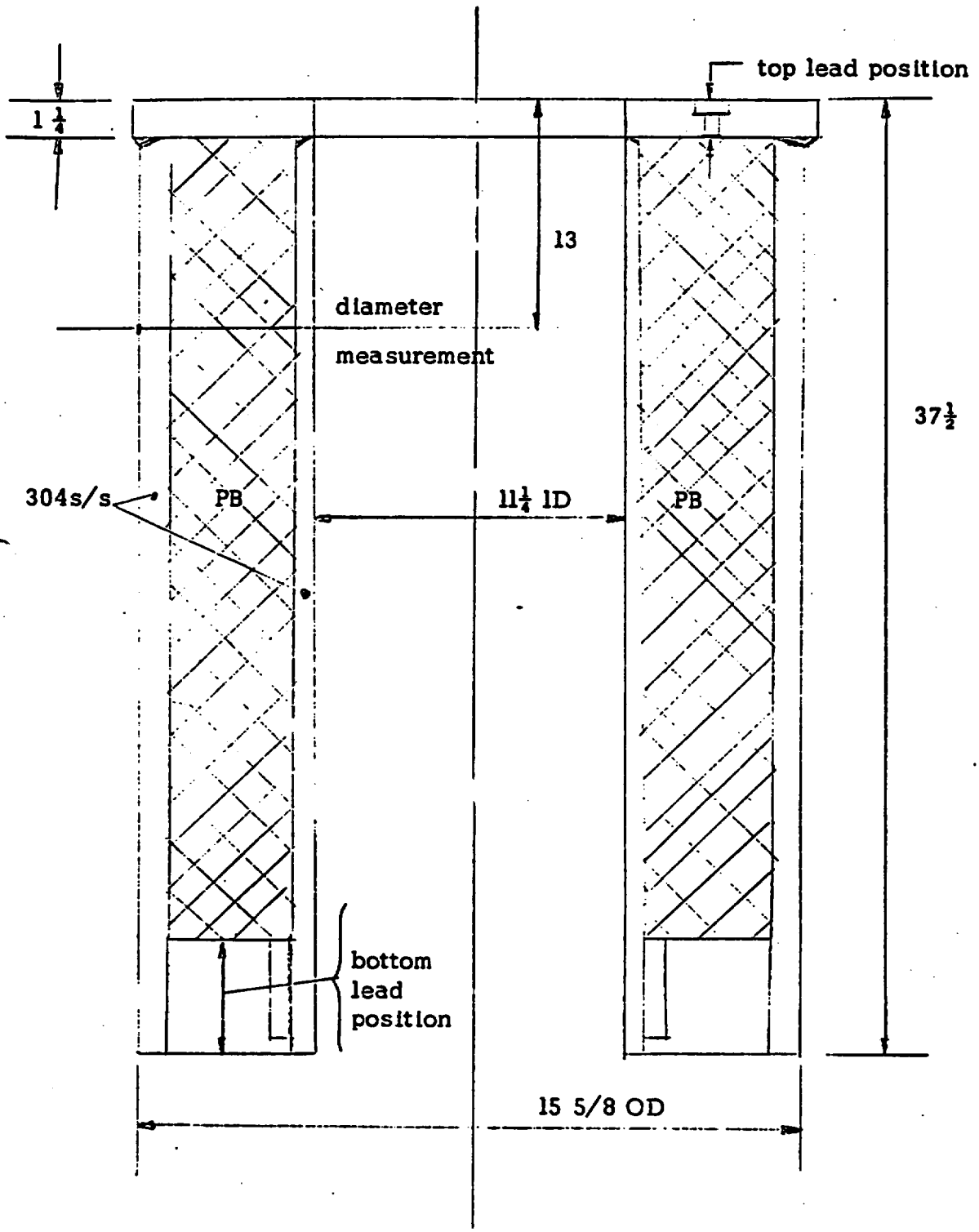

1/4 scale partial model of 10/24 cask

PUNCTURE TEST OF 1/4 SCALE PARTIAL CASK MODEL AT NORMAL TEMPERATURE

The 1/4 scale partial cask model previously used to investigate thermal effects on the composite lead/steel shell (p. XI-D-10) was subjected to a puncture drop test. In accord with previously established modeling procedure the puncture pin diameter was selected as $(\frac{1}{4})$ (6) = 1.5 inches and the required model kinetic energy at impact was required to be (1/64) (8) 10^6 = 125,000 in-lb based on full prototype cask weight of 200,000 lb. (See references). Since the partial model weighed less than a complete quarter scale model of the prototype cask, additional weights were added in the inner cavity and the drop height was increased above 40 inches. The weights were 10 inch diameter steel bars, cushioned where they contacted the inner shell by a $\frac{1}{2}$ inch thick lead sheet and restrained against axial movement by small steel blocks and wedges. The total model weight at test was 2020 lb. and the drop height was 62 inches, giving an impact energy of 125,240 in-lb., slightly more than required. The puncture pin was mild steel with an edge radius of 0.050 in. on the flat machined face, slightly less than the 1/16 in. maximum permissible for a quarter scale model. The model was heated by electric heaters in the cavity until the inner shell reached 400°F and the outer shell was 300°F. The model outer shell cooled somewhat during preparations for the drop; outer shell temperature is estimated to have been about 250°F at impact, giving an average lead temperature of about 325°F.

This puncture test is considered to have been very conservative in that the equivalent impact energy of the full cask was used and the water jacket,

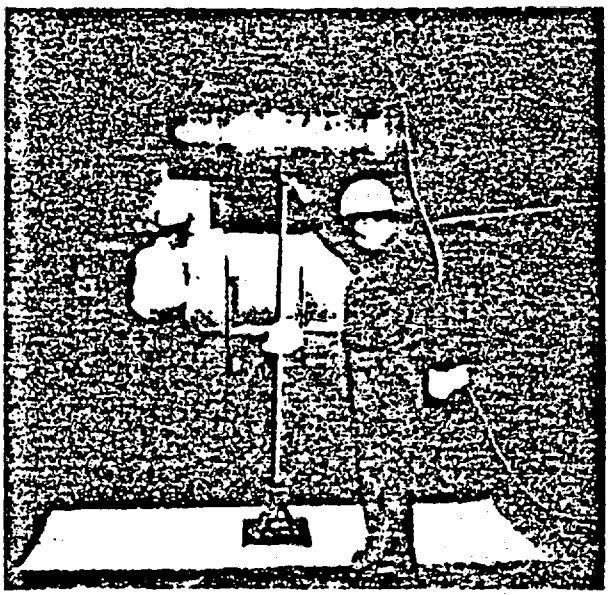

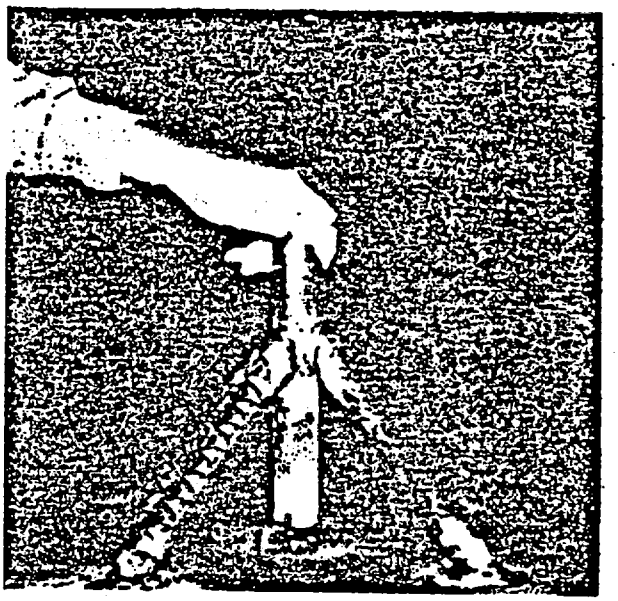

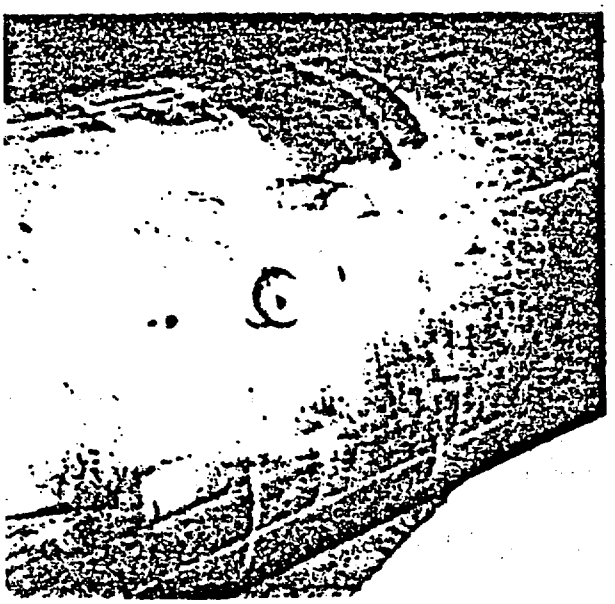

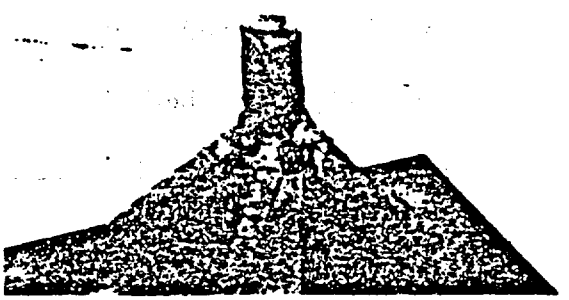

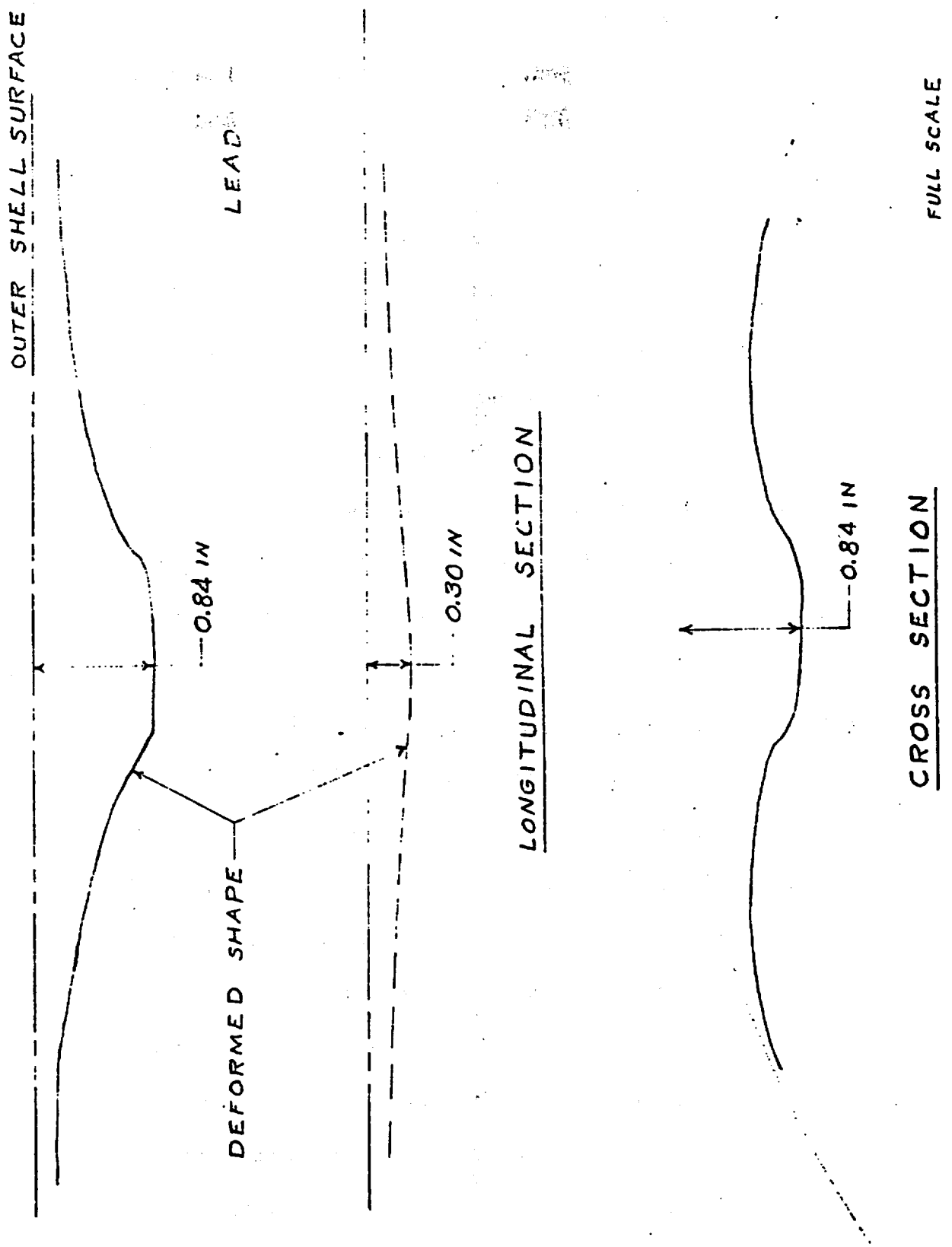

PUNCTURE TEST - 1/4 SCALE MODEL

neutron shield water and three sets of cooling fins were omitted from the model. Thus, the full puncture loading was applied to the outer shell directly without any of the protection normally provided by the water jacket and fins.

The photographs on p. XI-D-15 show the model being aligned and located at proper height above the puncture pin before the drop (upper left), the puncture pin braced to prevent bending (upper right), the indentation in the outer shell after drop on the puncture pin (lower left), and the puncture pin after test (lower right). The puncture pin deformed plastically over an annular region near the edge and mushroomed slightly. The sketch on p. XI-D-16 shows the indentation made in the cask outer shell by the puncture pin. Very little shear was evident at the edges of the indentation, probably because of the plastic deformation that occurred near the edges of the puncture pin. A liquid penetrant test was performed over the indented region and no evidence of cracks was found. As indicated approximately in the sketch (XI-D-16), the inner shell bulged slightly; the indentation extended over a greater distance than was the case in the outer shell. The amount of bulging at the maximum point could be measured accurately, but the general shape of the indentation was only approximated. The indentation on the outer shell was determined accurately by a profile gage.

The puncture test results demonstrate that the outer shell of the 10/24 rail cask will not be punctured under the conditions of the hypothetical puncture accident, even without the additional protection normally provided by the neutron shield tank and fins.

REFERENCES

1) Soper, W. G., "Dynamic Modeling with Similar Materials", pp. 51-56, Colloquium on Use of Models and Scaling in Shock and Vibration, ASME, New York,(1963).

2) Ezra, A. A., "Scaling Laws and Similitude Requirements for Valid Scale Model Work," pp. 57-64, Colloquium on Use of Models and Scaling in Shock and Vibration, ASME, New York (1963).

3) Soper, W. G., "Dynamic Similitude for Lead", pp. 132-133, J. Appl. Mech., Trans. ASME (1961).

4) Evans, J. H., "Structural Analysis of Shipping Casks. Vol. 8 - Experimental Study of the Stress-Strain Properties of Lead Under Specified Impact Conditions", ORNL Dept. No. ORNL- TM-1312 Vol. 8 (1970).

5) Clarke, H. G., "Impact Resistance of Casks", pp. 30-41, Chem. Engng. Progress Symp. Series, No. 56 Vol. 61, AI Ch. E (1965)

6) Spaller, A. E., "Structural Analysis of Shipping Casks. Vol. 2 - Resistance to Puncture", ORNL Dept. No. ORNL-TM-1312 Vol. 2 (1966).

7) Nelms, H. A., "Structural Analysis of Shipping Casks. Vol. 3 - Effects of Jacket Physical Properties and Curvature on Puncture Resistance", ORNL Dept. No. ORNL-TM-1312 Vol. 3 (1968).

SECOND PUNCTURE TEST OF 1/4 SCALE PARTIAL CASK MODEL

In the first puncture test of the 1/4 scale partial cask model the outer shell temperature at impact was lower than the temperature expected under normal transport conditions (p. XI-D-14). Hence, a second puncture test was performed to evaluate the effect of a higher temperature on puncture resistance of the outer shell. In this test the impact energy was the same as in the initial test (2020 lb. model weight and 62 in. drop height); the model was rotated 180° so the puncture pin struck on the opposite side from the original test. The model was heated as before by electric heating elements in the cavity; these were removed when the inner shell reached 375°F and the outer shell reached 330°F. During preparations for the drop the model temperature was maintained through use of gas burners applied to the outer shell. The outer shell temperature at time of drop was 325°F; average lead temperature is estimated to have been about 340°F.

The photographs on page XI-D-20 show the indentation in the outer shell and the puncture pin after test. As in the first test the puncture pin deformed plastically near the edge and mushroomed slightly. The sketches on page XI-D-21 show the indentation in the outer shell and the bulging of the inner shell resulting from the impact on the puncture pin. The deformation is somewhat greater than in the first test. A liquid penetrant test applied over the indented region of the outer shell showed no evidence of cracks. Hence, the outer shell was not penetrated in this second puncture test at a 325°F shell temperature.

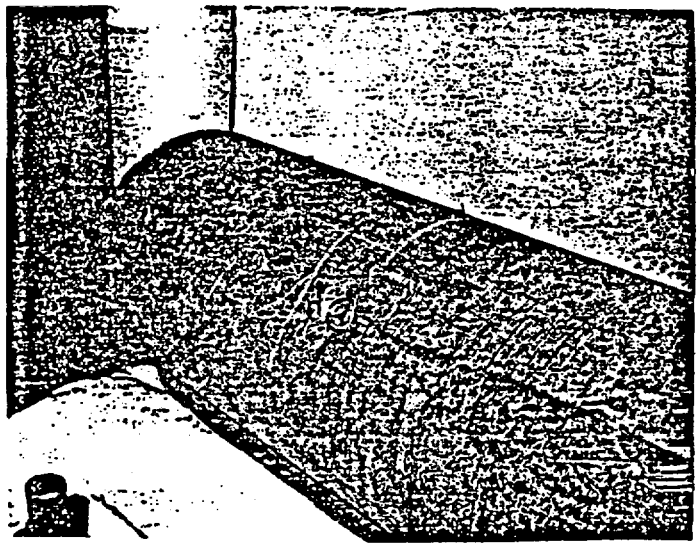

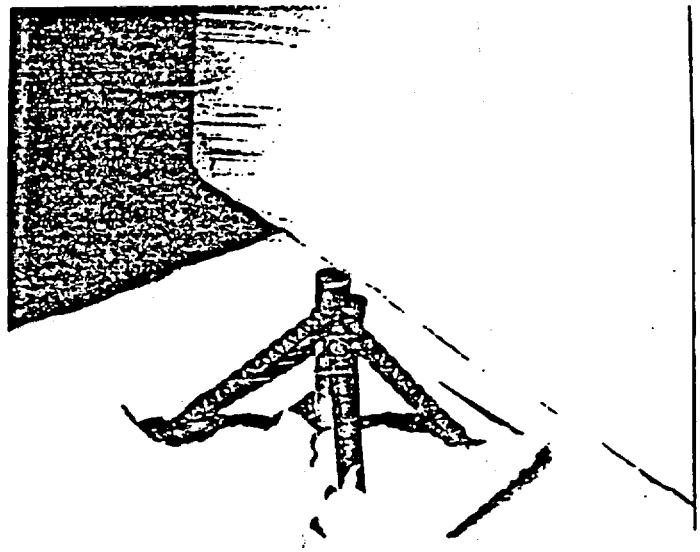

Second Puncture Test - 1/4 Scale Model

SECOND PUNCTURE TEST - 1/4 SCALE MODEL

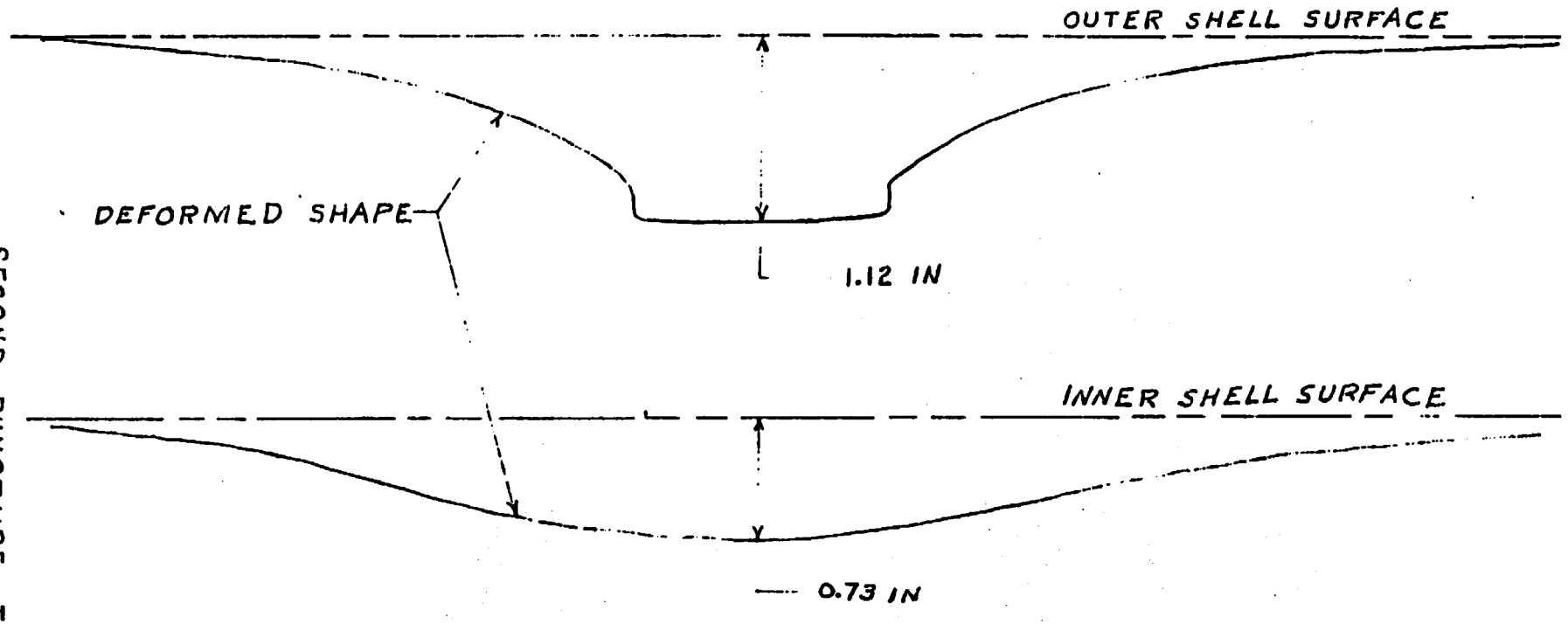

LONGITUDINAL SECTION

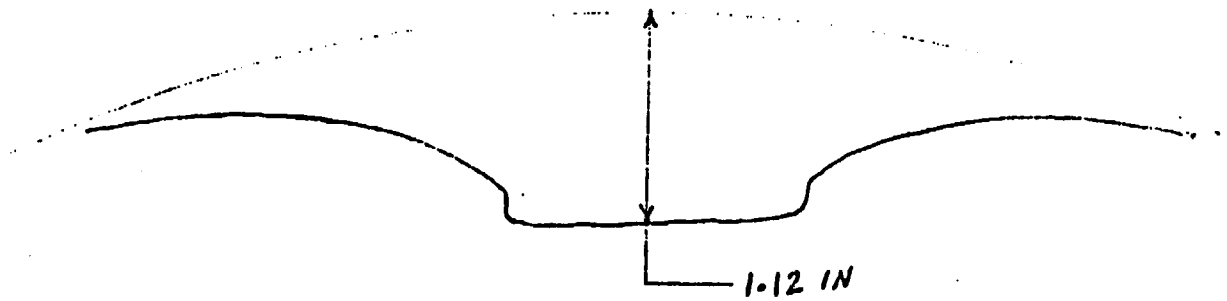

CROSS SECTION

FULL SCALE

5/76